

Automated Image-Quantification for Investigating the Mechanics of Cytoskeletal Spindles

A thesis

Submitted in partial fulfilment of the requirements

Of the degree of

Doctor of Philosophy

By

Anushree Ravindra Chaphalkar

Registration ID: 20123178




INDIAN INSTITUTE OF SCIENCE EDUCATION AND RESEARCH, PUNE

(2019)

Declaration

I declare that this written submission represents my ideas in my own words and wherever others' ideas have been included, I have adequately cited and referenced the original sources. I also declare that I have adhered to all principles of academic honesty and integrity and have not misrepresented or fabricated or falsified any idea/data/fact/source in my submission. I understand that violation of the above will be cause for disciplinary action by the institute and can also evoke penal action from the sources which have thus not been properly cited or from whom proper permission has not been taken when needed.



Anushree Ravindra Chaphalkar

Registration ID: 20123178

Date: 30/01/2019

Certificate

Certified that the work incorporated in the thesis entitled 'Automated Image-Quantification for Investigating the Mechanics of Cytoskeletal Spindles', submitted by Ms. Anushree Ravindra Chaphalkar was carried out by the candidate, under my supervision.

The work presented here or any part of it has not been included in any other thesis submitted previously for the award of any degree or diploma from any other University or institution.



Dr. Chaitanya Athale

Date: 30/01/2019

डा. चैतन्य आठले / Dr. Chaitanya Athale
असोसिएट प्रोफेसर / Associate Professor
भारतीय विज्ञान शिक्षा एवं अनुसंधान संस्थान
Indian Institute of Science Education & Research
पुणे / Pune - 411 008, India

Publications

Published

Anushree R. Chaphalkar, Kunalika Jain, Manasi S. Gangan, and Chaitanya A. Athale. (2016) 'Automated Multi-Peak Tracking Kymography (AMTraK): A tool to quantify subcellular dynamics with sub-pixel accuracy', *PLOS One*, vol. 11, no. 12, p. e0167620.

In Preparation

Anushree R. Chaphalkar and Chaitanya A. Athale. 'Single particle motility in label free images quantified using DIC-Object Tracker (DICOT)'.

Thibault Brugiere*, Anushree R. Chaphalkar*, Chaitanya A. Athale, Marie Delattre. 'Evolutionary Diversification of Spindle Forces During Asymmetric Division in Nematodes'.

Anushree R. Chaphalkar, Gayathri Pananghat and Chaitanya A. Athale, 'Bacterial ParM filament sliding: Implications for plasmid segregation'.

Acknowledgements

Support, guidance and love from the people I am about to mention, has enabled the completion of my PhD thesis.

I wish to express sincere gratitude for my PhD advisor, Dr. Chaitanya Athale for giving me the opportunity to work in the field of computational biology. Thank you for introducing me to coding, for helping me find my way through it and in the process, making me discover the joy in it. Thank you for the valuable scientific discussions and advice as well as constant guidance and support in my work.

I am grateful to the members of my Research Advisory Committee, Dr. Anu Raghunathan and Dr. Gayathri Pananghat for their suggestions and advice. I would like to thank Dr. Gayathri Pananghat and Dr. Marie Delattre for data and fruitful discussions on ParM dynamics and nematode spindles respectively, during the collaborative work. I thank Prof. Francois Nedelec for the valuable discussion and help with Cytosim. I sincerely thank Prof. LS Shashidhara for his support and guidance during my PhD tenure. I would also like to thank Dr. VS Rao and Dr. Urmila Kulkarni Kale. I thank IISER for the facility and the IISER community for smoothening out my PhD journey.

Special thanks to my friends at IISER, especially Neha Khetan, Kunalika Jain and Parichit Sharma. Thank you for being there. My thanks to members of Athale lab. I cherish our moments of brainstorming in the lab and the fun times we've spent outside. I thank my help, Mrs. Ratna Shinde, whose kind efforts I shall always be grateful for. Thanks are due, to my funding agencies - UGC-CSIR for the research fellowship and DST-SERB for the international travel grant.

To my family, I owe everything I am and I have. My passion for science stems from home. I thank my parents, Mr. Ravindra Chaphalkar and Prof. Sushama Chaphalkar, for guiding me and being ever encouraging in all my endeavours. Heartfelt thanks to my grandparents, parents and my sister Ashwini Chaphalkar for the immense and unconditional love they have always given me, despite all odds.

Abstract

Propagation of a cell requires successful segregation of its genetic material into resulting daughter cells, a process brought about by the coordinated dynamics of cytoskeletal spindles. High resolution time-lapse microscopy has opened new avenues for understanding the dynamics of spindles within single cells. Automated computational image analysis allows the extraction of useful quantitative information from microscopy data in an unbiased, objective and reproducible manner. In the present work, I have developed three automated image analysis tools in MATLAB to investigate the quantitative aspects of subcellular dynamics such as particle motion, intensity and interaction. The tools are called Automated Multi-peak Tracking Kymography (AMTraK), Fluorescence Tracker (FluoreT) and Differential Interference Contrast Object Tracker (DICOT). While AMTraK and FluoreT are used to analyse time-lapse fluorescence images, DICOT applies to images from time-lapse DIC microscopy. The tools are validated with simulated noisy data, tested on experimental image-series and benchmarked by comparing their results with manual measurements, published literature and outputs of other software. The wide utility of these tools is demonstrated on diverse data ranging from *in vitro* microtubule gliding assays and clathrin assembly kinetics to *in vivo* axonal vesicle transport, DNA segregation in *E. coli* and cytoplasmic granule mobility in *C. elegans* embryos.

ParM filaments that form a plasmid-segregating spindle in *E. coli* cells display dynamic instability and are also known to slide *in vitro*. Our Brownian dynamics simulations of the ‘search and capture’- based assembly of the ParMRC spindle suggest that dynamic instability does not alter the time taken by ParM filaments for plasmid capture. Quantitation of ParM sliding using AMTraK shows that the filaments slide against each other in a contractile, sub-diffusive manner at a speed higher than the rate of polymerization.

The mobility of the mitotic spindle during the process of asymmetric positioning is shown to vary between nematode species, suggesting an evolutionary difference in spindle mechanics. Viscosity of the cytoplasm is hypothesized to give rise to these differences. Our novel, non-invasive quantification of cytoplasmic viscosity using DICOT suggests that viscosity may contribute to the observed difference in spindle motion patterns during positioning in the embryos of six related nematode species including *C. elegans*.

My work highlights the insights that computational tool development can provide when applied to *in vitro* and *in vivo* dynamics of subcellular processes.

Abbreviations

AMPPNP	Adenylyl-imidodiphosphate
AMTraK	Automated Multi-peak Tracking Kymography
ATP	Adenosine Triphosphate
DIC	Differential Interference Contrast
DICOT	Differential Interference Contrast Object Tracker
FluoreT	Fluorescence Tracker
GFP	Green Fluorescent Protein
GTP	Guanosine Triphosphate
GUI	Graphical User Interface
HupA	Heat unstable protein A
LOI	Line of Interest
MT	Microtubule
MTOC	Microtubule Organizing Centre
SNR	Signal to Noise Ratio
TIRF	Total Internal Reflection Fluorescence

Contents

1. Introduction	11
1.1. DNA segregation machinery in eukaryotes and prokaryotes	11
Eukaryotic spindles	11
Prokaryotic spindles	14
1.2. Visualizing subcellular dynamics by microscopy	17
Fluorescence microscopy	17
Label-free microscopy	20
1.3. Computational analysis of microscopy images	21
Accuracy, precision and error	22
1.4. Simulation of cytoskeletal and spindle dynamics	23
1.5. Organization of the thesis	23
1.5.1. Computational tool development for automated image analysis	23
1.5.2. Applications: Spindle mechanics	24
2. Materials and Methods	25
2.1. Implementation of algorithms	25
2.2. Pre-Processing of image data from microscopy	25
2.3. Simulating fluorescence bead images	25
2.4. Calculation of signal to noise ratio	26
2.5. Otsu's thresholding	26
2.6. Centroid detection	27
2.7. Nearest-neighbour tracking	27
2.8. Data analysis	27
2.9. Estimation of effective diffusion coefficient	27
2.10. Stokes-Einstein's equation for estimation of viscosity	29
3. Automated Multi-Peak Tracking Kymography (AMTraK)	30
3.1. Introduction	30
3.2. Materials and methods	32
3.2.1. Simulated test images of bead diffusion in 1D	32
3.2.2. Microscopy of segregating nucleoids and kinesin-MT gliding assay	33

3.2.3. Image pre-processing	33
3.2.4. Manual analysis of kymographs	33
3.2.5. AMTraK implementation specifics	34
3.2.6. Data analysis	34
3.3. Algorithm and workflow	34
3.4. Results	40
3.4.1. Accuracy of detection	40
3.4.2. Detecting splitting events in bacterial DNA-segregation	42
3.4.3. Microtubule transport: filament edges, centers and time-dependence of velocity	44
3.4.4. Fusion of MT asters	46
3.4.5. Kinetics of clathrin assembly during in vitro vesicle formation	47
3.4.6. Axonal vesicle transport: Characterizing directional switching	49
3.5. Discussion	51
3.6. Conclusion	56
4. Fluorescence Tracker (FluoreT)	57
4.1. Introduction	57
4.2. Materials and methods	58
4.2.1. Simulated test images	58
4.2.2. Microscopy and image pre-processing	58
4.2.3. FluoreT implementation specifics	59
4.3. Algorithm and workflow	60
4.4. Results	63
4.4.1. Accuracy of position detection	63
4.4.2. Accuracy of length detection	64
4.4.3. Tracking diffusive and directional motion of simulated beads	66
4.4.4. Motility and length of motor-driven microtubules	67
4.5. Discussion	69
4.6. Conclusion	70
5. Differential Interference Contrast Object Tracker (DICOT)	72
5.1. Introduction	72

5.2. Materials and methods	73
5.2.1. Microscopy of diffusive beads	73
5.2.2. Image pre-processing and segmentation	74
5.2.3. DICOT implementation specifics	74
5.2.4. Data analysis	74
5.3. Algorithm and workflow	75
5.4. Results	79
5.4.1. Diffusive motion of beads	79
5.4.2. Estimation of viscosity of water and glycerol solution	82
5.5. Discussion	83
5.6. Conclusion	86
6. Cytoplasmic Viscosity Varies and Correlates with Spindle Motion Among Zygotes of Related Nematode Species	87
6.1. Introduction	87
6.2. Materials and methods	89
6.2.1. Nematode strains, culture and live-cell imaging	89
6.2.2. Image pre-processing and analysis	89
6.2.3. Density correction of viscosity	89
6.3. Results	90
6.3.1. Size and motion of yolk granules in nematode zygotes	90
6.3.2. Estimation of solvent phase viscosity of the cytoplasm	95
6.3.3. Viscosity corrected for density of granules	97
6.4. Discussion	100
6.5. Conclusion	101
7. Dynamic Instability and Sliding of ParM Filaments: Implications for Plasmid Segregation	102
7.1. Introduction	102
Dynamic instability of ParM filaments	103
Sliding and bundling of ParM filaments <i>in vitro</i>	104
7.2. Materials and methods	106

	10
7.2.1. Computer simulations	106
Cell system	106
Plasmids	107
Filaments	107
7.2.2. Microscopy, image pre-processing and analysis	110
Angle of contact measurement	110
Quantitative kymography for sliding and diffusion analysis	110
Persistence length measurement	111
Data analysis	111
7.3. Results	112
7.3.1. Simulations of ParM spindle assembly	112
Plasmids do not translocate to the poles by diffusion alone	112
Dynamic instability of ParM does not affect plasmid capture time in	
<i>E. coli</i> cells	113
Filaments bound to plasmids show slightly increased lifetimes	115
7.3.2. Quantitative image analysis of ParM filament sliding	117
Sliding is favoured by acute angles of contact	117
Sub-diffusive sliding of short filaments	119
Kymography reveals three phases of filament sliding	120
Bundles show greater persistence length as compared to single filaments	122
7.4. Discussion	124
7.5. Conclusion	126
8. Conclusion and Outlook	128
9. Bibliography	132

Chapter 1

Introduction

In this thesis, I have aimed to improve our quantitative understanding of subcellular dynamics by a combination of computational tool development, analysis of microscopy image data and computer simulations. In this chapter, I briefly describe cytoskeletal spindles that segregate DNA and the microscopy methods employed for observing subcellular dynamics. Further, I aim to motivate the computational analysis of microscopy image data and computer simulations of cytoskeletal systems.

1.1. DNA segregation machinery in eukaryotes and prokaryotes

The propagation of a cell requires successful segregation of its genetic material into resulting daughter cells. In both, prokaryotes and eukaryotes, this process is brought about by large subcellular structures called ‘spindles’ that are composed of cytoskeletal polymers and associated regulatory proteins. Spindles are transient in nature. They are formed at the onset of division; they orchestrate the segregation of DNA to opposite poles of the cell and disintegrate shortly after segregation. DNA segregation in all the three kinds of cell division - binary fission, meiosis and mitosis - is known to involve the spindle apparatus. Given this fact, the study of organization and working of spindles is of fundamental importance not only to understand how cells divide, but also to accelerate the development of drugs that target dividing cells, such as chemotherapy drugs and antibacterial substances.

In this thesis, we investigate biophysical aspects relevant to mitotic spindles in eukaryotes and prokaryotes. Although the goal of this machinery in both kinds of cells is to segregate copies of replicated DNA prior to cell division, the structure, components and mechanism of action of spindles appear to vary widely.

Eukaryotic spindles

In eukaryotic cells, spindles are composed of microtubules (MTs), ~25 nm wide dynamic filaments formed by GTP-hydrolysis dependent polymerization of tubulin subunits (Figure 1.1, Figure 1.5A). Each subunit is a heterodimer made of α and β tubulin monomers held by tight, non-covalent bonds. The structural and kinetic polarity of microtubules is

attributed to the α - β dimeric subunits such that the end with β is the fast-growing end or the plus end, while the α -end is the slow-growing or minus end. Microtubules are nucleated by centrosomes or microtubule organizing centres (MTOCs) composed of γ tubulin ring complexes such that the MT- minus ends are embedded in MTOCs while the plus ends continue to shrink and grow, extending outward in cellular space. The MTOCs with emanating microtubules form the two poles of a bipolar, antiparallel spindle that segregates chromosomes during mitosis.

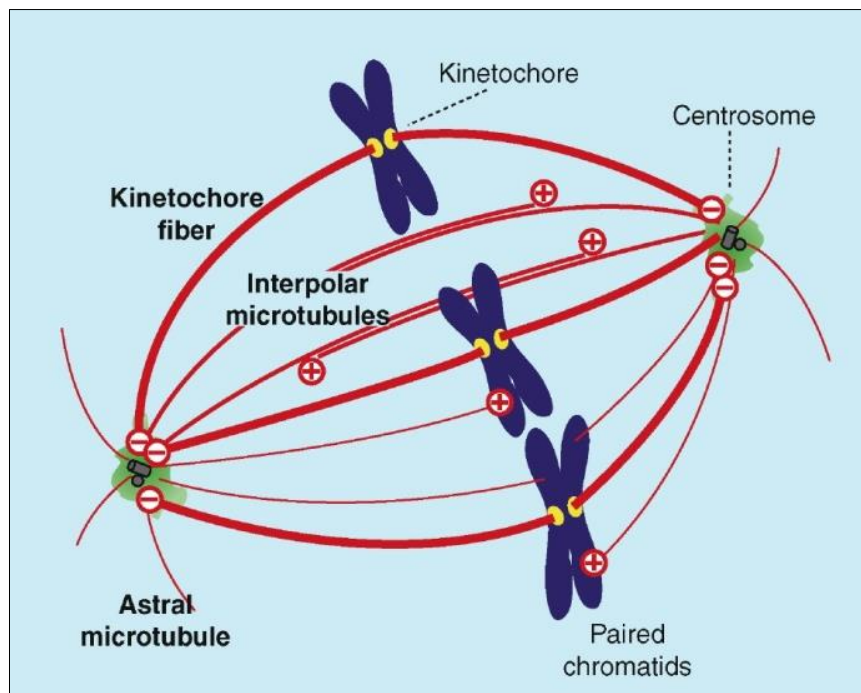


Figure 1.1. Mitotic spindle in eukaryotes. The spindles in eukaryotes are composed majorly of microtubule filaments (red) that extend outward from MTOCs (centrosomes, green) to the kinetochores (yellow) of chromosomes (blue) or to the other MTOC or towards the cell cortex. (Reproduced from Gadde and Heald, 2004).

Microtubules display dynamic instability, i.e. they alternate between phases of growth and rapid shrinkage (Mitchison and Kirschner, 1984). The transition of an MT from growth to shrinkage is called ‘catastrophe’, while the transition from shrinkage to growth is called ‘rescue’. According to the ‘search and capture’ model of eukaryotic spindle assembly (Kirschner and Mitchison, 1986), the MT plus ends search cellular space and capture chromosomes at their kinetochores. Theoretical studies show that polymers displaying dynamic instability are highly efficient in ‘search and capture’ in contrast with a polymer lacking the property (Holy and Leibler, 1994). Dynamic instability is shown to reduce the

time taken for target capture by orders of magnitude (Figure 1.2A). Further, mathematical modelling and Brownian dynamics based simulations suggest that dynamic instability alone is insufficient to bring about chromosome capture at mitotic timescales unless combined with a bias such as a RanGTP gradient that stabilizes MTs growing towards chromosomes (Wollman et al., 2005; Athale et al., 2008) (Figure 1.2B).

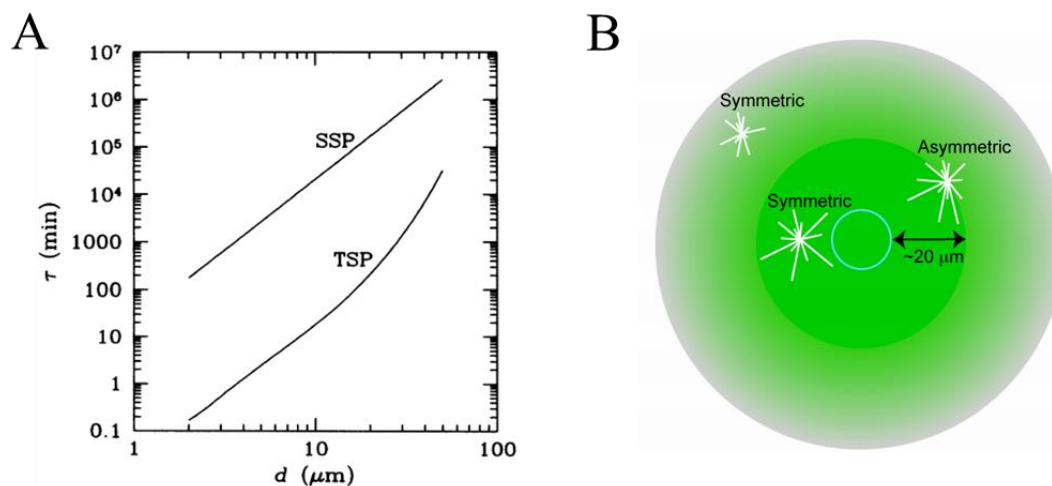


Figure 1.2. ‘Search and capture’ of DNA. (A) Target capture time (τ) is plotted versus distance from the target. A polymer with dynamic instability (two-state polymer (TSP)) shows 10^3 times lower capture time as compared to a polymer lacking dynamic instability (single-state polymer (SSP)). (Reproduced from Holy and Leibler, 1994). (B) Schematic suggests a ‘biased-search-and-capture’ model and shows how a MT stabilizing gradient (green) affects the length asymmetry of MT-asters (white). (Reproduced from Athale et al., 2008).

Several MT-associated proteins regulate MT dynamics and maintain the stability and structural integrity of the eukaryotic spindle during segregation (reviewed by Gadde and Heald, 2004). Molecular motors such as dynein and kinesin hydrolyse ATP to ‘walk’ along MT tracks and perform varied functions related to the spindle, including sorting, crosslinking and sliding of MTs (Howard, 2001). Cytoplasmic dynein, a minus-end directed motor is known to focus the minus ends of MTs thereby enabling spindle pole formation. Additionally, dynein motors anchored at the cell cortex are known to pull on astral microtubules to bring about spindle positioning in cells such as budding yeast and *C. elegans* embryos (reviewed by Grill and Hyman, 2005). In previous work, the mobility of the mitotic spindle during the process of asymmetric positioning was shown to vary between nematode species, suggesting an evolutionary difference between spindle mechanics (Valfort et al., 2018; Farhadifar et al., 2015; Riche et al., 2013). A simple hypothesis is that the viscosity of

the cytoplasm could give rise to these differences. Indeed, predictions from simulations of spindle-oscillatory mechanics in *C. elegans* have suggested that order of magnitude differences in the cytoplasmic viscosity can change the qualitative nature of spindle oscillations by mechanical damping (Kozłowski et al., 2007). This motivates the study of biophysical properties of the cytoplasm and their effect on spindle motion patterns in single-celled nematode embryos. In Chapter 6 of the thesis, we use a novel, non-invasive microrheology approach combined with automated image analysis to quantify the cytoplasmic viscosity of multiple nematode zygotes.

Prokaryotic spindles

Contrary to earlier belief, bacteria possess an extensive cytoskeleton (Vollmer, 2006; Wickstead and Gull, 2011; Cabeen and Jacobs-wagner, 2010; Michie et al., 2006) whose constituents are vital for various molecular events including DNA segregation. In addition to genomic DNA, bacteria are known to naturally possess extrachromosomal, self-replicating molecules of DNA called ‘plasmids’. Plasmids are reported to participate in the metabolism and virulence of the cell by conferring properties such as resistance to heavy metals, toxic chemicals and antibiotics to the cell. While high copy number plasmids are shown to be partitioned randomly between daughter cells prior to cell division (Reyes-Lamothe et al., 2014; Ghosh et al., 2006; Ebersbach and Gerdes, 2005), several low-copy-number plasmids ensure their faithful partition by encoding an active spindle machinery composed of homologs of eukaryotic cytoskeletal elements (Nordstrom and Austin, 1989; Becker et al., 2006; Aylett et al., 2010; Moller-Jensen et al., 2002; Fink and Löwe, 2015). A variety of prokaryotic spindle machineries made of cytomotive filaments have been reported so far (Gerdes et al., 2010; Schumacher, 2012; Ebersbach and Gerdes, 2005)(Figure 1.3). In this thesis, we focus on a well-studied type-II plasmid segregation system encoded by plasmid R1 in *E. coli*. R1 is a ~100 kb low copy number plasmid (4-6 copies per cell) that encodes the ParMRC spindle at its *par* locus.

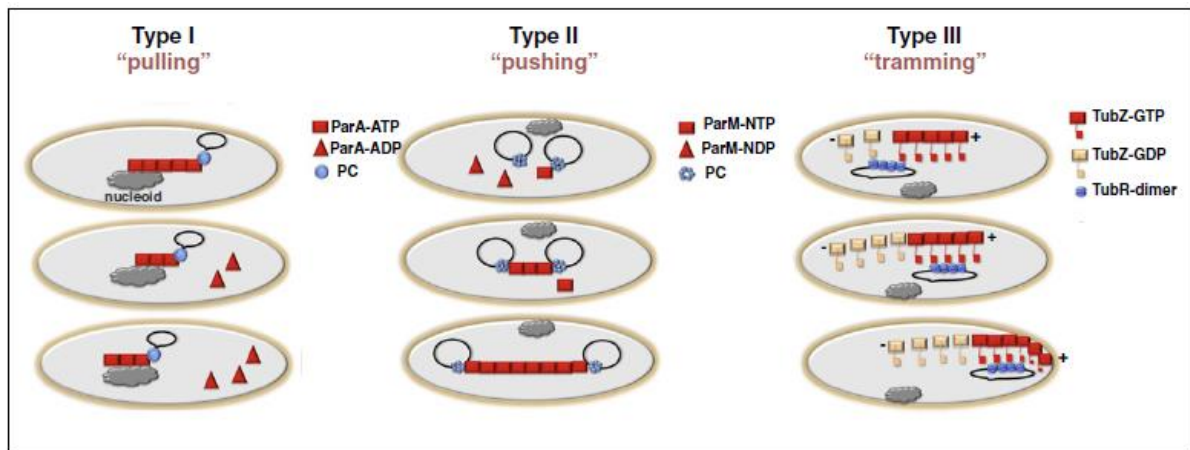


Figure 1.3. Schematic of types of plasmid segregation systems. The Type I system (for example, ParABS, SopABC) utilizes the bacterial nucleoid as a track. ParB bound plasmids are pulled by disassembling ParA filaments, enabling the uniform distribution of plasmids on nucleoid surface. In the type II system (for example, ParMRC, AlfA), plasmids are pushed apart by insertional polymerization of filaments bound to them. The type III system (for example, TubZRC) involves segregation by polymers that undergo treadmilling. (Reproduced from Schumacher, 2012).

As compared to eukaryotic spindles that span a length of tens of microns, the spindles in prokaryotes are minimal not only in size, but also in the number of components. The ParMRC system, for example, consists only of three components. ParM, the cytomotive element of the spindle, is an actin homolog that generates force by ATP-dependent polymerization. Other two components include *parC*, a *cis*-acting centromere-like DNA sequence and ParR, an adaptor protein that binds to both, *parC* and ParM. When a ParM plus end binds to ParRC, they form a complex that we will henceforth refer to as a 'half-spindle'. Two such 'half-spindles' assemble into a bipolar, transient mitotic spindle of average length $\sim 1.5 \mu\text{m}$ *in vivo* that pushes plasmids apart (Moller-Jensen et al., 2002; Campbell and Mullins, 2007; Gayathri et al., 2012) (Figure 1.4, Figure 1.5B).

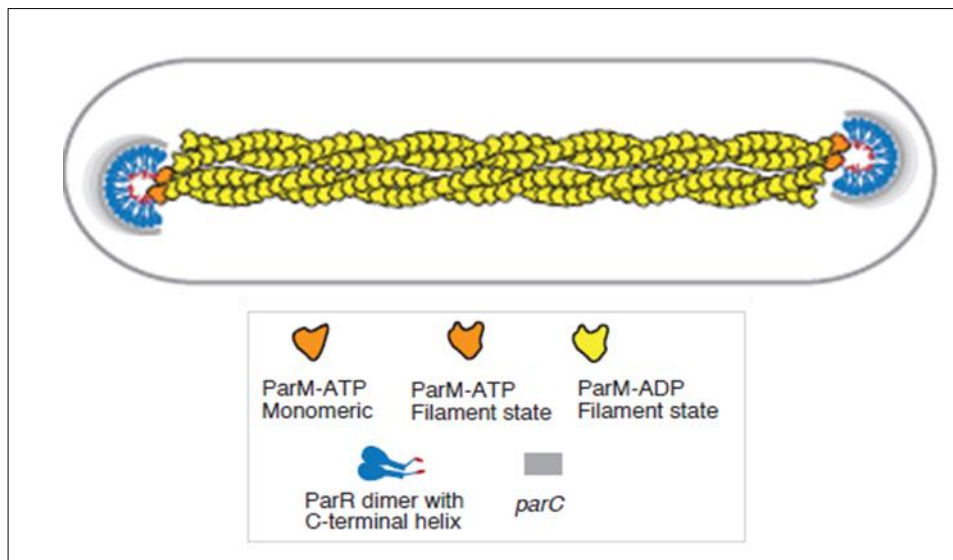


Figure 1.4. ParMRC spindle in *E. coli*. The plus ends of ParM polymers bind to plasmids at ParRC complexes to form a half-spindle. Two such half spindles associate to form an antiparallel, bipolar spindle. Insertional polymerization at the bound ends of ParM filaments generates force to push plasmids to opposite poles of the cell. (Reproduced from Gayathri et al., 2012).

Interestingly, ParM has been shown to display dynamic instability as that of microtubules (Garner et al., 2004). However, while ParM filaments are observed to undergo catastrophic events, no rescues have been observed in them. *In vitro* reconstitution experiments have been performed previously to show that the dynamic instability of ParM enables easy turnover of filaments and provides excess monomer to drive the elongation of the spindle (Garner et al., 2007). As seen in eukaryotes, dynamic instability is hypothesized to facilitate ParM filaments to search cellular space and capture their plasmid targets. However, the effect of ParM dynamic instability on the efficiency of plasmid capture has not been thoroughly investigated. Given that the ParMRC spindle requires the interaction of only three well-studied components to assemble and function, the use of computer simulations is most suited to address this question. With this aim, in Chapter 7 of the thesis, we simulate the ‘search and capture’ of plasmid targets by ParM filaments in an *E. coli* cell.

Once the entire spindle is assembled, insertional polymerization of ParM filaments at their plasmid bound ends pushes sister plasmids to opposite poles of an *E. coli* cell. In addition, ParM filaments are known to slide and form bundles *in vitro* in the absence of additional proteins, a feature only qualitatively reported recently in literature (Gayathri et al., 2012). How dynamic instability, insertional polymerization and inter-filament interactions together bring about the process of plasmid segregation in an *E. coli* cell in a span of a few minutes still remains poorly understood. In eukaryotic cells, motor-assisted sliding of MTs is

speculated to play a role in maintaining spindle length (Burbank et al., 2007; Goshima and Scholey, 2010). However, determining the potential role of ParM sliding in spindle assembly and plasmid segregation is difficult. This is because in an *E. coli* cell, the direct observation of sliding interactions in ParM filaments is hampered greatly due to the diffraction limit of light microscopy (~250 nm). Therefore, computer simulations are found most useful to identify the potential role of ParM filament sliding. Simulations of this process are currently hindered by the lack of quantitative information on ParM filament sliding. As a first step, in the latter half of Chapter 7, we quantify for the first time to our knowledge, the *in vitro* sliding parameters of ParM filaments by automated kymography.

Motivated by the need to unravel the complexity of organization and function of mitotic spindles, multiple studies have examined the time-dependent interactions between the spindle components using live-cell microscopy. Owing to the transient and dynamic nature of spindles, time-lapse light microscopy is found highly effective for studying these structures (Figure 1.5).

1.2. Visualizing subcellular dynamics by microscopy

Microscopes have aided the human eye for centuries, enabling the visualization of micrometer and nanometer-sized objects such as molecules, clusters, cytoskeletal filaments, organelles or cells themselves. Light microscopes make use of light in the visible range (wavelength 400-700 nm) and a combination of lenses to magnify objects. Since their invention in the 17th century, light microscopes have evolved greatly in terms of resolution and user-friendliness, thereby making light microscopy an indispensable tool in cell biology. The advent of time-lapse microscopy and live-cell imaging has further opened new avenues for the analysis of spatiotemporal dynamics of subcellular events that lay the foundation for higher order cellular processes such as determination of cell shape, locomotion, cell division, cell-cell adhesion and differentiation.

Light microscopy can be broadly classified into two categories- (a) labelled or fluorescence microscopy and (b) label-free microscopy. In the following text I dwell briefly on the two kinds of imaging.

Fluorescence microscopy

Fluorescence microscopy makes use of fluorophores or dyes that absorb light of a particular wavelength, reach their excited state and subsequently emit light of a longer

wavelength. These fluorophores are used to ‘label’ the molecules of our interest either by expressing them within cells or by physically introducing them into the system. Over the last two decades, the emergence of a plethora of compatible fluorophores, high resolution microscopy and robust computer programs for quantitative analysis of data has popularized the use of fluorescence microscopy for *in vitro* as well as *in vivo* imaging.

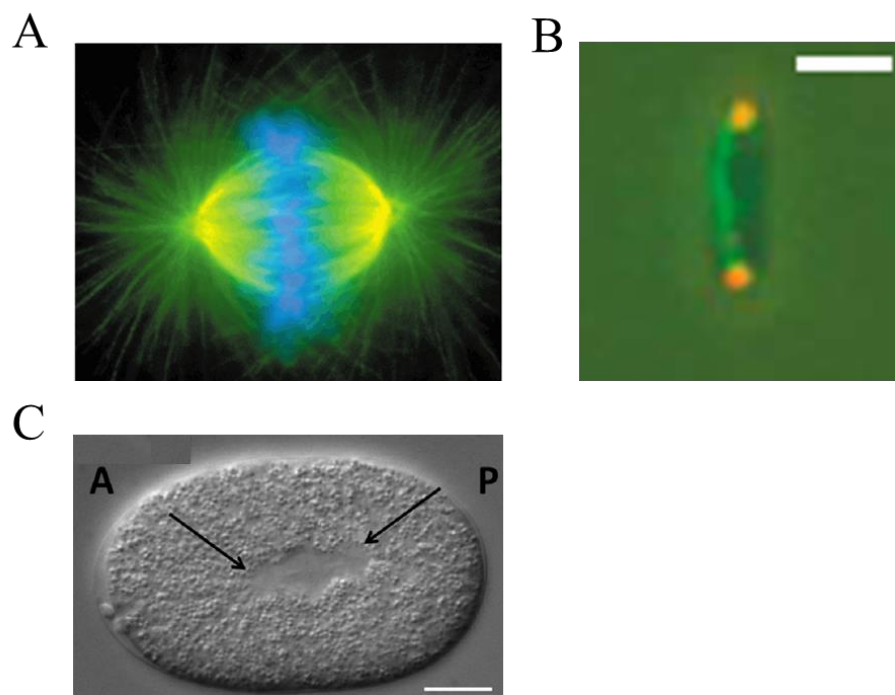


Figure 1.5. DNA-segregating spindles imaged by different forms of light microscopy. (A) Immunofluorescence micrograph of a eukaryotic mitotic spindle imaged during metaphase in a tissue culture cell. MTs (green) associated with chromosomes (blue) aligned at the metaphase plate are seen. The yellow region represents the overlapping of MTs with TPX2 (red), a spindle component. Reproduced from (Wittmann et al., 2001). (B) A phase-contrast image of an *E. coli* cell is overlaid with a fluorescence microscopy image of *par*⁺ plasmids (orange) pushed to cell poles by a ParM spindle (green). Scale bar – 2 μ m. (Reproduced from Moller-Jensen et al., 2003). (C) DIC image of a mitotic spindle within a single-celled *C. elegans* embryo. Centrosomes are marked by black arrows. A marks the anterior and P marks the posterior regions of the embryo. Scale bar – 10 μ m. (Adapted from Cluet et al., 2014).

Although fluorescence microscopy has several advantages, there are some inherent challenges associated with this method. Probing the components of a bacterial cell (size \sim 2 μ m) through optical microscopy is hindered by the diffraction limit of light. Phototoxicity due to prolonged exposure to high intensity radiation may damage cells, alter their behaviour and affect their viability (Sarah Grah et al., 2017; Dixit and Cyr, 2003). Rapid photobleaching

of fluorophores can result in poor quality of images over long durations of microscopy. Also, the signal obtained from thicker samples is obscured by out-of-focus light coming from planes above and below the focal plane. I shall allude now to the recent technological variants of fluorescence microscopy that have helped overcome some of these challenges and are found especially suitable for imaging spindles and their cytoskeletal elements (Figure 1.6A,B).

Confocal microscopes provide greater axial and lateral resolution as compared to typical epifluorescence microscopes as they illuminate the samples with focussed laser beams of light and further eliminate out-of-focus light by incorporating a pinhole aperture at the detector (Pawley, 1995). Total Internal Reflection Fluorescence (TIRF) microscopy (reviewed by Toomre and Manstein, 2001) is commonly used for analysing the *in vitro* dynamics of cytoskeletal filaments since it provides high axial resolution and selectively illuminates ~100 nm below the coverslip, thereby improving the signal to noise ratio.

Speckle labelling is yet another technique that uses low levels of fluorescent dyes and is most suitable for visualizing the polymerization and depolymerisation kinetics of cytoskeletal polymers (Waterman-Storer et al., 1998). The introduction of a low concentration of labelled monomers results in formation of polymer lattices that contain a mixture of labelled and unlabelled subunits. This in turn gives rise to fiduciary marks that allow better visualization of polymer turnover and movement.

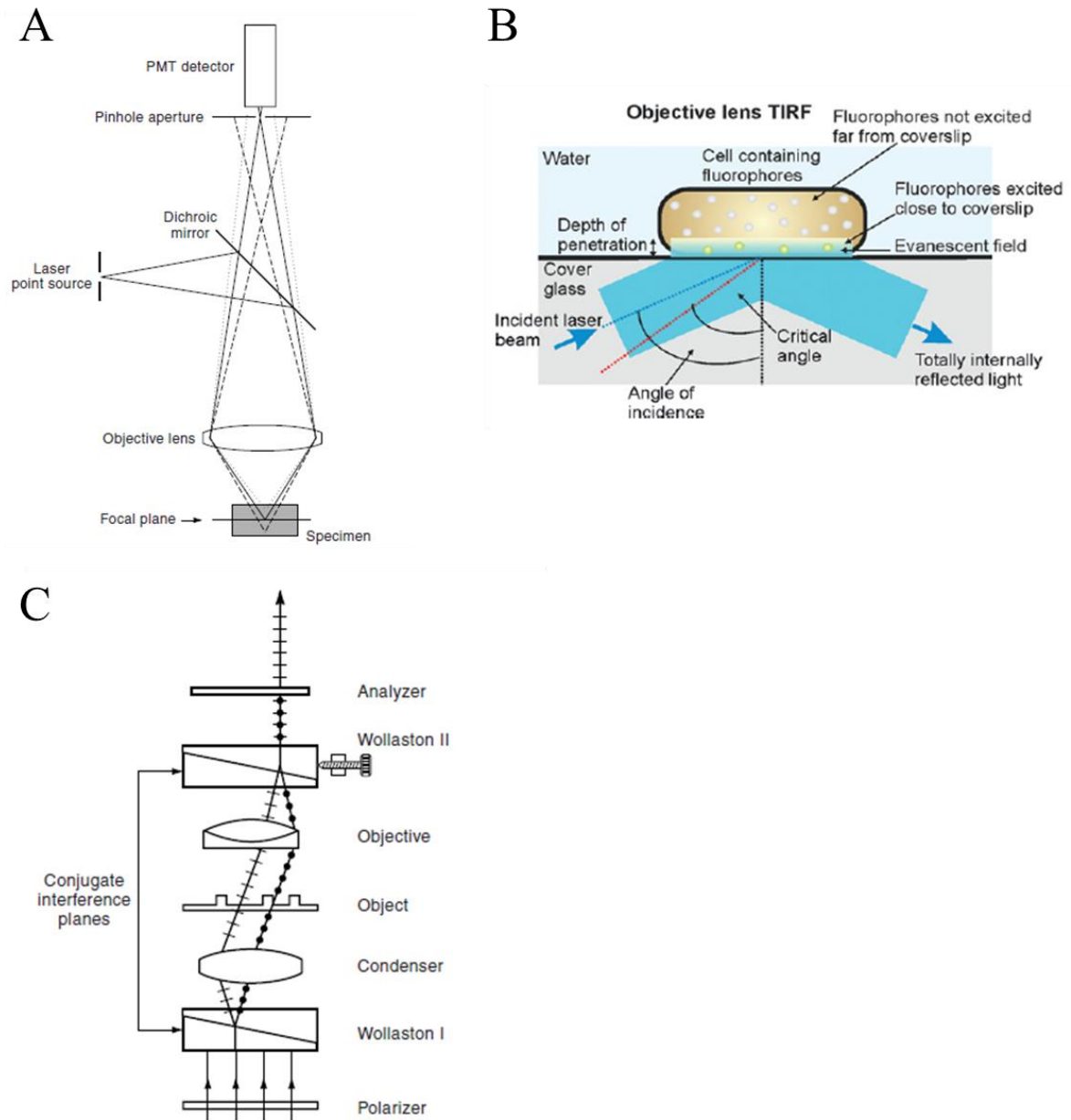


Figure 1.6. Modes of light microscopy for imaging mitosis. Schematics describing the working principles of (A) confocal microscopy (Reproduced from Murphy, 2001), (B) TIRF microscopy (Reproduced from Shashkova and Leake, 2017) and (C) DIC microscopy. (Reproduced from Murphy, 2001).

Label-free microscopy

As the name suggests, label-free imaging techniques generate contrast using inherent features of a colourless, unstained, transparent sample, without the use of fluorophores. Traditional label-free techniques such as Differential Interference Contrast (DIC) and phase-contrast (Zernike, 1953) allow the observation of cells and large subcellular structures in their

native, unperturbed states with minimal exposure to light, thereby preventing phototoxicity. Phase-contrast microscopes make use of the phase shift in light induced by the refractive indices of components of the sample. In phase-contrast images, objects appear uniformly dark over a relatively lighter background and with a characteristic outer halo. DIC microscopes employ dual-beam interference optics to improve contrast (Figure 1.6C). As a result, the DIC image of an object is a combination of light and dark regions that gives a pseudo-3D effect (Figure 1.5C). The use of DIC microscopy is especially advantageous as it allows users to focus on thin axial sections of the specimen and the high contrast generated in these images helps to easily discern single particles from aggregates (Li et al., 2007).

Modern day microscopes equipped with advanced cameras can acquire images and videos at high spatiotemporal resolution. Microscopy can thus rapidly generate hundreds of images from a single experiment leading to gigabytes of complex data. Manually making sense of this data is not only tedious, time-consuming and subjective but may also lead to erroneous interpretation owing to the possible existence of a viewer's bias. It is therefore useful to augment advanced imaging techniques with robust and automated image analysis tools that can efficiently process image data and accelerate investigation in cell biology.

1.3. Computational analysis of microscopy images

A digital image is made up of a finite number of discrete, equally sized units called 'picture elements' or 'pixels'. Each pixel possesses spatial coordinates (x,y) and an amplitude that corresponds to the intensity of light collected from the sample at that (x,y) position. Digital image analysis involves the use of computers to process images in order to mine the wealth of information stored in them and extract useful quantitative information (Gonzalez and Woods, 2008). The data deluge that results from microscopy experiments necessitates the rapid analysis of images on a high-throughput scale. Automation of image analysis helps not only to reduce manual intervention but also provides unbiased, reproducible measurements of the morphology and behaviour of the objects in terms of motion, concentration and interaction with other objects. Automated image analysis finds applications numerous fields, some examples of which are biology, biomedicine, astronomy, geology, remote sensing and robotics.

Since over a decade, the importance of computational image analysis in cell biology is increasingly being recognized. As a result, a plethora of image analysis techniques and tools are now available for researchers in order to quantitatively investigate the dynamics of cells

and intracellular molecules. Kymography and single particle tracking are two classic techniques fundamental to image analysis that are most commonly employed to explore the biophysical aspects of various biological processes, ranging from intracellular dynamics to the characterization of cell motility and migration. In Chapters 3, 4 and 5, I shall discuss in detail the software tools I have developed in order to automate quantitative kymography and 2D particle tracking in labelled and label-free images.

Microscopy data is inherently noisy. Noise in the context of image analysis is random variation in the intensity of an image. It can stem from several sources including fluctuations in the image sensor, thermal vibrations at the microscopy setup, errors in quantization and photon counting (Pawley, 1995). Data is therefore often denoised by specialized image-processing techniques such as median filtering and averaging prior to analysis (Gonzalez and Woods, 2008). The limit imposed by diffraction and the presence of noise in light microscopy data makes it important to test the robustness and accuracy of image analysis programs that automatically quantify parameters from such data.

Accuracy, precision and error

Accuracy of a tool is a measure of how close the output gained from the tool is to the actual or 'true' value (Waters, 2009). The deviation between the true value and the output is what we refer to as error. Error may depend on particle size and density, the quality of the hardware used for imaging and acquisition, image noise and even the algorithm used for analysis. The most accurate tool is the one that results in the lowest error. Precision, on the other hand, is a measure of how close the outputs from repeated runs of a tool on the same data are, to each other.

As simulations offer a true value of a parameter for comparison, image analysis tools are validated using simulated data. Owing to the lack of a true value of quantifiable parameters in biological image data, manual measurements are considered as gold standards during validation of automated tools. Additionally, one may compare the output generated by image analysis to other methods of quantification reported in previous literature.

The image analysis tools I describe in Chapters 3, 4 and 5 are rigorously validated with simulated noisy data, tested on experimental image time-series and benchmarked by comparing their results with manual measurements, published literature and outputs of other software.

To summarize, the computational analysis of image data obtained from *in vitro* and *in vivo* microscopy provides much needed quantitative insights into biological problems. The objective, high-throughput and reproducible quantitation provided by automated image analysis sets the foundation for mathematical models and simulations that could further improve our understanding of cellular and subcellular dynamics.

1.4. Simulation of cytoskeletal and spindle dynamics

The modularity of the cytoskeleton and the stochasticity associated with its dynamics has attracted scientists to model processes involving the cytoskeleton. Extensive theoretical studies have been carried out towards modeling aspects of mitosis (reviewed by Mogilner et al., 2006). Coarse-grained computer simulations based on constrained Langevin dynamics (Nedelec and Foethke, 2007) enable the reconstitution of the components of cytoskeletal spindles *in silico* in order to understand their collective behaviour. For instance, such simulations have been employed to shed light on self-organization of MTs and motors (Nedelec et al., 1997), spindle assembly (Loughlin et al., 2010; Nedelec, 2002) as well as spindle positioning (Kozlowski et al., 2007). In conclusion, a systems-biology approach that relates subcellular dynamics to individual and population level properties and combines experiments with quantitative analysis and computer simulations is essential in order to address some of the long standing questions in biology.

1.5. Organization of the thesis

The thesis is organized in two sections. The first part focuses on the development of tools for automated quantitative image analysis of microscopy data. The second part describes how these tools have been applied to study certain aspects of mechanics of cytoskeletal spindles in eukaryotic and prokaryotic cell systems through quantitative image analysis and simulations.

1.5.1. Computational tool development for automated image analysis

In Chapter 3, I describe a novel software tool for Automated Multi-peak Tracking Kymography (AMTraK), which uses peak information and distance minimization to track and automatically quantify kymographs from *in vitro* and *in vivo* fluorescence microscopy time-series of subcellular dynamics. Chapters 4 and 5 describe Fluorescence Tracker (FluoreT) and Differential Interference Contrast Object Tracker (DICOT) respectively, which are software tools I developed for automated single particle tracking in 2D in labelled and label-free image-series.

1.5.2. Applications: Spindle mechanics

In Chapter 6, we use a novel, non-invasive microrheology approach to estimate the cytoplasmic viscosity of multiple nematode zygotes. To this end, we apply DICOT (described in Chapter 5) to trace endogenous yolk granules imaged within live zygotes by time-lapse DIC microscopy. In Chapter 7, we aim to understand the effect of dynamic instability of ParM filaments on spindle assembly using Brownian dynamics based simulations. Additionally, in an attempt to understand the potential role of filament sliding in segregation, we quantify for the first time to our knowledge, the *in vitro* sliding parameters of ParM filaments. To this end, we employ AMTraK (described in Chapter 3).

Chapter 2

Materials and Methods

2.1. Implementation of algorithms

The computational image analysis tools (AMTraK, FluoreT and DICOT) were implemented in MATLAB R2014b and R2016a (MathWorks Inc., USA) in combination with the Image Processing toolbox (version 7.0 and above) and Statistics toolbox (version 7.3 and above) and tested on Linux, Mac OSX and Windows 10 platforms.

2.2. Pre-processing of image data from microscopy

The acquired time-series and movies taken from published data were converted to uncompressed TIF time-series using ImageJ version 1.4 (Schneider et al., 2012) and an online converter for MOV files (<https://video.online-convert.com>). Microtubule images with ‘salt and pepper’ noise were de-noised with a 3 x 3 median filter. Median filters work by replacing the intensity of each pixel by the median value calculated from its neighbourhood. Image contrast was enhanced by normalization (considering 0.3% saturated pixels) and brightness was adjusted using ImageJ and Fiji (Schindelin et al., 2012). Normalization stretches the intensity-histogram of the image to span the entire range of grayscale values allowed by the image type. The intensity of each pixel in the input image (I_{in}) is modified as follows:

$$I_{out} = (I_{in} - c) * [(b - a) / (d - c)] + a \quad (\text{Equation 2.1})$$

Here, I_{out} is the modified intensity, c and d are minimal and maximal intensities in the input image respectively and a and b are the lower and upper limits of grayscale values of the image (for example, for an 8-bit image, $a = 0$, $b = 255$). A non-zero value of saturated pixels improves contrast by reducing the effect of outlying pixel-intensities during normalization.

2.3. Simulating fluorescence bead images

In order to validate the automated tools for analysis of fluorescence microscopy data, we simulated bead-like circular structures by creating 8-bit images in MATLAB (MathWorks Inc., USA) with a black background (intensity: 0) with single white pixels (intensity: 255) placed in specific positions. To resemble the convolution effect of microscopy, the images were further filtered using a 5 x 5 disk filter and smoothed using a 3 x 3 averaging filter.

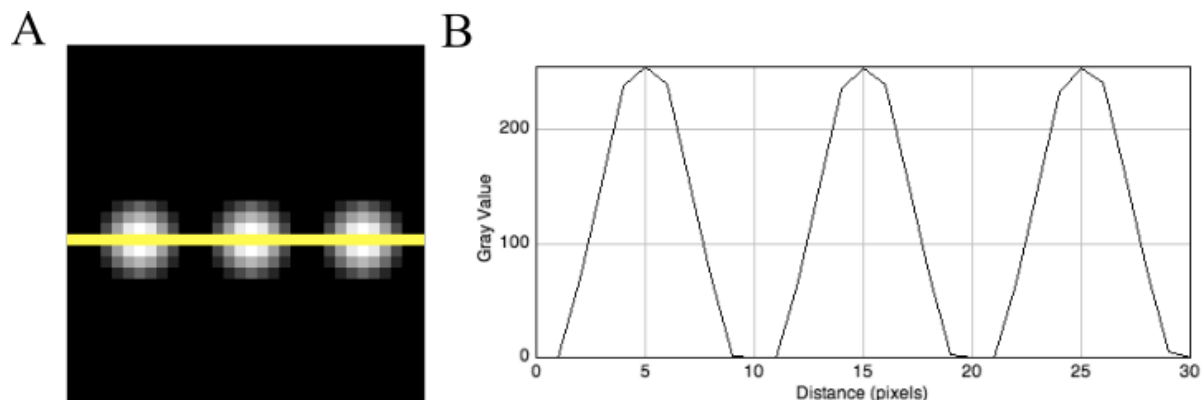


Figure 2.1. Simulated images. (A) A simulated bead image used to estimate the accuracy of image analysis tools developed for fluorescence microscopy. A profile through the image (yellow line) is used to generate (B) an intensity profile through the three beads.

The resulting circular objects (Figure 2.1A) have intensity profiles (Figure 2.1B) that resemble point sources of fluorescence signal. The time-series were saved as multi-page TIF files. Increasing levels of complex noise, a combination of Poisson and Gaussian noise, was added to individual images/time-series using ImageJ (Schneider et al., 2012). Poisson (shot) noise was introduced first using the ‘Poisson Noise’ plugin (Gallo, 2008). Gaussian noise was added using a filter with mean= 0 and increasing standard deviation (0-60) with the aid of the ‘Add specified noise’ feature.

2.4. Calculation of signal to noise ratio

The signal to noise ratio (SNR) was calculated for each image in a simulated time-series using the following equation, and then averaged:

$$\text{SNR} = \frac{\mu_s - \mu_b}{\sigma_b} \quad (\text{Equation 2.2})$$

While μ_s and μ_b are the mean intensities of the signal and background respectively, σ_b represents the standard deviation of the background intensity.

2.5. Otsu’s thresholding

In Chapters 3 and 4, automated thresholding for segmentation was carried out by Otsu's method that makes use of the gray-level histogram of images to dichotomize the pixels into background and foreground classes. The threshold level that maximizes inter-class variance (or minimizes intra-class variance) in pixel intensities is chosen as the optimal threshold (Otsu, 1979).

2.6. Centroid detection

The position of centroid or center-of-mass of a detected particle is calculated as follows:

$$C(x,y) = \left(\frac{\sum_{i=1}^n x_i}{n}, \frac{\sum_{i=1}^n y_i}{n} \right)$$

n is the number of pixels comprising the detected particle.

2.7. Nearest-neighbour tracking

In successive frames of an image-series, position coordinates that are closest in terms of distance and time are linked to make up a trajectory. This method is computationally less intensive and generally applicable and works best with low density of particles whose velocity of movement is lesser than the inter-particle spacing. Modified forms of this method have been used for tracking in the tools described in this thesis. The details of implementation are given in Chapters 3, 4 and 5.

2.8. Data analysis

All data analysis and plotting was performed using MATLAB 2014b and 2016a (MathWorks Inc., USA). Fitting of custom functions was performed using either the Levenberg-Marquardt non-linear least square routine or the trust-region method, implemented in the Curve-Fitting toolbox (version 3.5 and above) of MATLAB.

2.9. Estimation of effective diffusion coefficient

The effective diffusion coefficient (D_{eff}) of particles was estimated by two methods described in the following text.

2.9.1. Mean Square Displacement (MSD) analysis

Mean square displacement ($\langle r^2 \rangle$) of particles was calculated as described in (Khetan and Athale, 2016) using the Cartesian coordinates (x,y) obtained from AMTraK, FluoreT and DICOT.

$$\langle r^2(\delta t) \rangle = [x(t + \delta t) - x(t)]^2 + [y(t + \delta t) - y(t)]^2 \quad (\text{Equation 2.3})$$

In the above equation, r is the displacement of the particle at two time-points separated by a time-step δt that ranges from the minimal time-step in experiment to $3/4^{\text{th}}$ of the length of the trajectory.

D_{eff} was calculated by fitting the average MSD profile (as a whole or its linear portion, based on user input) to the anomalous diffusion model as follows:

$$\langle r^2 \rangle = 2nDt^\alpha \quad (\text{Equation 2.4})$$

Here, n is the number of dimensions ($n = 1$ for AMTraK; $n = 2$ for FluoreT and DICOT), t is the time-step and α is the anomaly parameter that indicates the nature of diffusion. The motion is said to be purely diffusive if $\alpha = 1$, sub-diffusive or ‘restricted’ when $\alpha < 1$ and super-diffusive or ‘transported-like’ when $\alpha > 1$.

2.9.2. Perrin’s method

It applies to particles undergoing pure Brownian motion with equal probability of being displaced in the X and Y directions. In order to calculate the D_{eff} by Perrin’s method (Perrin, 1910), Δx and Δy values are calculated from the Cartesian coordinates (x,y) of particle trajectories.

$$\Delta x = x(t) - x(t + \delta t); \quad (\text{Equation 2.5})$$

$$\Delta y = y(t) - y(t + \delta t)$$

Here, δt is the time-step. A Gaussian fit to the distribution yields the mean (μ) and standard deviation (σ). For a purely diffusive particle, μ of the distribution of Δx and Δy values would be 0. The diffusion coefficient is calculated separately for X and Y directions using the following expression:

$$D_x = \frac{\sigma_x^2}{2\delta t} \quad (\text{Equation 2.6})$$

$$D_y = \frac{\sigma_y^2}{2\delta t}$$

The D_{eff} is then given by the average of D_x and D_y values.

2.10. Stokes-Einstein's equation for estimation of viscosity

Viscosity of the solvent (η_s) was estimated from the effective diffusion coefficient (D) and radius (r) of suspended spherical particles using the Stokes-Einstein's equation:

$$\eta_s = \frac{k_B T}{6\pi r D} \quad (\text{Equation 2.7})$$

Chapter 3

Automated Multi-Peak Tracking Kymography (AMTraK): A Tool to Quantify Subcellular Dynamics with Sub-Pixel Accuracy

Overview

Kymographs are widely used in cell biology to reduce the dimensions of a time-series in microscopy for both qualitative and quantitative insight into spatiotemporal dynamics. While multiple tools for image kymography have been described before, quantification remains largely manual. In this chapter, I describe a novel software tool for automated multi-peak tracking kymography (AMTraK), which uses peak information and distance minimization to track and automatically quantify kymographs, integrated in an intuitive graphical interface. The tool provides an objective and automated method for reproducible analysis of kymographs from *in vitro* and *in vivo* fluorescence microscopy time-series of subcellular dynamics.

3.1. Introduction

Kymographs, or space-time plots, have been extensively used to analyse subcellular microscopy time-lapse image data with improvements in microscopy. They have been used in the past to characterize organelle transport, cell division (Pereira and Maiato, 2010) and molecular motor motility, and the wide-range of applications could be the result of the reduced spatial dimensions of complex microscopy time-series. Most often however, kymography has been used as a qualitative readout of movement or dynamics. In studies where kymographs have been quantified, this process has usually been manual, as seen in the Multi Kymograph plugin for ImageJ (Rietdorf and Seitz, 2008). The existing tools such as the automated kymography tool (Chetta and Shah, 2011) and ‘guided’ kymography (Pereira and Maiato, 2010) focus on automating the process of kymograph building. Few methods for the automated quantification of kymographs exist, such as ‘Kymomaker’ (Chiba et al., 2014) and a curvelet-based tool (Chenouard et al., 2010). Both these tools automate quantification, but cannot deal with merging and spitting events. Despite the ubiquitous nature of merging and splitting events in typical subcellular processes, none of the existing tools for the automated quantification of kymographs include a feature to handle budding and coalescence.

The reduced 1D analysis offered by kymography is found to be especially useful for the study of (i) bacterial DNA segregation, (ii) motor-driven filament transport, (iii) recruitment of proteins on membranes and (iv) vesicular transport in axons. Each of these scenarios is briefly reviewed in the following text.

Genome segregation is conserved across cellular systems and has been extremely well studied in the rod-shaped Gram-negative bacterium *Escherichia coli* (Skarstad et al., 1985; Nordström and Dasgupta, 2006). However microscopic analysis of DNA segregation has only recently been made possible with improvements in microscopy and image-analysis (Nielsen et al., 2006; Spahn et al., 2014; Sliusarenko et al., 2011; Reyes-lamothe et al., 2010). Given the almost 1D geometry of segregation of the genome along the long axis of the cell, kymography is a convenient way to analyse the process of nucleoid DNA segregation. Recent studies using explicit 3D tracking over time have found that compaction waves are associated with *E. coli* genome segregation (Fisher et al., 2013). Based on a reduction in dimensions to 1D over time, a quantitative kymograph-based analysis could be used to screen for changes and defects in segregation, without the need for more complex datasets and their analysis.

The process of microtubule transport by molecular motors reconstituted *in vitro*, referred to as a 'gliding assay' has been extensively used to examine the fundamental nature of multi-molecular transport of actin and microtubule filaments by motors (Howard et al., 1989; Nitzsche et al., 2010; Leduc et al., 2007; Toyoshima et al., 1987). Recent studies have also used 'gliding assays' to address microtubule mechanics based on the bending of filaments while undergoing transport (Martin, 2013). Kymography of cytoskeletal filaments *in vivo* has been used to follow actin contractility and microtubule buckling dynamics (Bicek et al., 2009). However in most cases the use of kymography has been limited to visualizing the time-series in a single-image, as a compact form of data representation. A general tool that could use this information to objectively extract the measures of motility would hence be of some use to these multiple applications.

The assembly of proteins by 'recruitment' to structures is fundamental in multi-protein complex formation. The assembly of vesicles by budding off membranes and their fusion is critical for cellular function. For the assembly of coated pits with clathrin for endocytosis, the site of assembly (Ungewickell and Branton, 1981), sequence of binding events (Avinoam et al., 2015) and interactions of other proteins (Skruzny et al., 2015) is considered to be critical. Microscopy of *in vitro* reconstituted membrane bilayers has become a powerful tool to study the dynamics of protein assembly during vesicle formation (Pucadyil and Schmid, 2010; Neumann et al., 2013). Proteins such as epsin, which were reported to

accelerate clathrin recruitment (Kalthoff et al., 2002) have been examined using kymography of the fluorescently labelled clathrin and the effect of mutant epsins on the process tested (Holkar et al., 2015). While such an approach lends itself to high-content screening, the analysis of the kymograph has been manual. Many other such recruitment dynamics studies could benefit from an automated routine to quantify the kinetics of assembly through intensity measurements coupled to kymography.

Neuronal vesicles are transported in axons by the action of molecular motors. Microscopy of *in vitro* reconstituted (Allan and Vale, 1991) and the *in vivo* transport in cultured cells (Welzel et al., 2011; Hill et al., 2004) has provided insights into both the components and forces regulating transport. Recent technical developments have allowed whole animal *in vivo* microscopy of subcellular vesicle movements in neurons (Mondal et al., 2011). In this and comparable studies, quantitative statistics have been obtained using manual detection of kymographs. This is possibly due to the complex nature of the time-series with cross-overs and the crowded *in vivo* environment. An approach that uses objective criteria and automates the process of quantification could provide valuable improvements to our understanding of fundamental nature of vesicle transport as well as aid in the process of modeling vesicle transport.

Here, we have developed a novel tool to automatically quantify kymographs from fluorescence image time-series. We proceed to demonstrate the utility of the automated multi-peak tracking kymography (AMTraK) tool by quantifying dynamics from diverse subcellular fluorescence microscopy data sets. These include bacterial genome-segregation, microtubule (MT) motility of 1D filaments and 2D radial asters, membrane protein assembly dynamics and vesicle transport in axons.

3.2. Materials and methods

3.2.1. Simulated test images of bead diffusion in 1D

Simulated images of static beads were generated as described in Chapter 2, Section 2.3. To simulate bead motion, a simple 1D random-walk was implemented. The initial position of every bead (x_0) was incremented in each frame as follows:

$$x_t = x_0 + vt \quad (\text{Equation 3.1})$$

Here, v is the speed assigned to the beads and x_t is the position of the bead after time t . For each time-series, the speed was varied and drawn from a normal distribution with a fixed mean $m = 0$ and standard deviation (s).

3.2.2. Microscopy of segregating nucleoids and kinesin-MT gliding assay

The dynamics of bacterial nucleoid segregation (experiment and microscopy performed by Manasi Gangan) were imaged using an inverted Zeiss LSM780 confocal microscope (Carl Zeiss, Germany) at 63x magnification. *E. coli* cells expressing plasmid-based HupA-GFP were grown on LB agar-pads at 37°C. The microtubule gliding assay (experiment and microscopy performed by Kunalika Jain) involved flowing in a mixture of TRITC-labelled and unlabelled tubulin that were previously taxol-stabilized, onto a cleaned glass slide with human kinesin (Cytoskeleton Inc., USA) following standard methods and imaged on a Zeiss Axiovert Z1 upright epifluorescence microscope at 40x magnification. Both experimental methods are described in greater detail in our publication (Chaphalkar et al., 2016).

3.2.3. Image pre-processing

Images of MT-gliding assays were de-noised using a 3 x 3 median filter in ImageJ. Images of bacterial nucleoid segregation were corrected for drift using the rigid body transformation in the StackReg plugin (Thévenaz et al., 1998) in ImageJ. The vesicle transport image time-series in *C. elegans* taken from supplementary material (movie S1) of Mondal et al., 2011 was converted from WMV to uncompressed TIF time-series using an online converter (<https://video.online-convert.com>) and ImageJ (Schneider et al., 2012). In the absence of a scale bar for this movie, the pixel size was calculated by first measuring the width of the axon of a posterior lateral touch neuron (PLM) from figure 1F in the same report. Using this value of axon width for calibration, the pixel size was determined to be 0.11 μm . Pixel sizes were provided by authors for the other published datasets (Holkar et al., 2015; Foster et al., 2015) analysed in this study. Signal to noise ratio of simulated images was calculated as described in Chapter 2.

3.2.4. Manual analysis of kymographs

For manual analysis, kymographs of MT-gliding made by AMTraK were processed using a custom script written in MATLAB (MathWorks Inc., USA). Lines were interactively drawn on each kymograph along the edges of the motion 'track' of a microtubule, using the *getline* function built in MATLAB. Position coordinates (x,y) were extracted over time from the drawn lines to calculate speed.

3.2.5. AMTraK implementation specifics

The automated multi-peak tracking kymography (AMTraK) code was implemented in MATLAB R2014b (MathWorks Inc., USA) in combination with the Image Processing (version 7.0) and Statistics (version 7.3) Toolboxes and tested on Linux, Mac OSX and Windows 10 platforms. The processing time taken by AMTraK varies in the range of a few seconds to a few minutes depending on the size of the input time-series and the number of tracks identified.

3.2.6. Data analysis

Data output from AMTraK was analysed for calculation of (a) displacement, (b) speed, (c) tortuosity, (d) MSD-based effective diffusion coefficient and (e) intensity-based time constant of assembly. All data analysis and plotting was performed using MATLAB 2014b and 2016a (MathWorks Inc., USA). Fitting of custom functions was performed using either the Levenberg-Marquardt non-linear least square routine or the trust-region method, implemented in the Curve-Fitting toolbox (version 3.5 and above) of MATLAB. The intensity kinetics plots (shown in Figure 3.8C, D) were fit to a single-phase exponential function, $y = a + (b - a) \times (1 - e^{-ct})$ to obtain the time constant of assembly $\tau = 1/c$. MSD-based effective diffusion coefficient in 1D was determined as described in Chapter 2, Section 2.9.1.

3.3. Algorithm and workflow

The automated multi-peak tracking kymography (AMTraK) is open source software based on an algorithm that combines peak detection and distance minimization based linking to quantify dynamics of fluorescence image time-series. The source code has can be accessed from: <http://www.iiserpune.ac.in/~cathale/SupplementaryMaterial/Amtrak.html>.

The program has a graphical user interface (GUI) front-end and is accompanied by a detailed help file. The algorithmic workflow (Figure 3.1) is divided broadly into three steps:

- (a) Making the kymograph
- (b) Peak detection and tracking
- (c) Statistics

These steps in the workflow are reflected in the graphical user interface (GUI) layout (Figure 3.2).

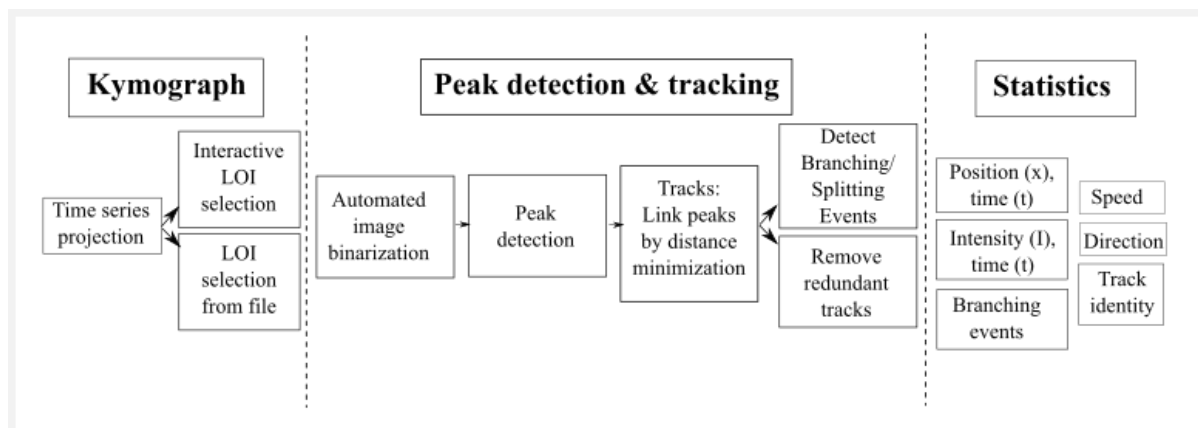


Figure 3.1. Algorithm workflow. The workflow of the algorithm involves three steps (1) kymograph generation, (2) peak detection and tracking and (3) quantification and the functions invoked by each part are elaborated.

The functioning of each of these steps is briefly described as follows:

(a) Making the kymograph:

The user chooses an input image time-series with the ‘Open File’ button. Image time-series are assumed to be uncompressed, multi-page TIF files (independent of bit depth). The user can choose to process either the whole or a subset of frames using the ‘Frame nos.’ text box. For example entering ‘2:2:8’ will now result in only frames 2, 4, 6 and 8 being processed for further analysis. The text box ‘Save as sub-folder’ takes a number input (default ‘1’) indicating where the outputs will be stored (e.g.: ‘./amtrak-1’). The drop-down menu ‘Apply LOI’ allows the user to either choose a line of interest (LOI) using the mouse (‘Interactive’) or apply a pre-existing LOI on a different channel (color) of the image time-series (‘From file’). Once an interactively drawn LOI is selected, it is stored in the output sub-folder as ‘LOIselection.txt’ (Table 1). This LOI can subsequently be applied, to another channel or the same region of another dataset (e.g.: microfluidics channels) using the ‘From file’ mode. For this, the user is required to load a separate TIF time-series using ‘Open File’ and change the sub-folder number in order to prevent overwriting old data. The ‘LOI width (pixels)’ allows a user to choose the width of the LOI, to compensate for occasional drift of the object, in a direction orthogonal to the LOI orientation. The choice widths- 1, 3 and 5 pixels- is centered around the selected LOI pixels, similar to that implemented in the ImageJ Multi Kymograph plugin (Rietdorf and Seitz, 2008). The drop-down menu ‘Units’ allows the user to select distance and time units, and the text boxes ‘Pixel size’ and ‘Time interval’ are used to provide conversion factors per pixel and frame respectively. This results in scaling the pixels

and frame numbers to physical units. The button ‘Make Kymograph’ produces a maximum intensity projection image of the input time-series, if the user had chosen the ‘Interactive’ mode (default) in the ‘Apply LOI’ menu. The user is required to select the line of interest by drag-clicking the mouse. Double-clicking or pressing the ‘Enter’ key on the keyboard ends the selection and throws a dialog box, which prompts the user to choose to either select more LOIs or continue with the processing of the one already selected. This generates file one or more ‘LOIselection.txt’ files in the sub-folders. If the ‘From file’ mode was selected, the program allows the user to select a pre-existing ‘LOIselection.txt’ from the directory structure. The program then generates kymographs based on these LOIs and stores the matrices corresponding to the LOIs in sub-folders numbered according to the sequence of LOI selection (e.g.: ‘/amtrak-1/’, ‘/amtrak-2/’ etc.).

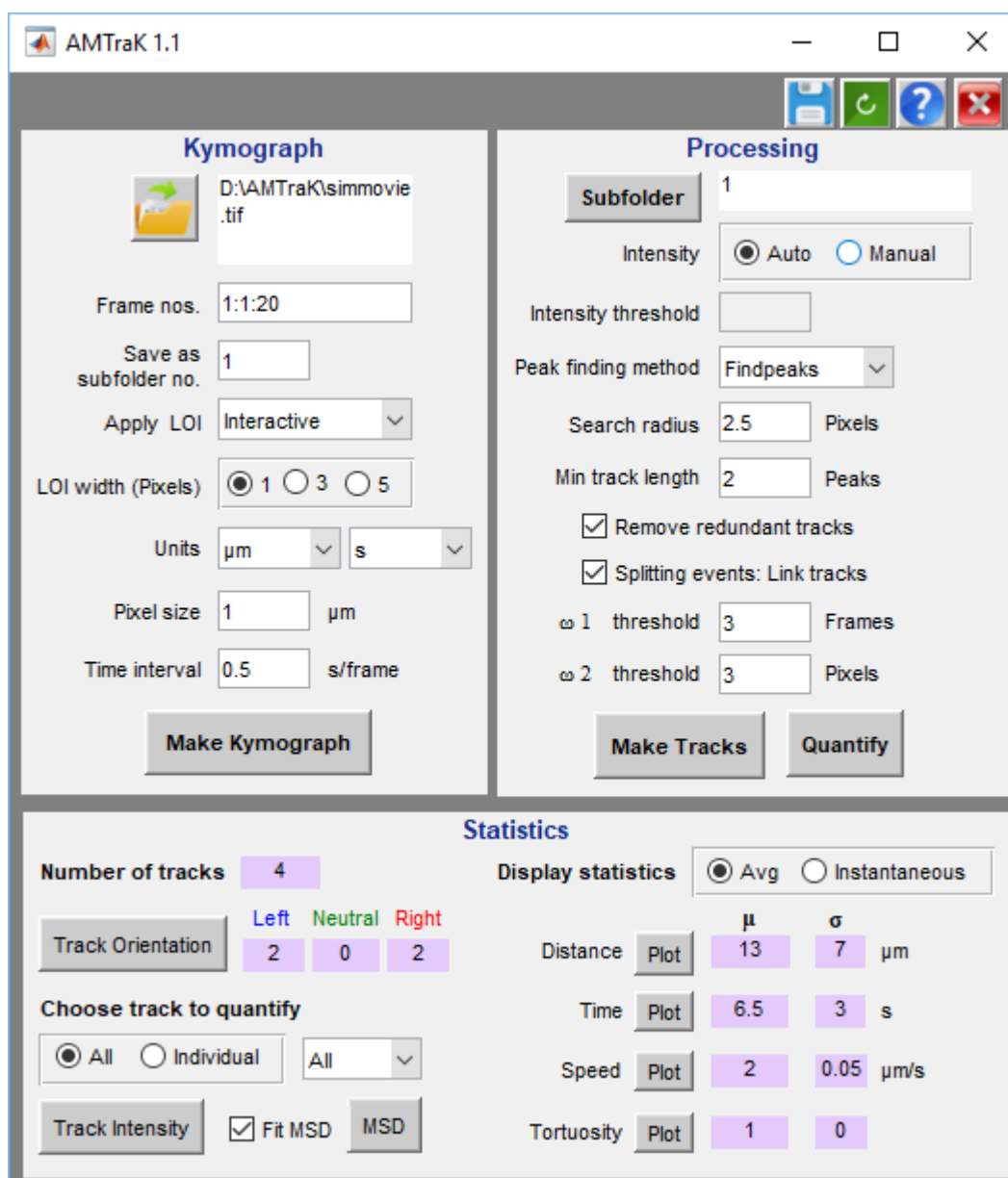


Figure 3.2. AMTraK user-interface. The GUI is organized to reflect the three workflow steps to generate and process a kymograph and display track statistics.

(b) *Peak detection and tracking:*

Detecting peaks: The button ‘Subfolder’ allows the user to choose the kymographs to be processed using ‘Add’, which adds the subfolders created earlier to the active list. Using this feature, a user can either process a single kymograph at a time, or process multiple kymographs using the same parameters. Based on the user’s choice, the kymograph is either auto-segmented row-wise using Otsu’s method (Otsu, 1979) (briefly described in Chapter 2, Section 2.5) or segmented with a manual input of ‘Intensity threshold’ that is a fraction in the range 0-1. The resulting binary image is processed for ‘Peak detection’. The user can choose between three alternative methods: (i) *findpeaks* (Brookes, Mike (Department of Electrical & Electronic Engineering, Imperial College, Exhibition Road, London, 2005) (default) and (ii) watershed (Meyer, 1994) to find central peaks, while (iii) Canny edge detection (Canny, 1986) is useful if the edge information is the most reliable descriptor of the dynamics. The *findpeaks* method makes use of the derivatives of a list of numbers to identify the position of ‘rises’ in them. In case of a plateau-like rise, *findpeaks* chooses the centre of the plateau as the peak. Typically *findpeaks* and watershed are ideal for spherical objects. Peak detection outputs an image of the kymograph with the peaks overlaid in color.

Linking: The list of peaks $P(t)$ for each time point t is linked resulting in tracks, based on user input parameters of ‘Search radius’ (λ_1) and ‘Min. track length’ (λ_2). Peaks are linked if the minimal pair-wise distance $d_j(t, t+\tau)$ between every j^{th} peak in successive rows ($t, t+\tau$) satisfies the condition $\min(d_j(t, t+\tau)) \leq \lambda_1$, iteratively for the j^{th} peak in every subsequent time step ($t + \tau$). If two or more peaks are equidistant, we implement linear approximation where the peak that makes the largest angle (0 to π) with the existing track is chosen. For the peaks in $t = 1$, the angle criterion does not hold true and equidistant peaks are resolved by user-input. The peaks that did not form a part of any track were treated as start-points of new tracks. Tracks are eliminated from further analysis if their number of peaks linked $\text{len}(P) \leq \lambda_2$, to avoid artifacts due to very short tracks.

Remove redundant: If the checkbox ‘Remove redundant tracks’ is selected, each i^{th} track with η_i coordinates, is tested for intersections using the inbuilt *intersect* function. If the number of

common coordinates (η_c) satisfies the condition $\eta_c \geq (\eta_i / 3)$, it is eliminated as a redundant track.

Splitting and joining tracks: If the checkbox ‘Splitting events: Link tracks’ is selected, events where two tracks merge are identified by a two-step process. First, all endpoints of tracks ($I(x,t)$) are evaluated for the condition:

$$I(x,t) = (d_e^t \leq \omega_1) \text{AND} (d_e^x \leq \omega_2) \quad (\text{Equation 3.2})$$

Here, d_e^t is the distance on the time-axis (t) and d_e^x is the distance on the spatial (x) axis. Then, a peak (J_m) with the minimal (Euclidean) distance to the end-point is selected to link the two tracks. The time and distance thresholds are set by the user in the text box for ω_1 (frames) and ω_2 (pixels) respectively.

Invoking the button ‘Make tracks’ links the peaks based on the input parameters, while the button ‘Quantify’ produces text files corresponding to each track (Table 3.1).

(c) Statistics:

This section of the code produces both text-file outputs and plots of the dynamics estimated from the kymograph. The user may choose to display statistics of ‘All’ tracks or a specific ‘Individual’ track picked from the drop-down menu. Similarly, the flexible display allows the user choose between ‘Average’ and ‘Instantaneous’ values of motility parameters. In case of the former, the frequency distribution of Distance, Time, Speed and Tortuosity (i.e. directionality) are plotted if the button ‘Plot’ corresponding to these variables is pressed. Additionally, the mean (μ) and standard deviation (σ) of these variables are also generated in the text boxes. Pressing the ‘Track Intensity’ button plots the normalized (0-1) grey value intensity of each track as a function of the time. The button ‘Track orientation’ triggers a recoloring the tracks in the kymograph based on the net direction of movement along the X-axis- blue (negative, left), red (positive, right) and green (stationary, neutral). The number of tracks following respective directions is displayed in the text boxes adjacent to the button.

Mean square displacement analysis of all detected tracks is performed on pressing the ‘MSD’ button. A window with the plot of the average MSD against increasing time-step is displayed. Ticking the ‘Fit MSD’ option *a priori* helps the user to extract the value of the average one-dimensional diffusion coefficient by fitting the entire or a fraction of the average MSD curve to the anomalous diffusion equation (See Chapter 2, Section 2.9.1).

Outputs of the analysis are stored in multiple tab-delimited text files to enable reproducible analysis and are summarized in Table 3.1.

Table 3.1. Description of output files generated by AMTraK

Function	Sr. No.	Output file	Description
Make Kymograph	1	OutputKymo.txt	The kymograph matrix
	2	OutputKymo.tif	The kymograph image
	3	LOIselection.txt	(x,y) Coordinates of Line of Interest
	4	LOIselection.tif	LOI overlaid on projected image-stack
Detect Peaks	5	Peaks.tif	Peaks overlaid on the kymograph
	6	Brightcoords.txt	(x,y) Coordinates of peaks detected in the kymograph
Make Tracks	7	PlotContour.tif	Tracks overlaid on the kymograph
	8	Tracklist.txt	(x,y) Coordinates and intensity of tracks detected in the kymograph
	9	Branchpoints.txt	Intersecting tracks and their branch points
Quantify	10	OutputStats.txt	Summary of particle movement statistics
	11	USER_InstStats.txt	Instantaneous (stepwise) statistics of each track
	12	USER_TrackStats.txt	Averaged statistics of each track
Track Orientation	13	Track_Orientation.txt	Directions indicated against track numbers
	14	Track_Orientation.tif	Colour-coded tracks overlaid on kymograph, red=right, blue=left, green= neutral
Track Intensity	15	Track_Intensity.tif	Intensity profiles of each track
MSD	16	MSD_vs_Time.tif	Mean square displacement profiles
	17	AvgMSD_vs_Time.tif	Average MSD curve with fit
	18	ID_Time_MSD.txt	Trackwise MSD
Save Parameters	19	All_Parameters.txt	Record of kymograph making and processing parameters

3.4. Results

3.4.1. Accuracy of detection

To test the positional detection accuracy of the algorithm, we created simulated image time-series of linearly aligned, equidistant, circular objects that represent typical fluorescence images of objects (Figure 3.3A, Figure 2.1A) comparable to subcellular structures.

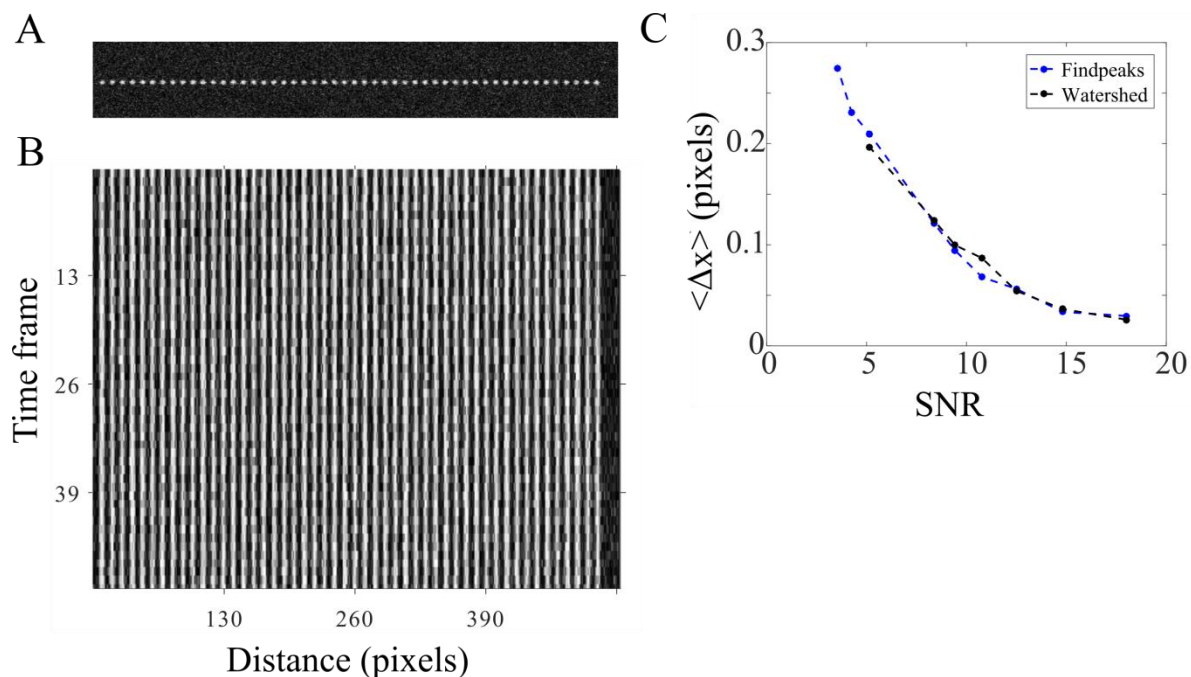


Figure 3.3. Estimating positional accuracy. (A) A single frame of a 2D image time-series of static spheres (with a peak intensity of 1) with Poisson and Gaussian noise (Signal to noise ratio 3.55) is analysed using AMTraK (B) resulting in a kymograph. (C) The mean error of detection in pixel units ($\langle \Delta x \rangle$) is plotted as a function of the signal to noise ratio (SNR) for the *findpeaks* (blue) and watershed (black) methods.

Since the time-series consists of the same image, the objects are static and the expected kymograph would show straight lines that do not deviate in their path. However, addition of complex noise, a combination of Poisson and Gaussian noise (described in Chapter 2, Section 2.3), results in intensity variations as seen in the kymograph (Figure 3.3 B). The difference between the position of the detected tracks (x_D) and the simulated position (x_S) is used as an estimate of the limit of accuracy in position detection:

$$\Delta x = |x_S - x_D| \quad (\text{Equation 3.3})$$

Increasing levels of noise were added to the time-series and the mean error in position detection was estimated. The SNR was calculated as described in Section 2.4. The mean error ($\langle \Delta x \rangle$) was found to be less than 1 pixel using both, the *findpeaks* and the watershed method (Figure 3.3C) in the given range of SNRs. In low SNR (3.56) conditions (Cheezum et al., 2001), *findpeaks* performed best and resulted in tracks of equal and unaltered lengths.

To test if motility affects the positional accuracy, we also evaluated the positional accuracy of particles undergoing a random walk (described in the Materials and Methods section) with a

fixed image noise (SNR 5.1). By increasing the SD of the random walk we estimated the effect of increasing velocity on Δx (Figure 3.4A). The error of positional detection ($\langle \Delta x \rangle$) using the findpeaks and watershed methods, as before, was found to be less than 1 pixel for the chosen range of velocities of the random walk (Figure 3.4B).

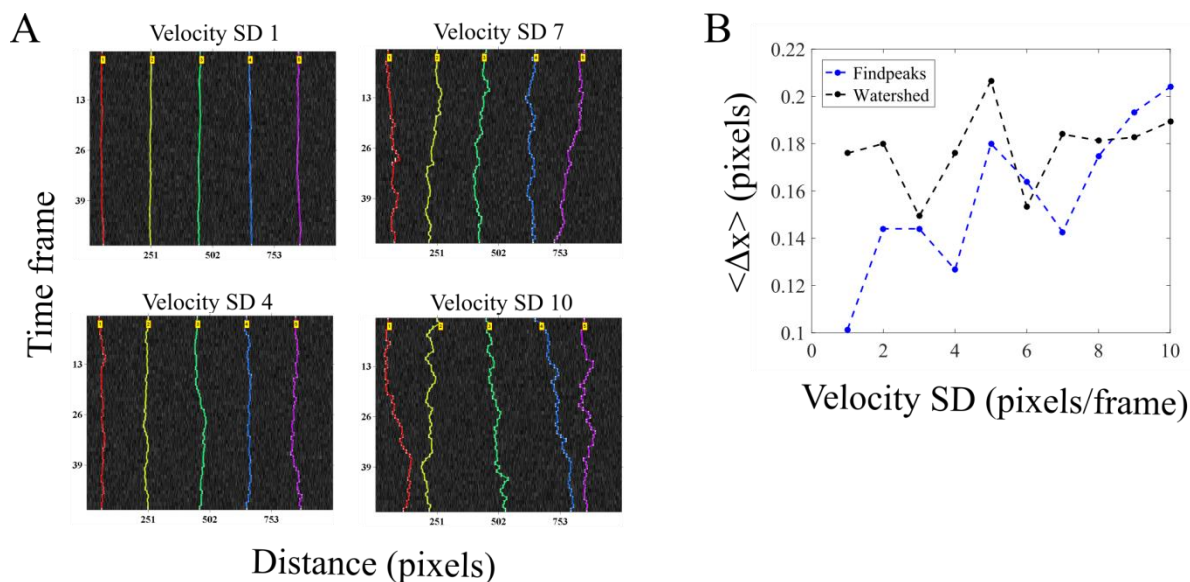


Figure 3.4. Positional accuracy of tracking simulated motility. (A) Kymographs of time-series of spheres undergoing a 1D random walk SNR 5.1 were tracked. The colors indicate the detected tracks. (B) The arithmetic mean of error in position detection (Δx) from *findpeaks* (blue) and watershed methods (black) over 3 iterations of the time-series is plotted for increasing velocity of the random-walk as inferred from the standard deviation (SD).

Tracking errors accumulate at higher velocities, suggesting that image noise is the major limiting factor for the positional accuracy of detection, independent of particle motility. Thus, while AMTraK analysis can result in sub-pixel accuracy of position detection, it is essential that the input data have low-noise. We proceeded to test our method on the multiple experimental datasets to examine the utility of this program involving bacterial DNA segregation, microtubule motility, vesicle assembly and transport dynamics.

3.4.2. Detecting splitting events in bacterial DNA-segregation

A time-series of growing *E. coli* is acquired in fluorescence and DIC to follow the nucleoid segregation dynamics of HupA-GFP labeled DNA (Figure 3.5A). Using the maximum intensity projection produced from AMTraK, the LOIs are chosen (Figure 3.5B) and used to generate and analyze two kymographs (Figure 3.5C, D). The segregation of the genome is captured by the branched structures of the tracks marked in the kymographs.

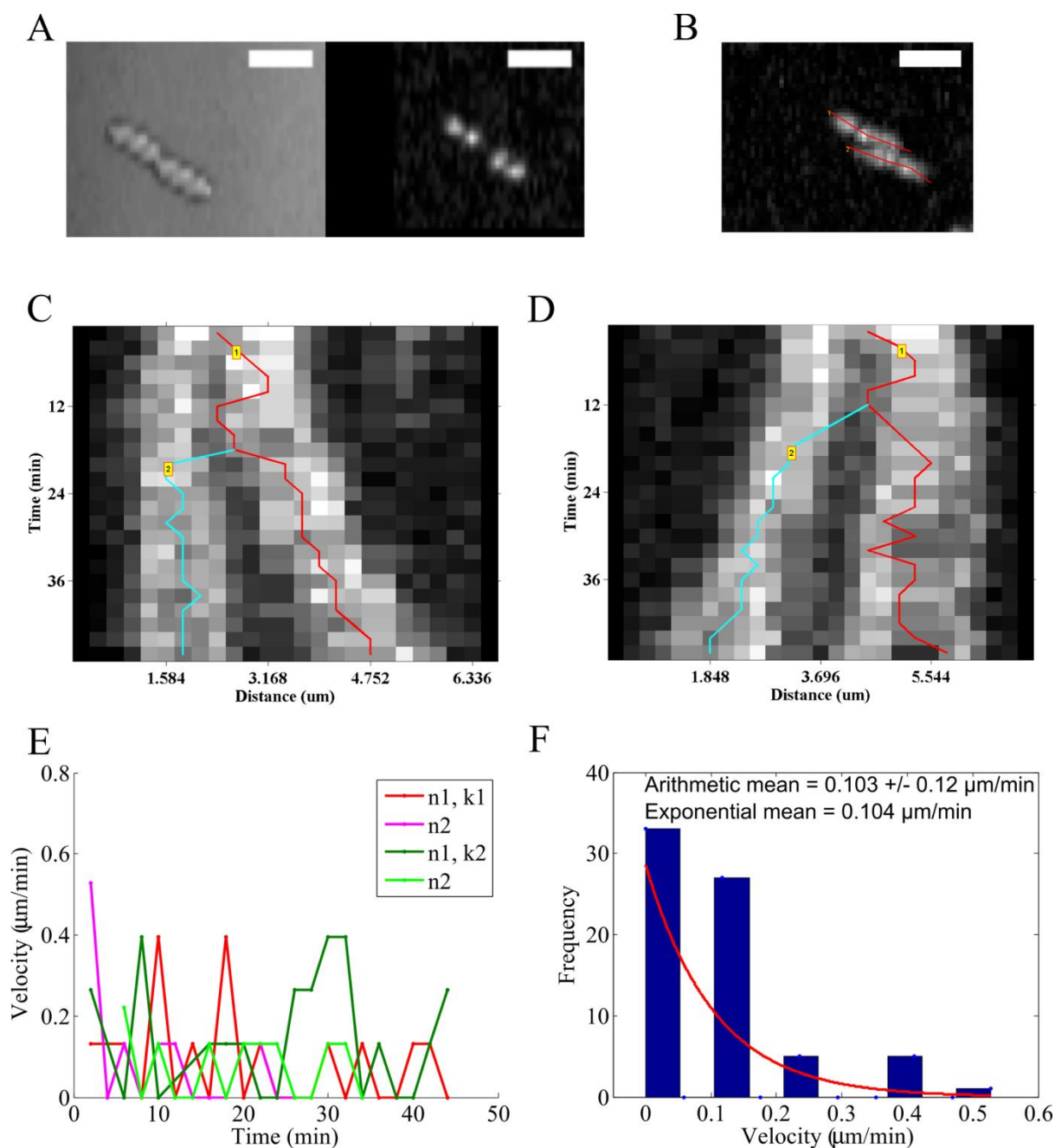


Figure 3.5. Nucleoid segregation dynamics of *E. coli*. (A) Image time-series of *E. coli* MG1655 grown on agar pads and imaged in DIC (left) and fluorescence based on HupA-GFP (right) are analyzed using AMTraK. (B) AMTraK generates a maximum intensity projection on the basis of which user-selected lines of interest (red lines) are used by the program to generate kymographs. The kymographs based on (C) LOI 1 (k1) and (D) LOI 2 (k2) were tracked resulting in branched tracks (colored lines). (E) The instantaneous velocities of nucleoids 1 and 2 (n1, n2) from kymographs 1 (k1) and 2 (k2) are plotted as a function of time (colors indicate nucleoids n1, n2 each from the kymographs k1, k2). (F) Mean velocities are estimated using both the arithmetic mean (\pm s.d.) and v_{ex} , the mean of the exponential decay ($y = e^{-1/v_{ex}}$) that was fit (red line) to the frequency distribution of instantaneous velocity (bars). Scale bar 4 μ m.

Additionally we can evaluate both the instantaneous velocity for time-dependence (Figure 3.5E) and average statistics (Figure 3.5F). The mean nucleoid transport velocity is $0.103 \pm 0.12 \mu\text{m}/\text{min}$ (arithmetic mean \pm SD). Based on the form of the frequency distribution of instantaneous velocities, we also fit an exponential decay function to obtain the exponential mean velocity $v_{\text{ex}} = 0.104 \mu\text{m}/\text{min}$. These values of nucleoid movement speed from *E. coli* MG1655 (wild-type) cells are comparable to a previous report in which nucleoids were tracked in 3D over time (Fisher et al., 2013). While nucleoids form a diffraction-limited spot in microscopy images, un-branched cytoskeletal filaments form typical 1D structures and dynamics of transport on them and of the filaments themselves, are ideally suited for kymography.

3.4.3. Microtubule transport: filament edges, centers and time-dependence of velocity

The transport of microtubule (MT) filaments by surface-immobilized molecular motors in the presence of ATP and buffers is referred to in the literature as a ‘gliding assay’ or ‘collective transport assay’. Here, we analyze the gliding motility of MT on kinesin, as described in the methods section, using AMTraK. The analysis of a representative kymograph using either peak- (Figure 3.6A) or edge-detection (Figure 3.6B) successfully traces the centroids and edges respectively.

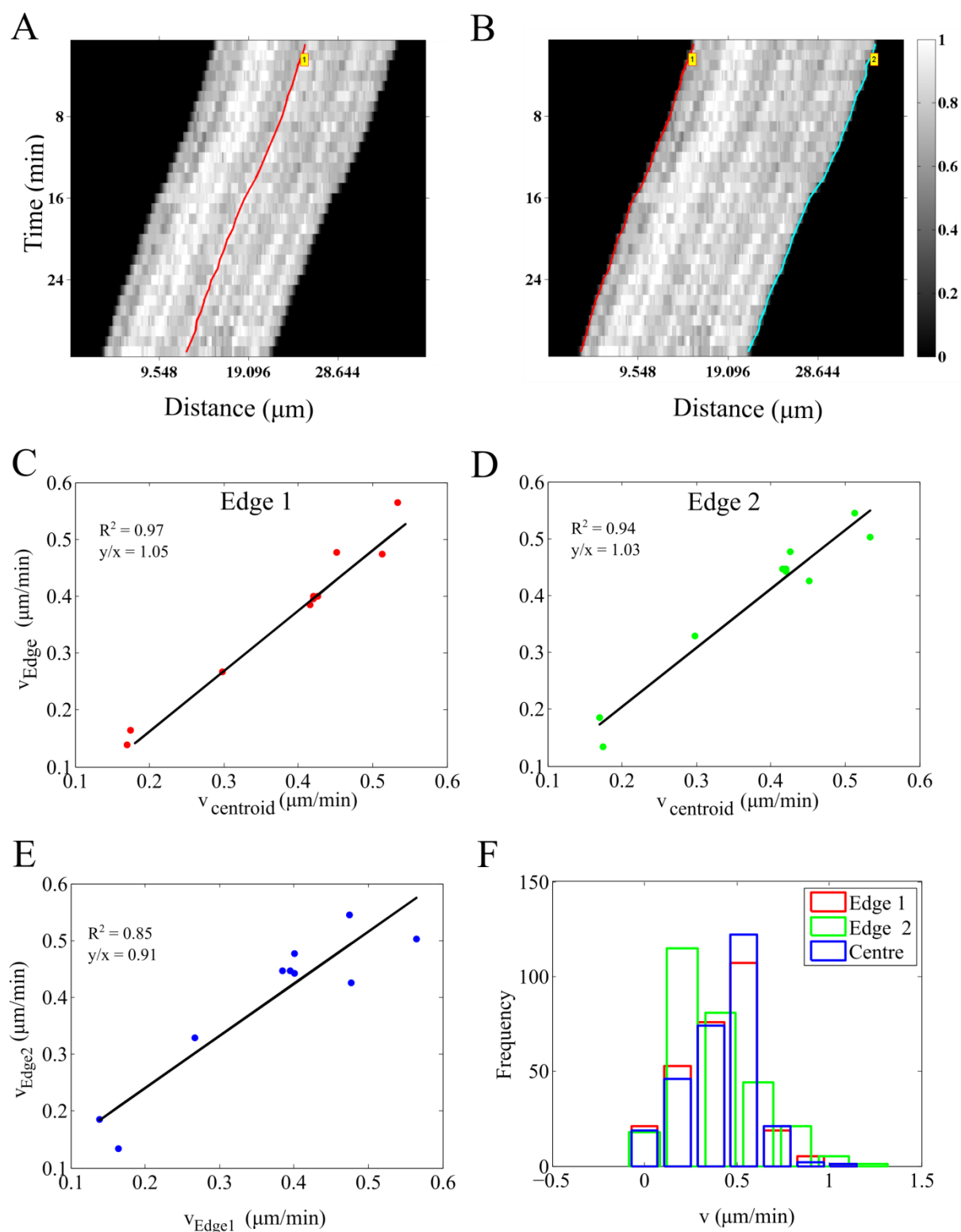


Figure 3.6. Microtubule (MT) gliding motility on kinesin motors. MTs gliding on kinesin (images acquired every 1 minute for 30 minutes) were analyzed using AMTraK by either detecting **(A)** the centerline (red) or **(B)** the two edges the filament, edge 1 (red) and 2 (cyan). Color bar: gray scale image intensity normalized by the maximal value for the bit-depth. **(C, D)** The velocity estimates from the centroid-based velocity estimates and the two edges and **(E)** the velocities estimated from each edge are correlated. **(F)** The frequency distribution of the instantaneous velocity estimates using

the centroid (blue) is compared to edge-based estimates. r^2 : goodness of fit, y/x : slope of the linear fit. Number of filaments analyzed, $n=10$.

The mean velocity estimates for collective motor transport show variations between individual filaments. The centroid and edge velocity estimates of multiple MT filaments ($n=10$) are strongly correlated as evidenced by the straight line fit with slope ~ 1 (Figure 3.6C, D), as expected. However, the linear correlation of edge-based velocities has a slope of ~ 0.9 (Figure 3.6E), suggesting small deviations from the ideal slope, within the range of the average positional detection error (Figure 3.3C). While typical kymograph analysis of cytoskeletal transport averages the edge information (movement of the tips over time), correlating edge-velocities could potentially be used to estimate small alterations in the filament geometry such as bending and length change. The mean velocity of $0.5 \mu\text{m}/\text{min}$ obtained from our analysis of the assay (Figure 3.6F) is consistent with previous reports for the same construct (Cytoskeleton, 2005; Stewart et al., 1993). While the transport of effectively 1D MT filaments lends itself to kymography, we proceeded to investigate if 2D radial MT structures or asters can also be analyzed by kymography.

3.4.4. Fusion of MT asters

In recent experiments by Foster et al. (Foster et al., 2015) they examined the spontaneous contraction dynamics of radial MT arrays or asters labeled with Alexa647-tagged tubulin, in *Xenopus* egg extracts. We have taken a time-series of such asters from published data (kindly shared by the author Peter J. Foster) and analyzed coalescence events using AMTraK (Figure 3.7A) The projection of the time-series for selecting the LOI enables us to reduce the complex movements of such 2D structures to a 1D over time process. The movement of the smaller aster as it merges with the larger one is rapid. The fluorescence intensity following the merger fluctuates but does not increase, which we interpret to mean tubulin density at the center of the new aster does not increase (Figure 3.7B).

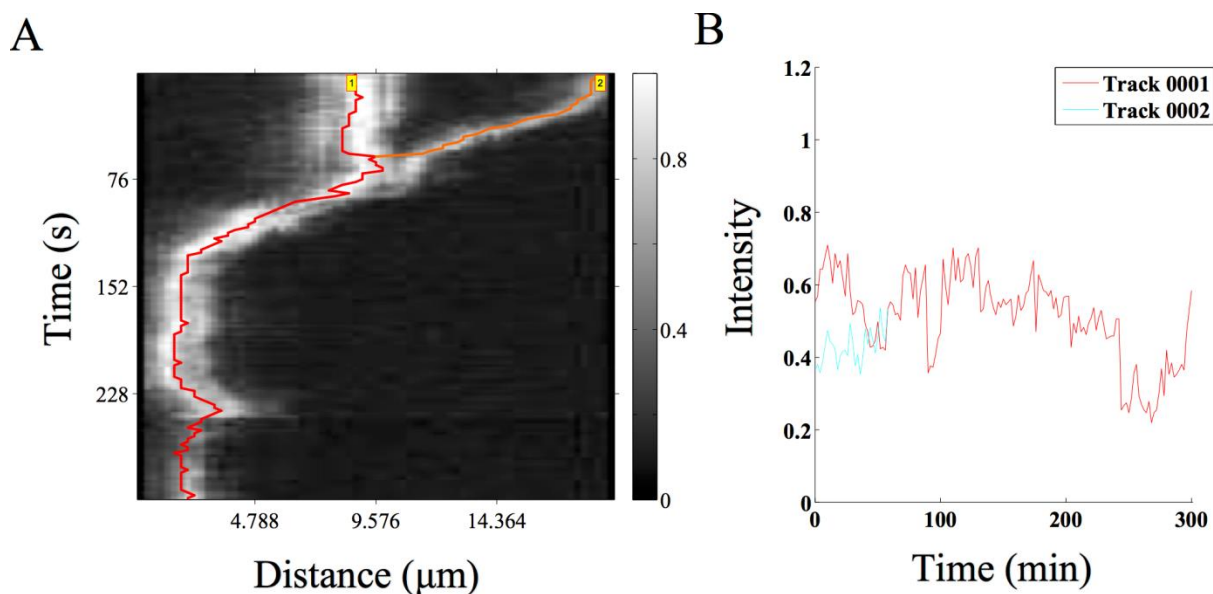


Figure 3.7. MT aster coalescence. (A) A time-series of MT asters undergoing fusion (time-series taken from previous work by Foster et al. (Foster et al., 2015)) was analysed using AMTraK. The grey scale bar indicates normalized fluorescence intensity of Alexa-647 labelled tubulin. (B) The relative intensity over time of the two coalescing asters is plotted.

While the coalescence appears not to result in a compaction of the aster, it demonstrates the utility of the code for 2D MT array transport. On the other hand, intensity measurements are expected to change during processes such as molecular ‘recruitment’ of subcellular structures, so we proceed to test the tool on this process, which had previously been studied using manual kymography.

3.4.5. Kinetics of clathrin assembly during *in vitro* vesicle formation

We proceed to quantify the assembly kinetics of clathrin on membranes from an *in vitro* reconstitution assay of clathrin assembly on vesicle precursors reported previously by Holkar et al. (Holkar et al., 2015). This process has been analyzed using kymography due to its effectively 1D spatial extent and the multiple simultaneous events of assembly. The published time-series of fluorescently labeled clathrin assembly kinetics in the presence of wild-type epsin (supplementary movie 3 in (Holkar et al., 2015)) and L6W mutant epsin (supplementary movie 5 in (Holkar et al., 2015)) in the form of 16 bit TIF images were provided by the authors (Sachin Holkar, personal communication). AMTraK was used to analyse this data without any pre-processing, resulting in tracked kymographs of assembly kinetics with wild-type (Figure 3.8A) and mutant epsin (Figure 3.8B).

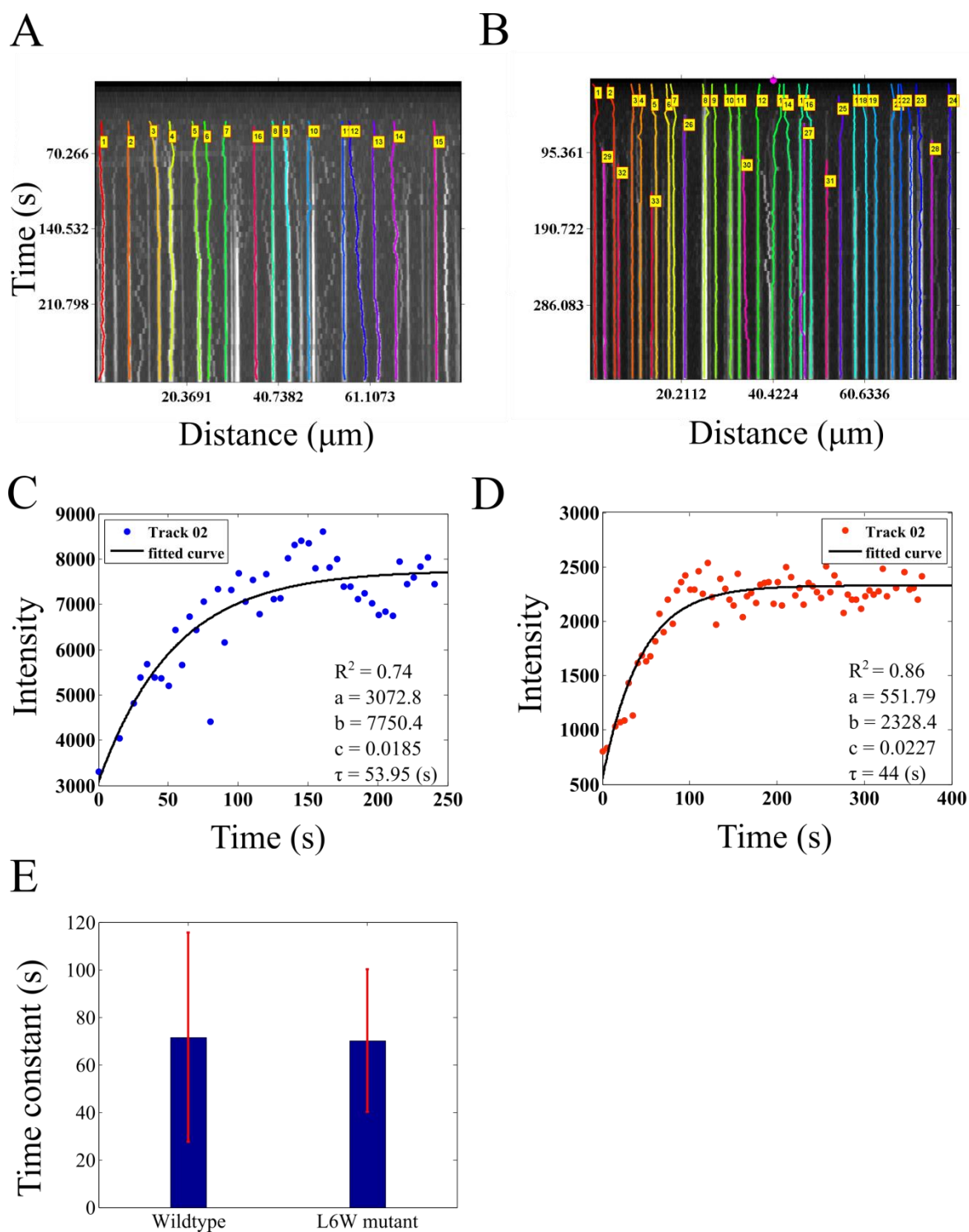


Figure 3.8. Dynamics of clathrin assembly. (A, B) Microscopy time-series taken from Holkar et al. (Holkar et al., 2015) of fluorescently labeled clathrin assembly in the presence of (A) wild-type and (B) mutant epsin were analyzed using AMTraK. Colored lines in the kymographs indicate detected tracks. (C, D) The change in intensity as a function of time based on AMTraK detected tracks from (C) clathrin + w.t. epsin and (D) compared to clathrin + (L6W) mutant epsin. The intensity kinetics plots are fit to a single-phase exponential function, $y = a + (b - a) \times (1 - e^{-ct})$ to obtain the time constant of assembly $\tau = 1/c$ (red). R^2 : goodness of fit. (E) The mean values (error bar represents SD)

of the time constant of assembly of clathrin (τ) in the presence of wild-type and mutant epsin are compared.

The software outputs a text-file of grey-value intensities normalized by the bit-depth (maximum normalized, between 0-1) (Table 3.1), which when multiplied by the bit-depth of the input images, produced intensity profiles of clathrin assembly in grey-values with time in the presence of wild-type (Figure 3.8C) and mutant epsin (Figure 3.8D). These intensity profiles were fit to a single phase exponential function $y = a + (b - a) \times (1 - e^{-ct})$, where y is the intensity which increases with time t , and depends on three fit parameters, a , b and c , the same function as used by Holkar et al. (Holkar et al., 2015). A large proportion of the assembly events were successfully tracked and most showed saturation kinetics that were fit by curves with $R^2 > 0.7$. While the parameters a and b are scaling factors, c determines the characteristic clathrin polymerization time, $\tau = 1/c$. In our analysis the clathrin assembly time in presence of wild-type epsin is $\langle \tau \rangle = 71.49 \pm 44.09$ s while with mutant epsin $\langle \tau \rangle = 70.16 \pm 29.89$ s. In our estimate of the mutant assembly time is indistinguishable from wild-type, consistent with the previous report, which used manual quantification of the kymograph (Holkar et al., 2015). We proceed to examine if our tool, which appears to work successfully on *in vitro* data with low background noise, can also be used for the quantification of *in vivo* dynamics inside the crowded environment of an intact cell.

3.4.6. Axonal vesicle transport: Characterizing directional switching

Synaptic vesicles in *Caenorhabditis elegans* mechanoreceptor neurons labeled with GFP-Rab3 have been recently studied by Mondal et al. in a whole-animal microfluidics device, providing retrograde and anterograde vesicle transport statistics (Mondal et al., 2011). Such *in vivo* data is complex, involves multiple crossovers and has many objects close to each other. AMTraK based analysis of the published data could detect up to 17 different tracks (Figure 3.9A). Vesicles that were not detected have typically low intensity or were out of focus and were not segmented. The spread of the distribution of instantaneous velocities (left-ward: negative, anterograde; right-ward: positive, retrograde, non-motile: paused) shows that the GFP-Rab3 vesicles are equally likely to be anterograde and retrograde in their transport (Figure 3.9B).

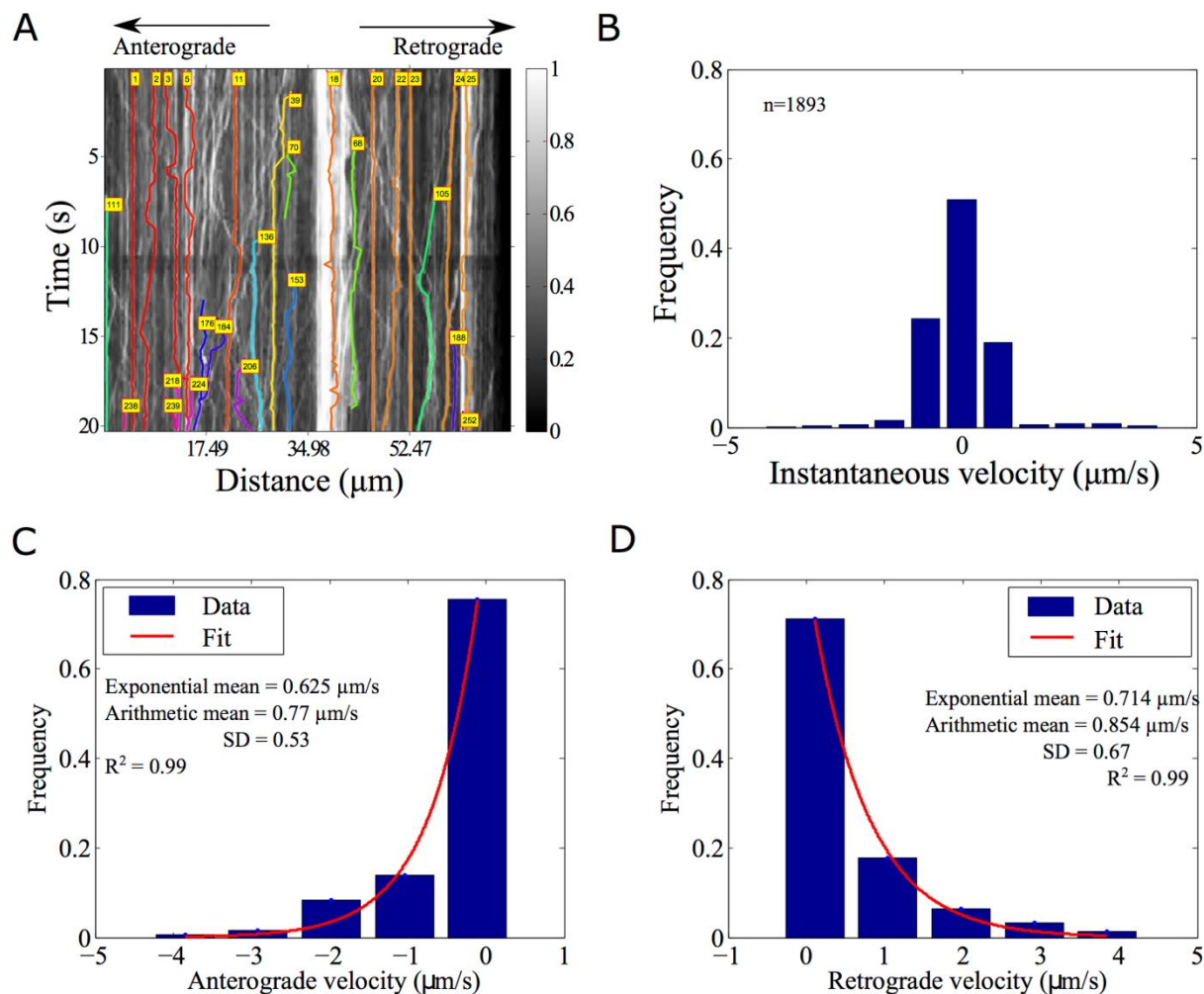


Figure 3.9. Analysis of synaptic vesicle transport. **(A)** GFP-Rab3 tagged vesicles from posterior touch cell neurons in *C. elegans* (experimental data from taken from supporting movie S1 from (Mondal et al., 2011)) were analyzed using AMTraK. Colored lines with index numbers indicate tracks. **(B)** The frequency distribution of instantaneous velocities of the vesicles (n=1592) is plotted using AMTraK (mean: 0.49 μm/s, SD 0.88). **(C, D)** The frequency distributions of non-zero velocities are fit with an exponential decay function $y = A \cdot e^{-x/m}$ (red line), where A: scaling factor and m: mean. **(C)** The mean anterograde velocity from the fit is 0.625 μm/s with arithmetic mean 0.77 ± 0.53 μm/s (n = 425) and **(D)** the mean retrograde velocity from the fit is 0.714 μm/s with arithmetic mean 0.854 ± 0.67 μm/s (n = 540). Arithmetic means are reported \pm standard deviation (SD). R² indicates the goodness of the fit.

Based on the shape of the frequency distribution of the non-zero velocities in anterograde (Figure 3.9C) and retrograde (Figure 3.9D) directions, an exponential decay fit to the frequency distribution was used to estimate mean velocities (goodness of fit, R² = 0.99). To enable comparison with the arithmetic means reported in literature (Mondal et al., 2011), we also estimate the average. The mean velocity from the exponential fits of anterograde transport is 0.625 μm/s (n = 425, arithmetic mean \pm SD: 0.77 ± 0.53 μm/s) while the mean

retrograde velocity is $0.714 \mu\text{m/s}$ ($n = 540$, arithmetic mean \pm SD: $0.854 \pm 0.67 \mu\text{m/s}$). In this case, both means are comparable since only non-zero values were analyzed. Velocities in both directions are of comparable order of magnitude to the published values obtained by manual detection (Mondal et al., 2011), but ~ 1.5 -fold lower, due to a (non-zero) threshold velocity used by the authors to define pauses (as personally communicated by the author, Sudip Mondal). This difference in values could also be attributed to the choice of tracks considered for manual and automated analysis. Thus, AMTraK can be reliably used to quantify transport and assembly dynamics from both *in vitro* and *in vivo* fluorescence microscopy data, as seen from the quantification, which is consistent with literature.

3.5. Discussion

In this report, we have described a novel tool for automatic quantification of kymographs from fluorescence microscopy time-series. Using simulations we have demonstrated sub-pixel position detection accuracy of our proposed method, in conditions of low Poisson and Gaussian noise. The program quantifies position, motility, brightness intensity of fluorescence signal and fusion/splitting events. The utility of the code is tested on *in vitro* and *in vivo* fluorescence time-series ranging from *in vitro* assays of MT gliding assays with kinesin, coalescence dynamics of MT-asters, clathrin assembly kinetics on lipid tethers to *in vivo* axonal synaptic vesicle transport. The measures of average transport and kinetics of these diverse data types are consistent with published data and provide opportunities for improved statistics of individual events from a dynamic time-series, which were not as easily accessible with current methods.

Manual quantification of kymographs (Rietdorf and Seitz, 2008) depends typically on reliable edge detection. As a result, quantification varies between individuals and requires prior information or experience (Welzel et al., 2009). Yet, manual kymography is widely reported in cell-biological literature for the analysis of dynamic processes, possibly due to the heterogeneity of the data types and the absence of a single standard method or even criterion, which to make the process less interactive. While developing AMTraK, we tested global (whole-image) methods of edge-segmentation (contour-, watershed- and gradient-based), but found them to be inadequate for the task. Possible reasons include the time-dependent brightness and contrast changes of the sample resulting from either bleaching or intrinsic dynamics. We find that for some applications such as vesicle transport and protein recruitment, the detecting and tracking peaks is ideal, while for microtubule gliding assays edge detection is better. As a result our code allows the user to choose amongst three

different methods of segmentation based on the nature of their data (a) peak detection by *findpeaks* and (b) watershed and (c) edge detection using the Canny edge detector.

Typical problems in peak or edge detection arise when the data has poor signal to noise. This is also seen in our error analysis with increasing noise amplitude (Figure 3.3D). One solution is to background-subtract the image, which can be easily done in multiple tools. The occasional loss of some particles in a time-series such as synaptic vesicles (Figure 3.9A), despite being visible to the eye, results from a failure in detection or a 'pruning' step used to remove spurious and redundant tracks. Such pruning however was found to be necessary to ensure robustness of the code for handling multiple data types and is simple to troubleshoot due to the limited number of adjustable parameters. While intensity matching did not improve the percentage vesicles tracked, in future additional features like those used in pattern-matching for tracking (Miura, 2005) could be used further improve the detection percentages. Our test with increasing (Poisson and Gaussian) random image noise (Figure 3.3) also suggests that increase of fluorescently tagged proteins (for instance due to expression level increases *in vivo*) could result in reduced spatial contrast. Such data would then be difficult to automatically quantify using AMTraK. The data would require pre-processing with something similar to an anisotropic diffusion filter (Perona and Malik, 1990) to preserve edge information but reduce non-specific signal. In future, multiple data pre-processing routines could be implemented in a separate module, to add to the functionality of the program.

Our quantification of the frequency distribution of synaptic vesicle transport in anterograde and retrograde directions (Figure 3.9C, D) suggests the instantaneous velocities are exponentially distributed. While the arithmetic mean suffices for comparison with experimental reports (Mondal et al., 2011), the quantification of the precise nature of the distribution of velocities could be used as a test of theoretical models. Such a comparison has been made in previous work on synaptic vesicle precursor trafficking (Maeder et al., 2014). Such models are relevant for both neurophysiology as well as understanding of collective effects in molecular-motor driven vesicle transport *in vivo* (Bridgman, 1999; Hendricks et al., 2010).

The collective motor velocity of human kinesin driven gliding of MTs has been well characterized in previous work (Howard, 2001; Gibbons et al., 2001; Howard et al., 1989). Many of these studies have shown that the MT length and kinesin density do not affect the mean speed. However, the time-series of individual filaments show small time-dependent variations (Figure 3.6A, B), possibly a result of the local inhomogeneity of motor distributions. This information could be of some use when mixed-motor populations are used

(Ikuta et al., 2014). Recent studies of filament motility have used a filament-tracking approach based on a MATLAB program FIESTA (Ruhnow et al., 2011), with a positional accuracy of 30 nm. We find the distribution of time-averaged velocity of gliding calculated using AMTraK match closely the distribution obtained from analysis using FIESTA (Figure 3.10). This suggests that while complex transport dynamics in 2D are indeed better analyzed using tracking tools, for those data sets that are amenable to kymography analysis, AMTraK results are comparable to those obtained from tracking tools with sub-pixel accuracy.

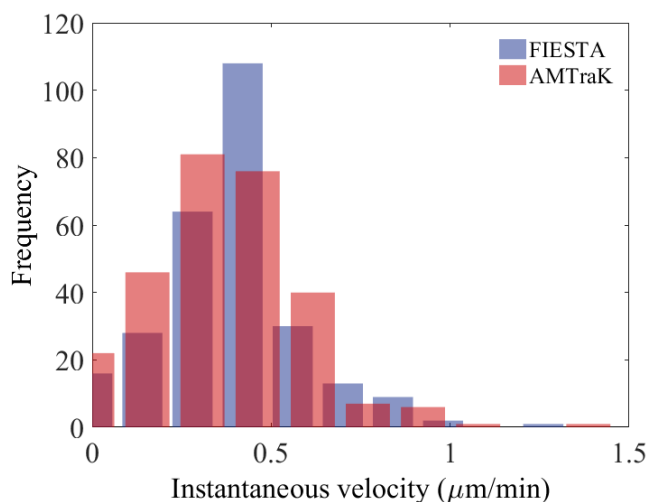


Figure 3.10. Comparing kymography to filament tracking. The frequency distribution of instantaneous velocities obtained after analyzing time-series of MTs gliding on kinesin using AMTraK (red bars) and the high-precision filament-tracking tool, FIESTA (blue bars) are plotted.

While the dynamics of multiple particles can be simultaneously quantified using AMTraK, the selection of LOIs remains manual. However, once an LOI has been selected, the program can also be used in the ‘From file’ mode to apply a pre-existing LOI to quantify kymographs in other channels (e.g.: bright field, fluorescence) and other fields of view with similar sample geometries. Potentially, LOIs could be generated independent of AMTraK too, provided they are compatible with the input format. Multiple bright-field and fluorescence correlative analysis tools for bacterial image analysis (Athale and Chaudhari, 2011a; Sliusarenko et al., 2011; Guberman et al., 2008; Ducret et al., 2016) are examples in this case. More recent developments in image-analysis software to systematically extract data from microfluidics experiments automatically output channel information (Sachs et al., 2016), which could also form the basis for the LOIs for multiple fields of view. These approaches could in future further increase the throughput our analysis tool.

Multiple software tools for kymography have been described in the recent past in literature and their features are summarized for comparison (Table 3.2, Figure 3.11). While most tools including this one, require user inputs for the process of kymograph generation, only AMTraK and Kymograph Direct (Mangeol et al., 2016) automates the detection and connection. However, certain features of AMTraK make it unique, being absent in other comparable tools, such as automated branch-point detection, an integrated quantification module and sub-pixel positional accuracy accessible with an easy to use GUI front-end. In addition, since the code is open source and written in MATLAB, it is more likely to be used in an existing microscopy analysis workflow, due to the increasing spread of MATLAB as a data analysis platform in quantitative cell-biology research (Shekhar et al., 2014; Howard, 2014).

Table 3.2. A comparison of features in kymography tools described in literature and commonly in use for cellular and subcellular scale images.

Feature / Tool	AM Tra K	Multi-kymograph	Makekymograph	Icy-Kymo graph Tracker	Kymo maker	Points from Kymo graph	Kymo graph mt2	KymographClear and KymographDirect
LOI selection	Manual	Manual	Semi-automated	Manual	Manual	No	Manual	Manual
Multiple LOIs	Yes	Yes	Yes	Yes	Yes	No	No	No
Automated track detection	Yes	No	No	Semi-automated	Yes	Semi-automated	No	Yes
Quantification	Yes	Separate	No	Separate	No	XY-coordinates	No	Separate
No. of adjustable parameters	8	1	1	7	13	-	-	-
Split and merge detection	Automatic	No	No	No	No	No	No	Manual
Open source	Yes	Yes	Yes	Yes	No	Yes	Yes	Yes
Programming language	MATLAB	ImageJ macro	Java (ImageJ plugin)	Plugin for Icy	-	Java (ImageJ plugin)	Java (ImageJ plugin)	ImageJ macro and LabView
Reference	This report	(Rietdorf, Jens (FMI	(Hallman, 2007)	(Chenuard et al.,	(Chiba et al., 2014)	(Das et al., 2012)	(Siebrasse et al., 2012)	(Mangeol et al., 2016)

		and Seitz, 2008)		2010)				
--	--	------------------	--	-------	--	--	--	--

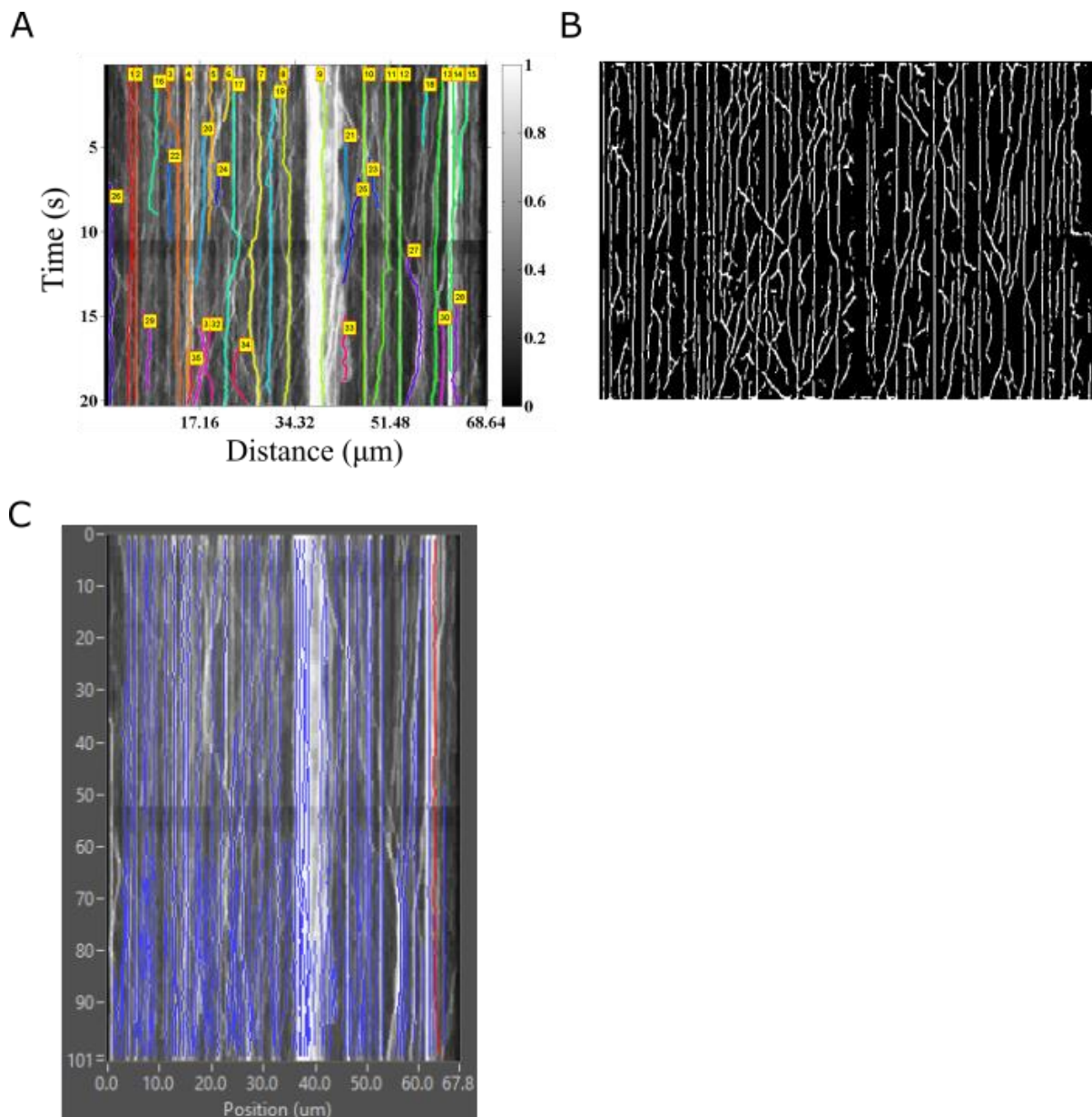


Figure 3.11. Automated track detection by other tools. Kymograph of axonal vesicle transport tracked by (A) AMTraK, (B) Kymomaker and (C) KymographDirect are shown.

Thus, AMTraK could serve as a tool for the rapid quantification of image time-series of transport and assembly kinetics from microscopy. This has become particularly relevant in the context of high-content screening (Zanella et al., 2010), where the spatial interaction patterns are becoming just as important as bulk kinetics measured in traditional high throughput screens.

3.6. Conclusion

We have developed AMTraK, an automated tool for the quantification of kymographs. Our approach detects peak and edge information and utilizes a distance minimization approach to link them. We demonstrate the wide utility of our tool by quantifying microtubule transport dynamics, clathrin polymerization kinetics and vesicle transport. Combined with a user-friendly interface, objective detection criteria and open source code, we believe AMTraK can be used to extract more and reproducible statistics from microscopy of subcellular dynamics.

Chapter 4

FluoreT: A platform for 2D fluorescence tracking with sub-pixel accuracy

Overview

In Chapter 3, we have described automated kymography as a powerful technique to analyse spatiotemporal dynamics of various seemingly 1D processes in cell biology. To study the biophysical aspects of intracellular processes, it is useful to track morphology, motion and interaction of particles in multiple dimensions from time-lapse image data. In this chapter, I describe Fluorescence Tracker (FluoreT), an automated particle tracker in 2D, which performs intensity-based segmentation and nearest-neighbour based linking to track labelled particles and quantify parameters of their motility and length. The tool is integrated in an intuitive interface and provides an objective method for reproducible analysis of fluorescence microscopy time-series of subcellular dynamics.

4.1. Introduction

Time-lapse imaging is pivotal in understanding and observing the spatiotemporal dynamics of subcellular events that lay the foundation for higher order cellular processes such as determination of cell shape, locomotion, cell division, cell-cell adhesion and differentiation. Over the last two decades, the advent of a plethora of compatible fluorophores, high resolution microscopy and robust computer programs for quantitative analysis of data has popularized the use of fluorescence microscopy for *in vitro* as well as *in vivo* imaging. While kymography proves to be a powerful method to qualitatively and quantitatively analyse fluorescence image-series, its scope seldom extends beyond classic 1D problems in biology (described in Chapter 3). For biophysical studies of intracellular processes, it is useful to track single particle morphology, motion and interaction in multiple dimensions from image data. The ‘particles’ in focus here could range from single molecules, clusters, cytoskeletal filaments, organelles to cells themselves. To this end, several algorithms for single particle tracking have been proposed for the efficient and objective quantification of motion of labelled biomolecules (Chenouard et al., 2014; Cheezum et al., 2001; Maska et al., 2014; Ulman et al., 2017; Jaqaman et al., 2008).

The process of microtubule transport by molecular motors reconstituted *in vitro*, referred to as a ‘gliding assay’ has been extensively used to examine the fundamental nature of multi-molecular transport of actin and microtubule filaments by motors (Howard et al., 1989; Nitzsche et al., 2010; Leduc et al., 2007; Toyoshima et al., 1987). Recent studies have also used gliding assays to address microtubule mechanics based on the bending of filaments while undergoing transport (Martin, 2013). Multiple studies have used a filament tracking programme called FIESTA, that is reported to have ~9 nm accuracy of filament detection (Ruhnow et al., 2011) for quantifying transport of microtubules in gliding assays (Lüdecke et al., 2018; Grover et al., 2016; Jain et al., 2019). However, the tool displays some limitations. At high filament densities, it is found to not resolve filament crossovers accurately. It is seen to switch the plus-minus ends of MTs in data of high temporal resolution. We also find that it may underestimate the number of small filaments in the field of view. Hence, a custom-made tool that alleviates these problems could be of utility.

In this chapter, we describe Fluorescence Tracker (FluoreT), an automated particle tracking software that performs centre-of-mass-based segmentation and distance-based linking to quantify object motion and length in 2D. We demonstrate the sub-pixel accuracy of the tool using simulated noisy images. We test the utility of FluoreT on experimental *in vitro* reconstitution data from kinesin-driven microtubule gliding assays and assess its performance in comparison to FIESTA.

4.2. Materials and Methods

4.2.1. Microscopy and image pre-processing

The microtubule gliding assay experiment (courtesy, Kunalika Jain) is briefly described in (Chaphalkar et al., 2016) and in Chapter 3. The images were de-noised using a 3 x 3 median filter in ImageJ.

4.2.2. Simulated test images

Beads

Simulated images of static beads were generated as described in Chapter 2, Materials and Methods. To simulate a time-series of diffusive bead motion, a simple 2D random-walk was implemented. Each bead was displaced in random orientations in the consecutive frames. The step-size of the bead was drawn from root mean square displacement values calculated based on the following equation:

$$\langle r^2 \rangle = 4Dt \quad (\text{Equation 4.1})$$

Here, r^2 is the mean square displacement, D is the fixed diffusion coefficient assigned to the beads and t is the time-step.

To simulate a time-series of ballistic motion of beads, the initial position of beads (x_0, y_0) was incremented in each frame using the following equations:

$$x_t = x_0 + vt * \cos(\theta) \quad (\text{Equation 4.2})$$

$$y_t = y_0 + vt * \sin(\theta) \quad (\text{Equation 4.3})$$

Here, v is the specific fixed speed assigned to the beads and (x_t, y_t) are position coordinates of beads after time t .

Filaments

Filaments ($n = 10$) were simulated in 8-bit images as randomly oriented, bright, rigid rods (intensity = 255) of variable lengths (10 to 90 pixels) on a black background (intensity = 0) using MATLAB (Mathworks Inc., USA). To resemble the convolution effect of microscopy, the images were further filtered using a 5 x 5 disk filter and smoothed using a 3 x 3 averaging filter. These images were processed further in Fiji, where their contrast was enhanced by normalization and they were smoothed using a 3 x 3 filter. A representative filament is shown in Figure 4.5C, whose intensity profile along the width is shown in Figure 4.1.

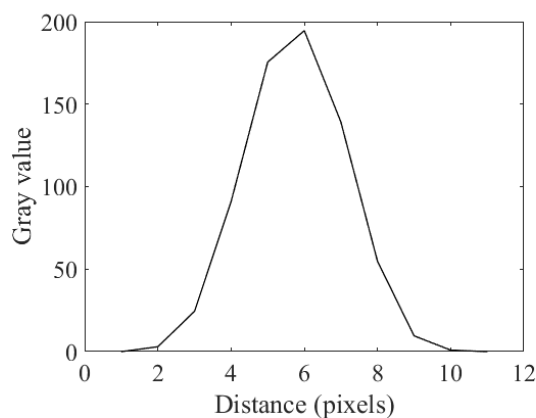


Figure 4.1. Intensity profile along the width of a simulated filament.

4.2.3. FluoreT implementation specifics

The FluoreT code was implemented in MATLAB R2014b (MathWorks Inc., USA) in combination with the Image Processing (version 7.0) and Statistics (version 7.3) toolboxes and was tested on Linux, Mac OSX and Windows 10 platforms.

4.3. Algorithm and Workflow

The Fluorescence Tracker (FluoreT) is a program for 2D single particle tracking in fluorescence microscopy images. It involves intensity-based particle detection and distance minimization based linking to quantify dynamics of particle motion in image time-series. The program has a GUI front-end and is accompanied by a detailed user-guide. The algorithmic workflow (Figure 4.2) is divided broadly into two steps:

- (a) Particle detection and tracking
- (b) Statistics

These steps in the workflow are reflected in the graphical user interface layout (Figure 4.3).

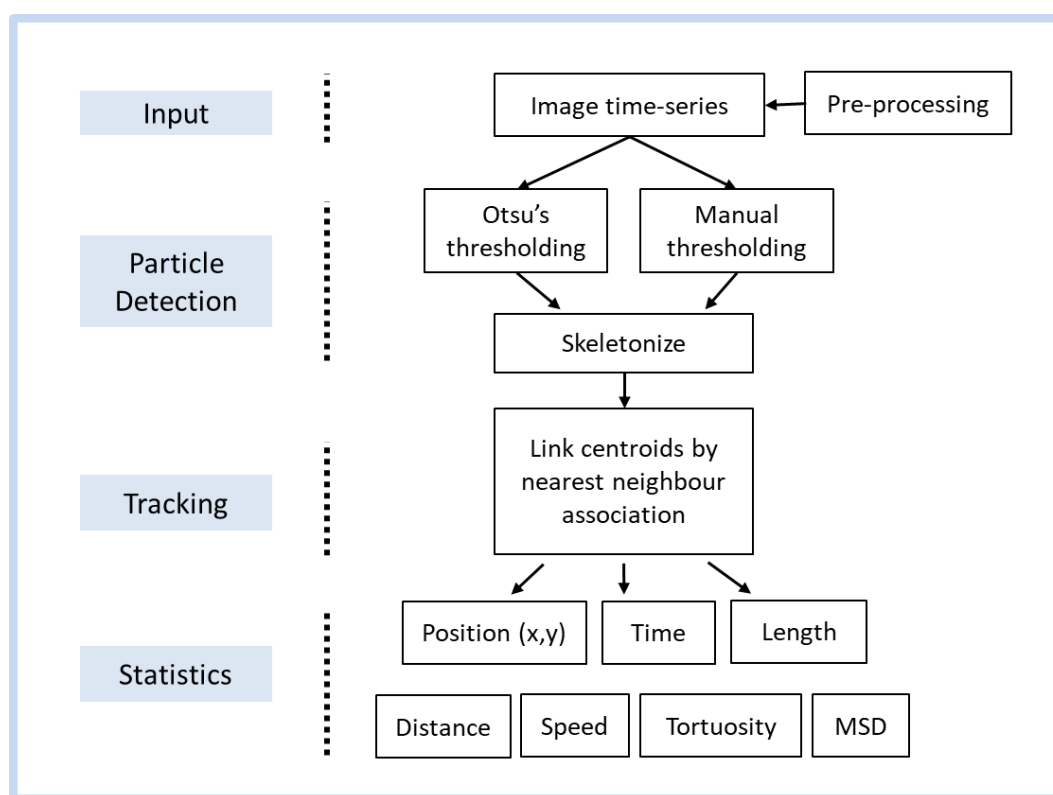


Figure 4.2. Algorithm. The algorithm involves two steps (1) particle detection and tracking and (3) quantification to obtain statistics from the input data.

The functioning of each of these steps is briefly described as follows:

(a) Particle detection and tracking:

The user chooses an input image time-series with the ‘Open File’ button. Image time-series are assumed to be uncompressed, 8 or 16-bit multi-page TIF files. The user can choose to process either the whole or a subset of frames using the ‘Frame nos.’ text box. For example entering ‘2:2:8’ will now result in only frames 2, 4, 6 and 8 being processed for further

analysis. The output will be stored in a subfolder named ‘fluoret-*<name of input file>*’ in the same directory as the image. In the segmentation step, particles of interest are distinguished from the background based on an intensity threshold. Choosing the ‘Automated’ option results in global thresholding of each image in the time-series by Otsu’s method (See Chapter 2, Section 2.5). Alternatively, one may choose to input a ‘Manual threshold’ value of intensity, a fraction in the range 0-1. Particle detection is commenced on the click of the ‘Locate particles’ button, the first output of which is a segmentation-preview window displaying the skeleton of the particle overlaid in red on the first time-frame of the original image-series. Depending on the segmentation accuracy observed in this window, the user may want to tweak the threshold value applied and restart the segmentation process. The skeleton and centroid information obtained from segmentation is used for measuring the length and for tracking the motion of particles.

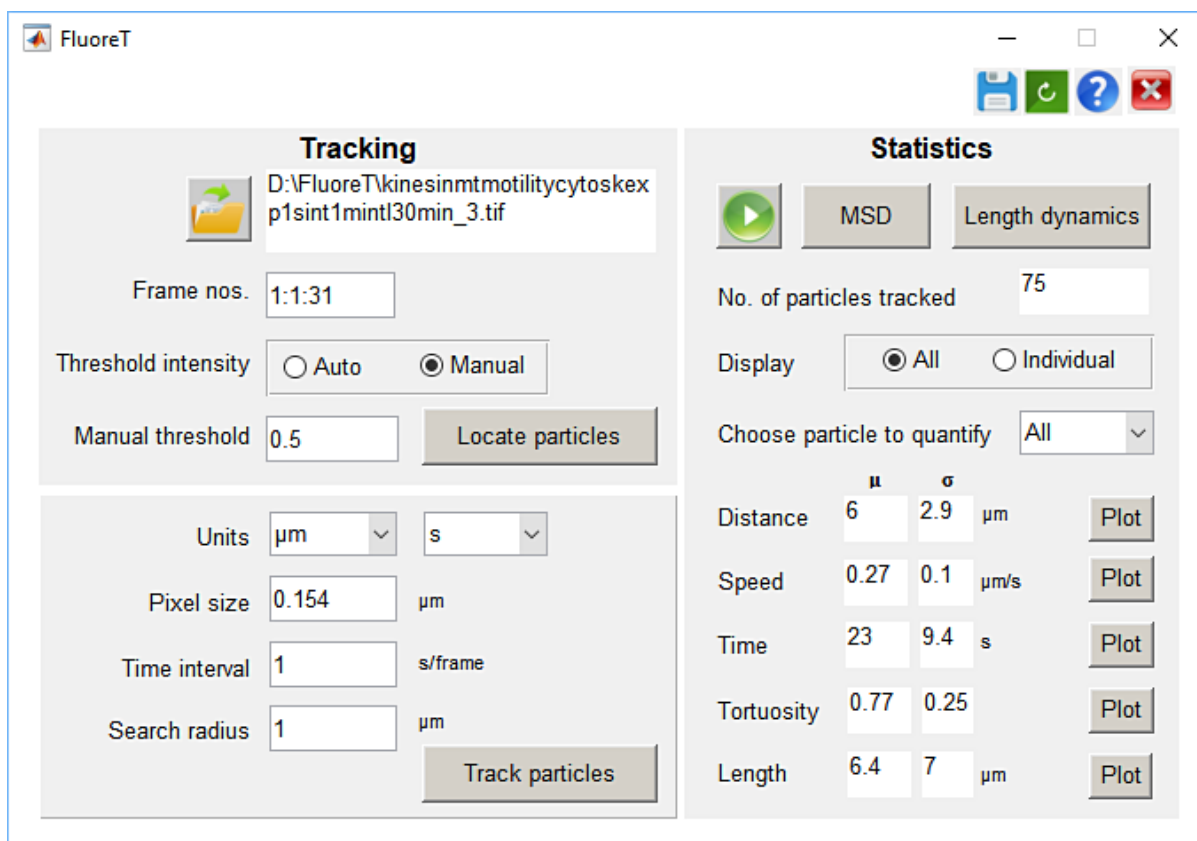


Figure 4.3. FluoreT interface. The GUI allows the user to provide input for segmentation and tracking in the ‘Tracking’ panel, while quantification is carried out in the ‘Statistics’ panel.

Once particles are detected, the user needs to fill in parameters of tracking. The drop-down menu ‘Units’ allows the user to select distance and time units, and the text boxes ‘Pixel size’ and ‘Time interval’ are used to provide conversion factors per pixel and per frame

respectively. This results in scaling the pixels and frame numbers to physical units. The list of centroids $P(t)$ for each time frame t is linked resulting in trajectories, based on user input parameters of ‘Search radius’ (λ_1). The core tracking function is adapted from (Athale et al., 2014). Centroids (see Chapter 2) are linked if the pair-wise distance $d_j(t, t+\tau)$ between every j^{th} centroid in successive frames ($t, t+\tau$) satisfies the condition $(d_j(t, t+\tau)) \leq \lambda_1$ iteratively for the j^{th} centroid in every subsequent time frame ($t + \tau$). The centroids that do not form a part of any trajectory are treated as start-points of new trajectories. Any trajectory with less than 3 data-points $len(P) \leq 3$ is eliminated from further analysis to avoid artifacts due to very short paths.

The code produces both, text-file outputs and plots of the dynamics estimated from the tracking. The end of tracking is marked by the display of a plot of trajectories (blue) overlaid on the first image of the original time-series. Parameters used for particle detection and tracking are stored in a text file on using the ‘Save Parameters’ button.

(b) Statistics:

The ‘number of particles detected’ are displayed in the panel as soon as basic quantification is completed. The ‘Make and save movie’ button produces and saves the output of tracking as a multi-page TIF file in the same subfolder. The user may want to tweak the tracking ‘search radius’ and re-run the tracking if spurious trajectories are observed at this stage. Mean square displacement analysis (see Chapter 2) of all detected trajectories is performed on pressing the ‘MSD’ button. A window with the plot of average MSD against increasing time-step is displayed. Ticking the ‘Fit MSD’ option *a priori* helps the user to extract the value of the average two-dimensional diffusion coefficient by fitting the entire or a fraction of the average MSD curve to the anomalous diffusion model (Equation 2.5, Chapter 2). Time-dependent dynamics of length of skeletons of detected particles can be visualized by clicking the ‘Length dynamics’ button.

A flexible display allows the user to choose between average statistics of ‘All’ trajectories or a specific ‘Individual’ trajectory picked from the drop-down menu. The mean (μ) and standard deviation (σ) of these variables are generated in the text boxes. Additionally, frequency distributions of Distance, Time, Speed and Tortuosity (i.e. directionality) and Length are plotted if the button ‘Plot’ corresponding to these variables is pressed.

Outputs of the analysis are stored in multiple tab-delimited text files to enable reproducible analysis and are summarized in Table 3.1.

Table 3.1. Description of output files generated by FluoreT.

Function	Sr. No.	Output file	Description
Locate particles	1	segmentation.tif	Image of detected particles with skeletons overlaid in red.
Track particles	2	trajectories.txt	(x,y) Coordinates and lengths of tracked particles
Make movie	3	trackingmovie.tif	TIF movie of tracked particles where the current position is marked in blue, trajectory in red and particle ID is displayed in yellow
	4	trajectoryplot.tif	Trajectories (blue) overlaid on the first image
	5	InstStats.txt	Instantaneous (stepwise) statistics of each trajectory
	6	StatsPerTrack.txt	Averaged statistics of each trajectory
MSD	7	MSD_vs_Time.tif	Mean square displacement profiles
	8	AvgMSD_vs_Time.tif	Average MSD curve with fit
	9	ID_Time_MSD.txt	Track-wise MSD
Length dynamics	10	Length_vs_Time.tif	Time-dependent statistics of length of skeletons of tracked particles
	11	elongrate.txt	Elongation rates of particles
Save Parameters	12	Parameters.txt	Record of parameters of particle segmentation and tracking

4.4. Results

4.4.1. Accuracy of position detection

To test the accuracy of position detection of the algorithm, we created simulated images of randomly localized, circular objects that represent typical fluorescence images of objects (Figure 4.3A) comparable to subcellular structures in pixels (Chapter 2, Figure 2.1A). Complex noise was added to the image as described in Chapter 2.

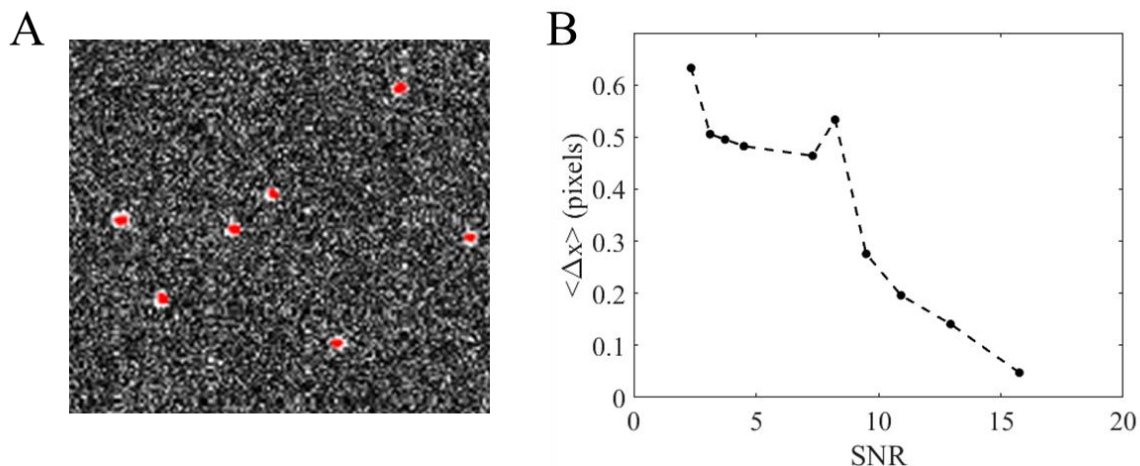


Figure 4.4. Sub-pixel accuracy of position detection. (A) A static image showing simulated beads on a noisy background. Centroids (red dots) of the beads were detected by FluoreT. (B) The mean error of detection in pixel units ($\langle \Delta x \rangle$) is plotted as a function of the signal to noise ratio (SNR).

The Euclidean distance between the position of the detected centroids (x_D , y_D) and the simulated position (x_S , y_S) is used as an estimate of the accuracy in position detection.

$$\Delta x = ((x_D - x_S)^2 + (y_D - y_S)^2)^{1/2} \quad (\text{Equation 4.1})$$

Increasing levels of noise were added to the time-series and the mean error in position detection was estimated. The SNR was calculated as described in Section 2.3. The mean error ($\langle \Delta x \rangle$) was found to be less than 1 pixel even at SNR below 4. During segmentation, optimal intensity thresholds for segmentation were chosen independently for each noise level, either automatically or manually. We find that in low SNR conditions, manually adjusted intensity thresholds improved segmentation as fewer false positives were observed with stringent manual thresholds.

4.4.2. Accuracy of length detection

In addition to particle position, FluoreT also measures particle length in an automated manner. In order to test the accuracy of the length estimation feature of FluoreT, we chose static images of 8 filaments of different lengths (Figure 4.5A) from an *in vitro* gliding assay in which microtubules were allowed to glide on immobilized kinesin motors. The lengths of these filaments were measured manually using ImageJ, independently by three individuals in the lab. The average length obtained from manual measurements (L_m) was treated as the ‘actual length’ of the filament. We then allowed FluoreT to automatically measure the length of these filaments and compared the output (L_a) with the ‘actual’ length. The error is taken as

the difference in manual and algorithmic measurements ($e = \langle L_m \rangle - L_a$). We find that the error in length detection is sub-micron and independent of filament length (Figure 4.5B).

FluoreT's length detection module was also validated with simulated data, since there is no 'actual' length in experiments. Simulations provide a 'true' value for comparison. We simulated static images of rigid, rod-like filaments that were processed to mimic the effect of convolution in fluorescence microscopy (Figure 4.5C). The filaments were of varying lengths (10 pixels to 90 pixels).

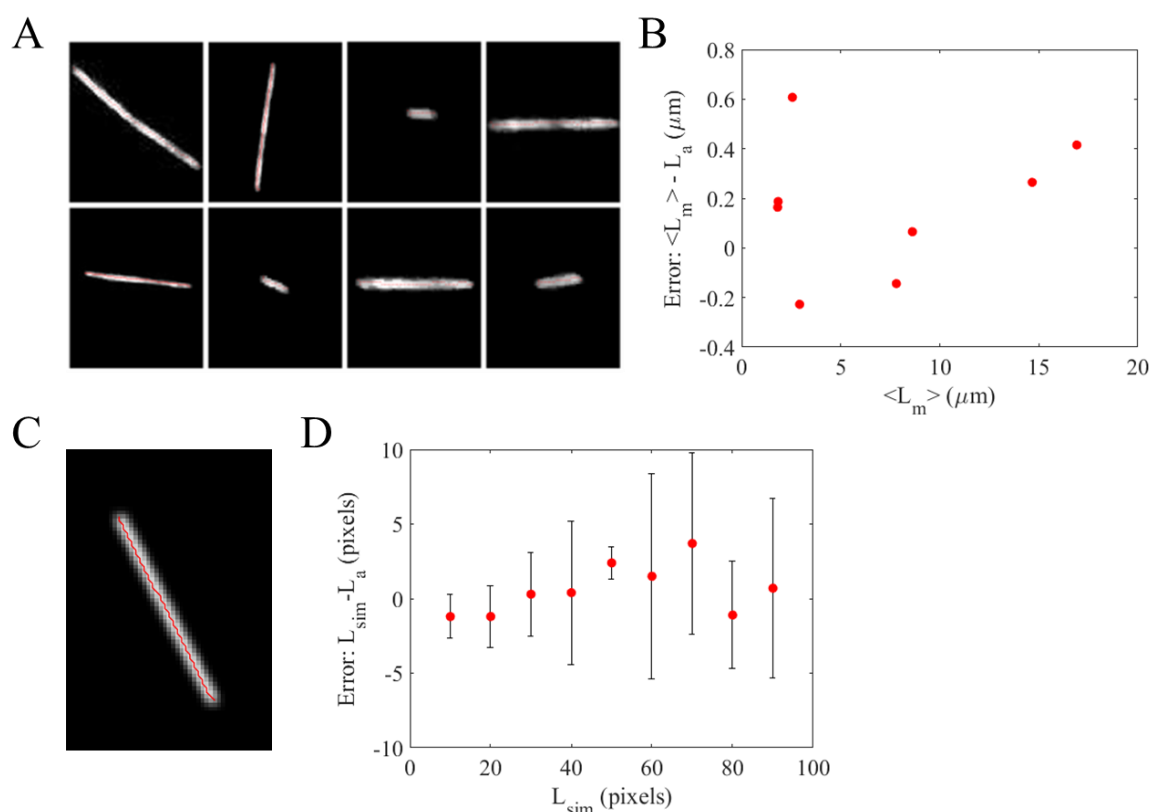


Figure 4.5. Accuracy of length detection. (A) Microscopically imaged microtubule filaments chosen for length measurement are shown. Their lengths were measured manually ($n_{\text{repeats}} = 3$) and using FluoreT. (B) The difference (error) in the average manual length (L_m) and algorithmically measured length (L_a) is plotted as a function of L_m . (C) The skeleton (red line) of a simulated filament detected by FluoreT is shown. (D) The difference in the simulated length (L_{sim}) and algorithmically measured length (L_a) is plotted as a function of L_{sim} . Number of filaments simulated for each length slot, $n = 10$.

In this case, the error in length detection was calculated as the difference between the simulated length (L_{sim}) and the length measured by the algorithm (L_a). The results from simulation are consistent with what was observed in experimental filaments as the error in length showed no dependence on length of filaments. Also, the average error is equally distributed around 0, indicating that FluoreT has overestimated as well as underestimated the

lengths of some simulated filaments, as opposed to consistent underestimation observed in experimental filaments.

4.4.3. Tracking diffusive and directional motion of simulated beads

After testing the position and length detection accuracy, we proceeded to further test the ability of FluoreT to track particles that perform two different kinds of movement over time. Time-series of circular particles were simulated that perform diffusive (Figure 4.6A) and transported (Figure 4.6B) particle motion.

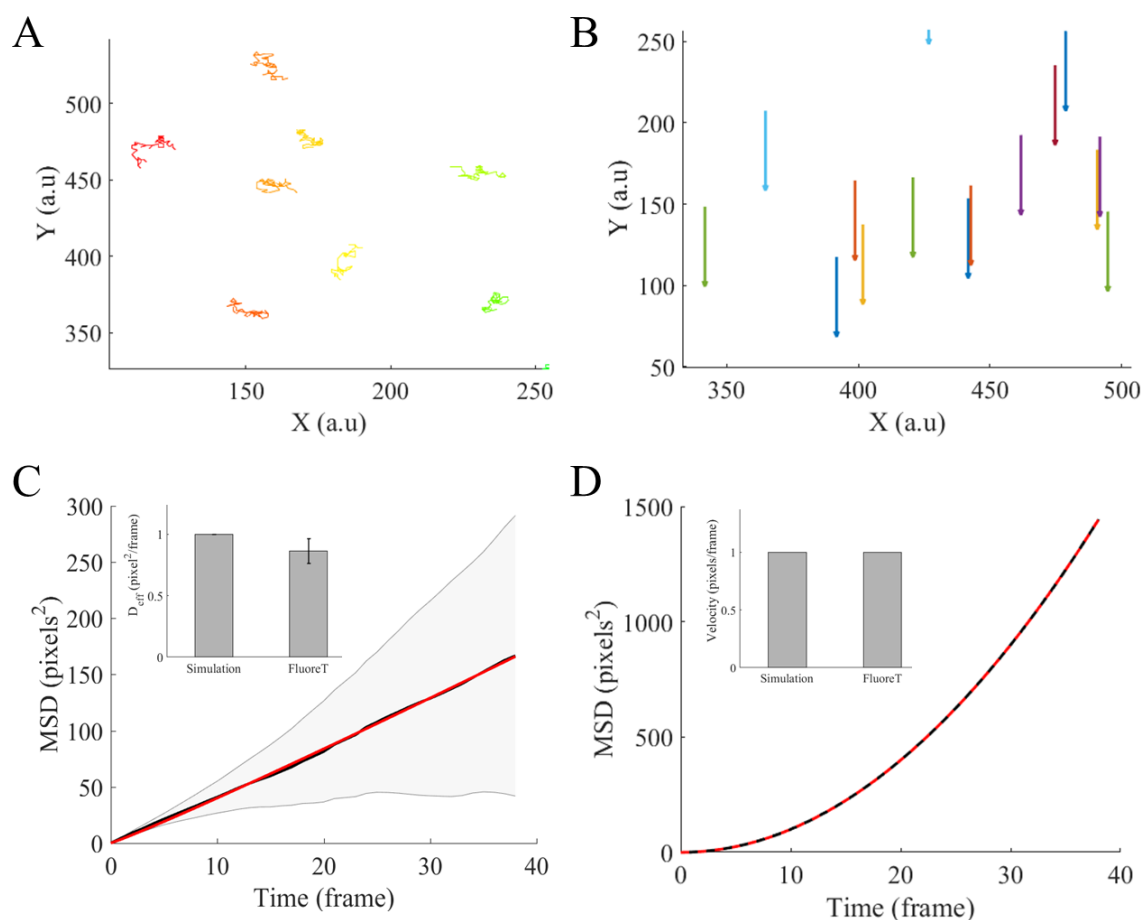


Figure 4.6. Diffusive and transported motion analysed by FluoreT. Trajectories of simulated beads showing (A) diffusive motion and (B) transported-like motion are shown. (C) Average MSD profile (black solid lines) of diffusive beads from (A) was fit (red) to the anomalous diffusion model to obtain the effective diffusion coefficient. Shaded gray region indicates standard deviation. *Inset:* The simulated diffusion coefficient and estimated diffusion coefficient were compared. (D) The average MSD profile (black solid line) of directional beads from (B) was fit (red dashed line) to the anomalous diffusion model. *Inset:* The simulated bead velocity was compared with the velocity measured by FluoreT.

We analysed the motility of these particles using FluoreT and compared motility parameters. The effective diffusion coefficient of randomly diffusing simulated particles was found to be comparable with the actual value of D_{eff} used in the simulation, i.e. 1 pixel²/frame. We found the measured velocity of directional particles to be identical with the value used for simulation, i.e. 1 pixel/frame.

4.4.4. Motility and length of motor-driven microtubules

Having validated the ability of FluoreT to characterize diffusive and transported-like motion of simulated particles, the tool was tested on experimental data that comes from an *in vitro* gliding assay experiment. Kinesin motors are immobilized on the surface and TRITC-labelled, taxol-stabilized microtubules of varying lengths (Figure 4.7A) are allowed to glide on them.

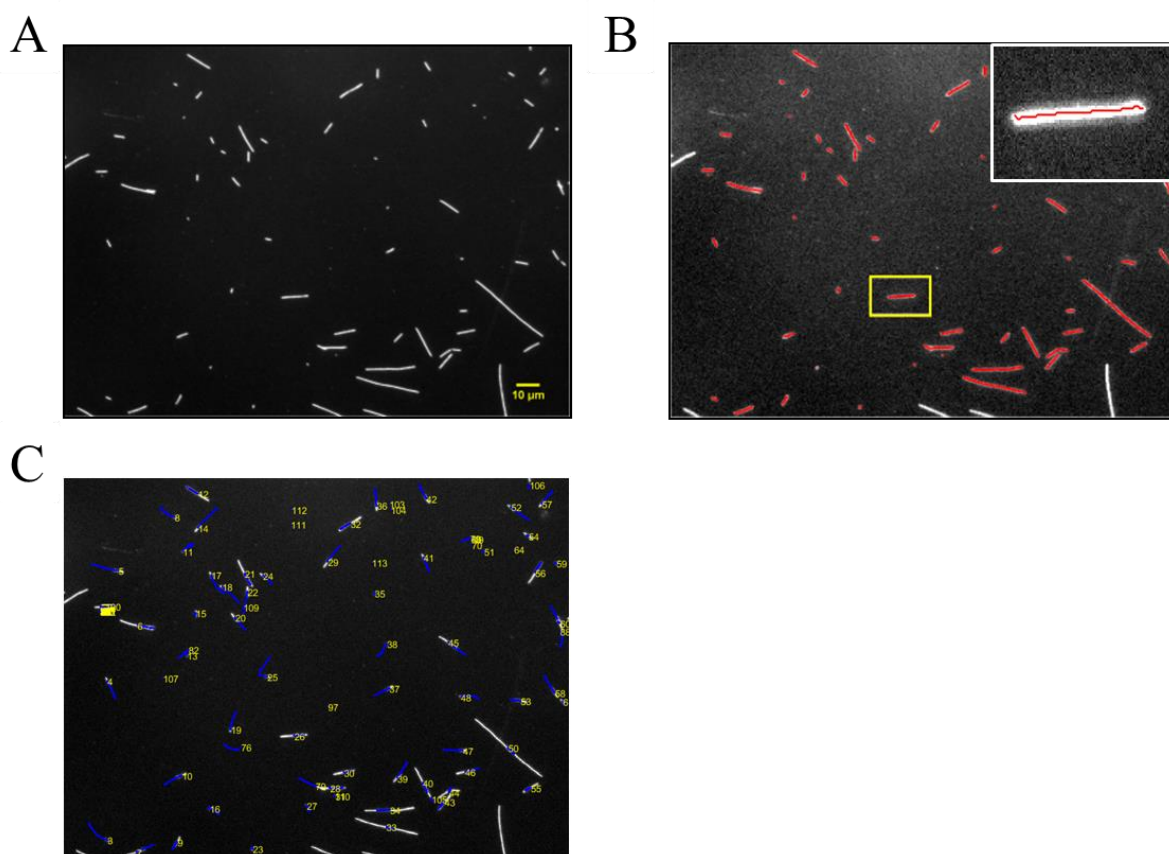


Figure 4.7. Tracking kinesin-driven microtubules. (A) Still image from an *in vitro* gliding assay experiment showing taxol-stabilized microtubules moving on immobilized kinesin motors. Scale bar 10 μm. (B) Filaments are segmented by FluoreT and their skeletons are marked in red. The filament marked in a small yellow box is magnified and shown as the inset. (C) Motion trajectories (blue lines)

of filament-centroids tracked by FluoreT are overlaid on the image. The numbers indicate filament IDs.

FluoreT could effectively segment and skeletonize all the filaments in each image (Figure 4.7B) of the time-series (31 frames) using an automated threshold. The kinetics of movement was tracked only till the filaments remained within the image frame and away from the image borders. Centroids of filaments were detected and tracked by the tool, generating (x,y) trajectories (Figure 4.7C).

The 2D position coordinates from trajectories were used to calculate the MSD of filaments over time (Figure 4.8A) based on equation 2.2 (see Chapter 2). Fitting the average MSD curve to the anomalous diffusion model (Equation 2.4) yielded an anomaly parameter $\alpha = 1.7$, which clearly indicates the super-diffusive nature of filament movement as they are transported and driven by the action of motors bound to them.

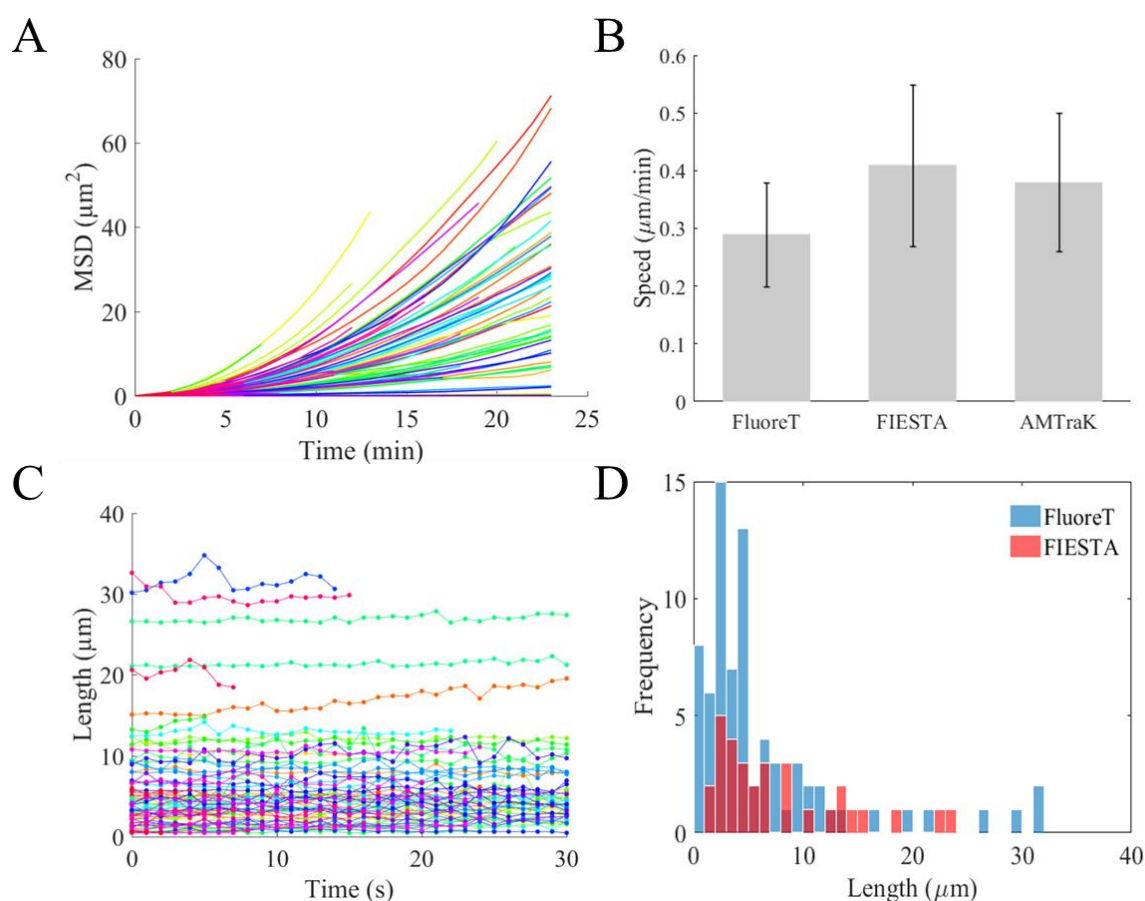


Figure 4.8. Motility and length dynamics of microtubules analysed by FluoreT. (A) MSD profiles of individual filaments tracked in Figure 4.7 are shown. (B) Filament speed measured by FluoreT is compared with measurements by other automated tools. FIESTA is a nanometer-precision 2D particle tracker and AMTraK (see Chapter 3) is an automated kymography tool. (C) Length dynamics of

taxol-stabilized filaments were analysed post tracking. (D) Distribution of microtubule lengths measured by FluoreT and FIESTA are compared.

Motility parameters such as displacement, speed and tortuosity of filaments were estimated using the position coordinates obtained from tracking. We compared the speed estimates from FluoreT with those from 2 other image analysis tools, namely FIESTA (Ruhnow et al., 2011) and AMTraK (Chaphalkar et al., 2016). While FIESTA is a 2D tracking program, AMTraK performs kymography in an automated manner with sub-pixel accuracy (described in Chapter 3). We find that for the given image data, the mean filament speeds estimated by all the three tools are comparable (Figure 4.8B). The number of filaments tracked using the three tools were varied, FluoreT-78, AMTraK-10, FIESTA-31.

In addition to position and motility parameters, the length dynamics of filaments was tracked over time using FluoreT. As the filaments were taxol-stabilized, they showed minimal variation in length over time, as expected (Figure 4.8C). The length estimates of filament populations measured by FluoreT and FIESTA were compared and the average lengths were found to be similar (6.37 μm and 7.78 μm respectively) (Figure 4.8D). However, FIESTA appeared to underestimate the number of filaments in comparison to FluoreT (Figure 4.8D).

4.5. Discussion

We have developed FluoreT-- a MATLAB-based 2D particle tracking tool integrated in a GUI-- that detects and tracks labelled particles in fluorescence microscopy image time-series. The intensity-based detection of centre-of-mass of particles is followed by nearest-neighbour based linking to generate trajectories that describe the movement of particles over time. In addition to parameters of motility such as speed, directionality and MSD, FluoreT also follows the length dynamics of particles in fluorescence microscopy images.

We test the position detection accuracy of FluoreT using simulated noisy images of circular particles and find the error to be sub-pixel even at SNR as low as 4. The accuracy of length detection was tested using experimental images of microtubules as well as simulated filaments. On comparing the measures of length obtained from FluoreT with manual measures, we find that the error in length detection is sub-micron and is independent of filament length (Figure 4.5B). It is important to note that the algorithmically determined lengths are slight underestimations as compared to mean manual lengths. However, this trend was not seen in length measurements of simulated filaments (Figure 4.5D). The

underestimation in experimental images could simply be the effect of a manual bias while measurement, as we have no information about the ‘true’ size of objects imaged in diffraction limited microscopy images.

Although multiple automated tools are available for particle tracking in fluorescence microscopy data (Chenouard et al., 2014), FluoreT stands out as a user-friendly program that detects and traces particles over time with minimal adjustable parameters. FluoreT could effectively track diffusive and directional movement of simulated particles and was further tested on experimental data of labelled microtubule filaments gliding on kinesin *in vitro*. The super-diffusive motion of filaments was identified by confirmed by anomaly parameter greater than 1 (Figure 4.8A). The speed of movement and length of filaments was found to match with measures from FIESTA. However, we note that the number of filaments tracked by FIESTA were two fold lower than those tracked by FluoreT (Figure 4.8D) and FluoreT appeared to track all filaments in the field of view (Figure 4.7C).

In future, FluoreT could be improved significantly in terms of segmentation accuracy by implementing Gaussian fitting or alternative segmentation algorithms (Ulman et al., 2017) and allow users to choose a suitable method for their dataset. Currently, FluoreT performs centroid-based tracking. As centroid-based tracking is sensitive to fluctuations in particle shape, FluoreT could be extended further to obtain tip information from particles with high aspect ratios such as filaments. This information would be useful especially in case of tracking length dynamics of filaments such as microtubules (without taxol stabilization) that grow and shrink over time and show different polymerization and depolymerisation kinetics at both ends. In order to resolve spatial overlaps and crossovers in filaments, ‘branch pruning’ (Athale and Chaudhari, 2011b) that relies on running angles of skeleton pixels, or ‘multi-assignment’ algorithms designed for high density data (Kirubarajan et al., 2001) could be implemented. This would help to improve the accuracy of the tool in conditions of low SNR and high particle density.

4.6. Conclusion

Fluorescence Tracker (FluoreT), is a single particle tracking software developed for high throughput quantitation of object motion and length in 2D. The speed of kinesin motors associated with microtubules in an *in vitro* assay is estimated using the tool (0.29 $\mu\text{m/s}$) and is comparable to measures from other software. FluoreT is found to display sub-pixel accuracy of position detection and reproduces identical values of parameters of motion when

tested on simulated noisy data. The MATLAB-base and extensibility of FluoreT allows the scientific community to build on the code to enhance existing features of segmentation and tracking. The interface is very user-friendly with minimal number of tuneable input parameters to help users irrespective of their programming expertise to process image data using this platform.

Chapter 5

Differential Interference Contrast Object Tracker (DICOT) for particle motility analysis in label-free images

Overview

In contrast with fluorescence microscopy, label-free imaging techniques such as Differential Interference Contrast (DIC) allow the observation of cells and large subcellular structures in their native, unperturbed states with minimal exposure to light. Owing to these advantages, there exists a demand for more and robust image-analysis routines that can automatically process DIC images in order to gain quantitative insight into cellular and subcellular processes. In the following chapter, I present DICOT, a novel program for comprehensive 2D tracking of objects in DIC images based on simple objective criteria for detection and linking. The tool is shown to reproducibly quantify in a high-throughput manner, the diffusive behavior of micron-sized beads and the rheology of solvents in which they are suspended.

5.1. Introduction

Several cells and tissues are transparent and colourless in nature and cannot be observed by plain light microscopy unless stained. The visualization of such tissues, cells and subcellular organelles necessitated innovations in light microscopy in the past. Since over two decades, the goal of observing cells and intracellular processes is routinely being achieved by labelling biomolecules with compatible fluorophores and subsequently imaging them under fluorescence microscopes. These fluorophores can either be genetically expressed within cells or be physically introduced into the system. However, the invasive nature of these methods may perturb cellular systems and alter their behaviour (Sarah Grah et al., 2017). In addition, the phototoxicity that results from prolonged exposure to high intensity beams of light in such experiments may affect the viability of the specimen being imaged (Dixit and Cyr, 2003).

Label-free imaging techniques overcome these challenges by generating contrast using inherent features such as refractive index and density differences in a sample, without the use

of fluorophores. Traditional label-free techniques such as Differential Interference Contrast (DIC) and phase-contrast allow the observation of living cells and subcellular structures (Kasprowicz et al., 2017; Sarah Grah et al., 2017) with minimal exposure to light.

Although single particle tracking is a powerful technique commonly employed to analyse fluorescence microscopy images (see Chapter 4), specialized tools for particle tracking in label-free images are scarcely available. Furthermore, most of the available software tools are designed to analyse phase contrast images (Sliusarenko et al., 2011; Guberman et al., 2008) as segmentation of DIC images is more complex than that in phase contrast. This is because, in phase contrast images, objects appear uniformly dark (with a characteristic halo) over a relatively lighter background. However, the DIC image of an object is a combination of light and dark regions that gives a pseudo-3D effect. The object appears as if it were illuminated from a certain direction at an angle, casting a shadow on a part of itself. While particle detection algorithms developed for fluorescence images leverage the difference in intensities of the signal and background, the lack of such clear difference in intensities and the non-uniformity of illumination in DIC make segmentation in such images particularly challenging.

Current algorithms in the field of automated DIC segmentation and tracking range from to template-based methods (Piccinini et al., 2016) to machine-learning (Carpenter et al., 2006). Here, we describe differential interference contrast object tracker (DICOT), a novel program that implements gradient detection (Athale and Chaudhari, 2011b) and adaptive thresholding (Bradley and Roth, 2007) to segment and extract position and size information of objects in DIC images. Trajectories that are generated by linking the position coordinates in time by nearest neighbour approximation, are used further to comprehensively quantify the spatiotemporal dynamics of objects.

5.2. Materials and Methods

5.2.1. Microscopy of diffusive beads

Monodisperse polystyrene beads (NIST Traceable Particle Size Standards, Bangs Laboratories Inc, IN, USA) of radius 0.5 μm and dilution 1:100 (v/v) were used for diffusion experiments (experiments and microscopy was performed by Yash Jawale). Beads suspended in distilled water or 25% (v/v) glycerol (Glycerol 99% GC, Sigma-Aldrich Inc., USA) were flowed into a double-backed tape chamber (dimensions - 1 cm x 1 cm x 0.01 cm) made using a slide and coverslip. Time-lapse images were acquired every 0.5 s for 50 s in DIC mode with

a 40x (NA 0.6) CFI S Plan Fluor ELWD lens and 60x (NA 0.7) Super Plan Fluor ELWD ADL lens and Andor Clara CCD camera mounted on a Nikon Eclipse Ti-E inverted microscope (Nikon Corp., Japan). The imaging was carried out at 25⁰C.

5.2.2. Image pre-processing and segmentation

DIC images of control beads were pre-processed to enhance contrast (with 0.3% saturated pixels) using Fiji (Schindelin et al., 2012).

Segmentation: Two core alternative methods are employed by DICOT for segmentation of images after a customized background correction routine:

Adaptive thresholding

This method (Bradley and Roth, 2007) considers local variations in illumination and computes an integral image of the input image. The mean intensity (μ_i) of a fixed window of neighbouring pixels is calculated at each pixel position. That pixel is considered as background if its original intensity is less than $t\%$ of μ_i and foreground if the original intensity is less than μ_i . The factor t is dependent on image size.

Gradient detection

In order to segment objects in DIC images, a pixel-wise gradient is calculated in neighbouring pixels in X and Y directions. Each neighbouring pixel is an average of a window of pixels. The two gradient images are binarized using a threshold and combined and skeletonized to obtain object information (Athale and Chaudhari, 2011b).

5.2.3. DICOT implementation specifics

The DICOT code was implemented in MATLAB R2014b (MathWorks Inc., USA) in combination with the Image Processing (version 7.0) and Statistics (version 7.3) toolboxes and was tested on Linux, Mac OSX and Windows 10 platforms.

5.2.4. Data analysis

All data analysis and plotting was performed using MATLAB 2014b and 2016a (MathWorks Inc., USA). The effective diffusion coefficient of bead motility was calculated by MSD analysis and Perrin's method (described in Chapter 2, Section 2.9). Viscosity of the solvent was estimated by Stokes-Einstein relation (Chapter 2, Section 2.10). Fitting of custom

functions was performed using either the Levenberg-Marquardt non-linear least square routine or the trust-region method, implemented in the Curve-Fitting toolbox (version 3.5 and above) of MATLAB.

5.3. Algorithm and Workflow

The differential interference contrast object tracker (DICOT) is an open source program based on an algorithm that combines segmentation of objects and distance minimization based linking to quantify dynamics of label-free DIC image time-series. The program has a GUI front-end and is accompanied by a detailed help file. The algorithmic workflow (Figure 3.1) is divided broadly into three steps:

- (a) Object detection
- (b) Tracking
- (c) Statistics

These steps in the workflow are reflected in the graphical user interface (GUI) layout (Figure 3.2).

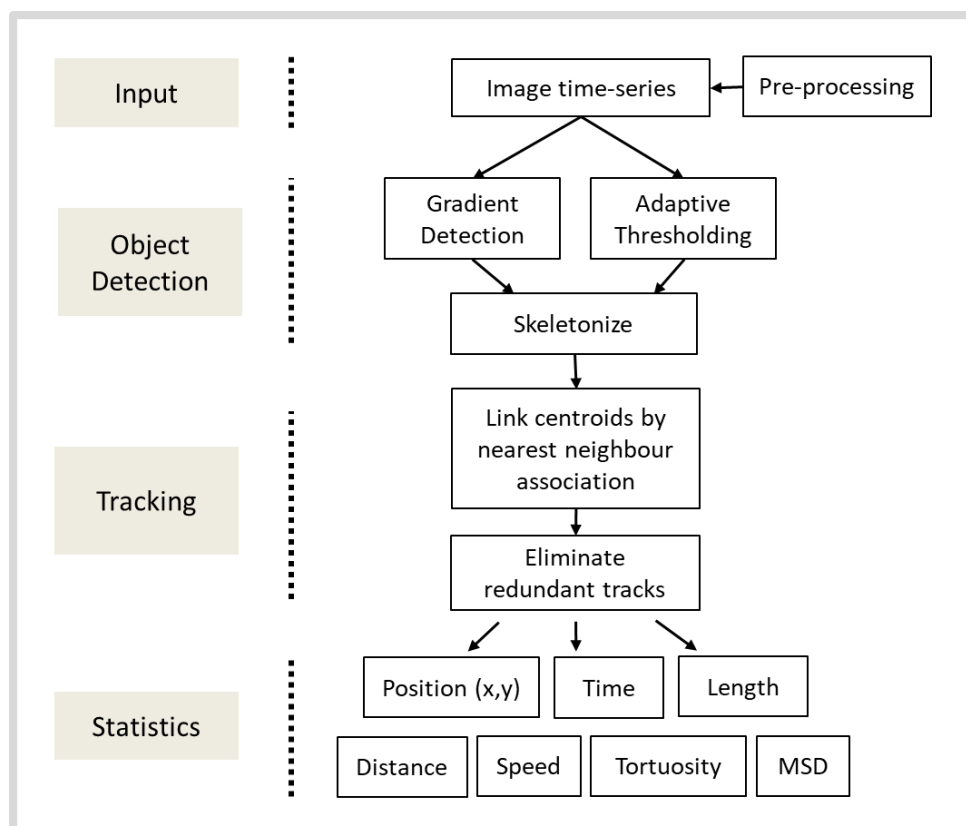


Figure 5.1. Algorithm. The workflow of the algorithm involves three steps (1) object detection, (2) tracking and (3) quantification to obtain statistics from the input image time-series.

The functioning of each of these steps is briefly described as follows:

(a) Object detection:

The user chooses an input image time-series with the ‘Open File’ button. Image time-series are assumed to be uncompressed, 8 or 16-bit multi-page TIF files. The user can choose to process either the whole or a subset of frames using the ‘Frame nos.’ text box. For example entering ‘2:2:8’ will now result in only frames 2, 4, 6 and 8 being processed for further analysis. The output will be stored in a subfolder named ‘dicot-<name of input file>’ in the same directory as the image. The drop-down menu ‘Units’ allows the user to select distance and time units, and the text boxes ‘Pixel size’ and ‘Time interval’ are used to provide conversion factors per pixel and frame respectively. This results in scaling the pixels and frame numbers to physical units. Objects could be detected selectively by applying minimum and maximum size thresholds. Background subtraction is performed to aid accurate segmentation, for which a pseudo-background is created by filtering the test image itself. The size and SD of this ‘Gaussian filter’ can be specified in the adjacent boxes. We set size ‘11’ and SD ‘5’ as default values which may be varied by the user depending on the image data. Two alternative methods of object detection have been implemented in DICOT. The first method is a modified form of the ‘Gradient detection’ algorithm (Athale and Chaudhari, 2011b) which marks the skeletons of objects by calculating the gradient in neighbouring pixel values in X and Y directions such that each neighbouring pixel is an average of ‘ n_g ’ neighbours. The parameter ‘Gradient mask’ allows the user to set the value of n_g to suit the current data. Alternatively, the ‘Adaptive thresholding’ method computes a local threshold based on mean or Gaussian-weighted mean intensity at each pixel and compares it with the intensity of the pixel. The size of the neighbourhood is determined from the ‘Adaptive mask’ parameter (n_a) and image size (K), such that the neighbourhood size is $2*K/n_a + 1$.

Clicking the button ‘Locate’ commences the segmentation.



Figure 5.2. DICOT interface. The GUI allows the user to provide input in the ‘Parameters’ panel, which is processed to obtain statistics that are displayed in the ‘Operations and Display’ panel.

(b) Tracking:

Once objects are detected, the user needs to fill in parameters of tracking. The list of centroids $P(t)$ for each time point t is linked resulting in tracks, based on user input parameters of ‘Search radius’ (λ_1) and ‘Min. track length’ (λ_2). Centroids (see Chapter 2) are linked if the minimal pair-wise distance $d_j(t, t+\tau)$ between every j^{th} centroid in successive frames ($t, t+\tau$) satisfies the condition $\min(d_j(t, t+\tau)) \leq \lambda_1$ iteratively for the j^{th} centroid in every subsequent time frame ($t + \tau$). The centroids that do not form a part of any trajectory are treated as start-points of new trajectories. Trajectories are eliminated from further analysis if their number of centroids linked $\text{len}(P) \leq \lambda_2$, to avoid artifacts due to very short tracks. If the checkbox ‘Remove redundant tracks’ is selected, each i^{th} track with η_i coordinates, is tested for intersections using the inbuilt *intersect* function. If the number of common coordinates (η_c) satisfies the condition $\eta_c \geq \eta_i/3$, it is eliminated as a redundant track.

The code produces both text-file outputs and plots of the dynamics estimated from the tracking. The end of tracking is marked by the display of coloured trajectories overlaid on the first image of the original time-series. Parameters used for object detection and tracking are stored in a text file on using the ‘Save Parameters’ button.

(b) Statistics:

The ‘Make and save movie’ button produces and saves the output of tracking as a multi-page TIF file in the same subfolder. The user may want to tweak the tracking ‘search radius’ and re-run the tracking if spurious trajectories are observed at this stage. After satisfactory tracking, the ‘Quantify’ button is invoked to proceed with quantification. The ‘number of objects detected’ are displayed in the panel as soon as basic trajectory-wise quantification is completed. A flexible display allows the user to choose between average statistics of ‘All’ trajectories or a specific ‘Individual’ trajectory picked from the drop-down menu. The mean (μ) and standard deviation (σ) of these variables are generated in the text boxes. Additionally, frequency distributions of Distance, Time, Speed and Tortuosity (i.e. directionality) and Length are plotted if the button ‘Plot’ corresponding to these variables is pressed.

Mean square displacement analysis of all detected trajectories is performed on pressing the ‘MSD’ button. A window with plot of the average MSD against increasing time-step is displayed. Ticking the ‘Fit MSD’ option *a priori* helps the user to extract the value of the average two-dimensional diffusion coefficient by fitting the entire or a fraction of the average MSD curve to the anomalous diffusion model (Equation 2.5, Chapter 2). Time-dependent dynamics of length of skeletons of detected objects can be visualized by clicking the ‘Length dynamics’ button. While the segmentation module of the tool detects lengths for elongated objects (aspect ratio >1) (Athale and Chaudhari, 2011), the length of a circular object measured here is along a chord of the circle rather than its diameter.

Outputs of the analysis are stored in multiple tab-delimited text files to enable reproducible analysis and are summarized in Table 3.1.

Table 3.1. Description of output files generated by DICOT.

Function	Sr. No.	Output file	Description
Locate	1	segmentation.tif	Image of detected objects with skeletons overlaid in red
	2	untracked.txt	Frame-wise record of detected objects prior to tracking
Track	3	trajectories.txt	(x,y) Coordinates and lengths of tracked objects
	4	trackingmovie.tif	TIF movie of tracked objects where the current position is marked in blue, trajectory in red and particle ID is displayed in yellow
Make movie	5	trajoverlaid.tif	Trajectories (blue) overlaid on the first image
	6	InstStats.txt	Instantaneous (stepwise) statistics of each trajectory
Quantify	7	StatsPerTrack.txt	Averaged statistics of each trajectory
	8	MSD_vs_Time.tif	Mean square displacement profiles
MSD	9	AvgMSD_vs_Time.tif	Average MSD curve with fit
	10	ID_Time_MSD.txt	Track-wise MSD
	11	Length_vs_Time.tif	Time-dependent statistics of length of skeletons of tracked objects
Length dynamics	12	elongrate.txt	Elongation rates of objects
	13	Parameters.txt	Record of parameters of particle segmentation and tracking
Save Parameters			

5.4. Results

5.4.1. Diffusive motion of beads

The ability of DICOT to segment and track particles in DIC mode was tested using DIC image-series of 1 μm diameter beads suspended in two solvents, water and 25% glycerol solution. The density of beads was chosen such that they could space out evenly in the field of view and did not hinder each other's movement. The centroids of beads were detected by either by gradient detection or adaptive thresholding (*insets* of Figure 5.3A, 5.43A) and tracked in time for at least 5 s using a nearest-neighbour search to generate trajectories (x,y)

(Figure 5.3A, 5.4A). The resulting position information was used to calculate the effective diffusion coefficient by MSD analysis and Perrin's method.

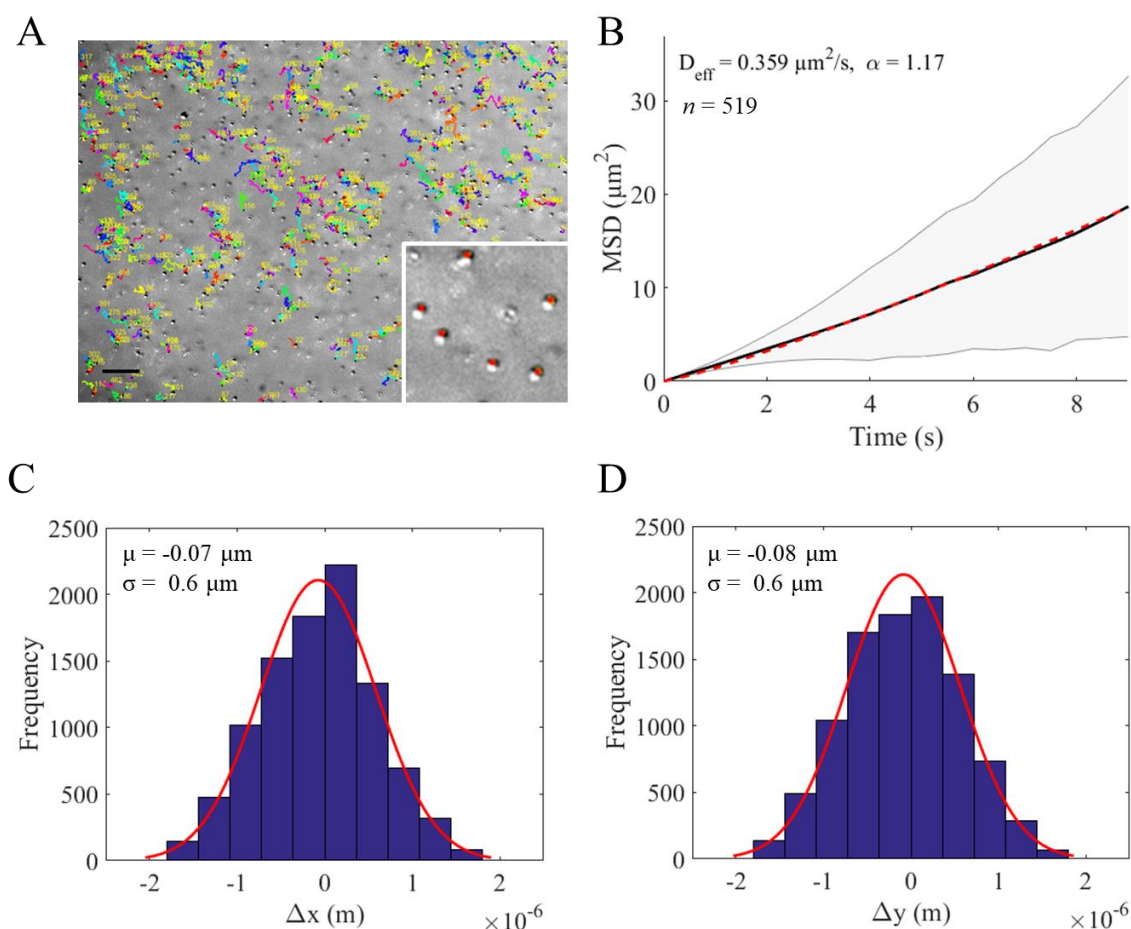


Figure 5.3. Diffusive motion of beads suspended in water. (A) Trajectories from 2D tracking are shown as coloured lines overlaid on DIC images of beads. Scale bar 10 μm . *Inset:* Magnified image of beads (segmented by adaptive thresholding) overlaid with centroids (red dots). (B) Average MSD profiles (black solid lines) were fit (red dashed line) to the anomalous diffusion model (equation 2.3) to obtain effective diffusion coefficients. Shaded gray region indicates standard deviation. Distribution of step-sizes of beads along the (C) X-axis and (D) Y-axis with their Gaussian fits (red) are shown.

The MSD analysis (Figure 5.3B, Figure 6.3B) helps to not only quantify the D_{eff} , but also helps to reveal the nature of movement of objects by quantifying the anomaly parameter (α) by fitting the average curve to the anomalous diffusion model. The motion is said to be purely diffusive if $\alpha = 1$, sub-diffusive or ‘restricted’ when $\alpha < 1$ and super-diffusive or ‘transported-like’ when $\alpha > 1$.

We find that beads suspended in both the solvents showed purely diffusive behaviour upto timescales of ~ 9 s, as the α values obtained from fits were close to 1 (Figure 5.3B, 6.3B). Perrin's method, on the other hand, applies only to particles undergoing pure Brownian

motion with equal probability of being displaced in the X and Y directions. For purely diffusive objects, average of the distribution of displacement in X and Y (Δx and Δy) is 0. In case of beads suspended in solvents, the distributions of Δx and Δy were found to be similar to each other, hinting at the isotropic nature of the medium. Gaussian fits to these distributions show an average around 0 (Figure 5.3 C, D and Figure 5.4C, D), confirming the Brownian motion of beads. Velocity auto-correlation analyses performed with bead trajectories also suggest diffusive movement upto ~ 12 s (data not shown).

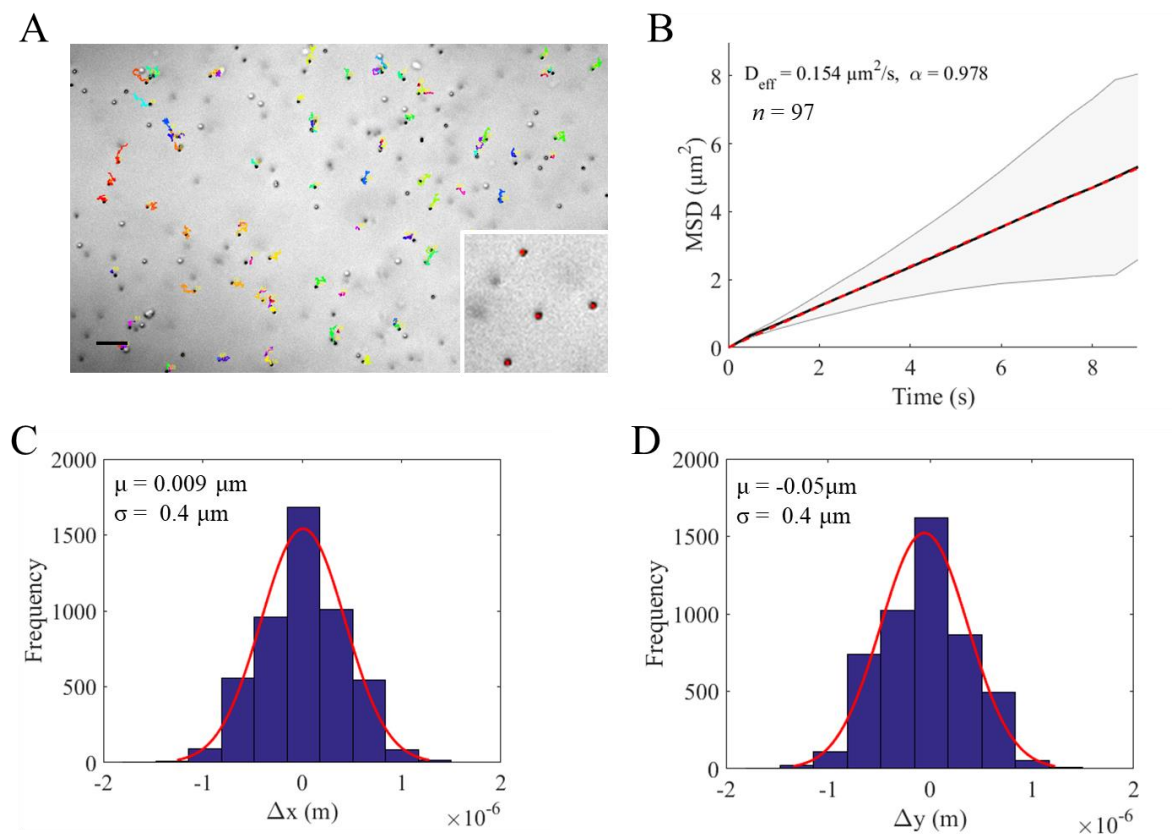


Figure 5.4. Diffusive motion of beads suspended in glycerol solution. (A) Trajectories from 2D tracking are shown as coloured lines overlaid on DIC images of beads. Scale bar $10 \mu\text{m}$. *Inset*: Magnified image of beads (segmented by adaptive thresholding) overlaid with centroids (red dots). (B) Average MSD profiles (black solid lines) were fit (red dashed line) to the anomalous diffusion model (equation 2.5) to obtain effective diffusion coefficients. Shaded gray region indicates standard deviation. Distribution of step-sizes of beads along the (C) X-axis and (D) Y-axis with their Gaussian fits (red) are shown.

As predicted, the D_{eff} of beads was found to be greater in water as compared to 25% glycerol, as estimated by both methods- Perrin and MSD. In order to validate these measures of bead motility determined by DICOT, we used the Stokes-Einstein equation that relates the diffusion coefficient to viscosity of the solvent to quantify the viscosity of water and glycerol (Figure 5.5).

5.4.2. Estimation of viscosity of water and glycerol

The viscosity value of water estimated using the D_{eff} values based on Perrin's method and MSD were found to be comparable to each other (Figure 5.5) and to the reported value ($0.89 \times 10^{-3} \text{ Pa s}$ at 25°C) that was determined experimentally using viscometers (Korson et al., 1969; Rob Phillips et al., 2012).

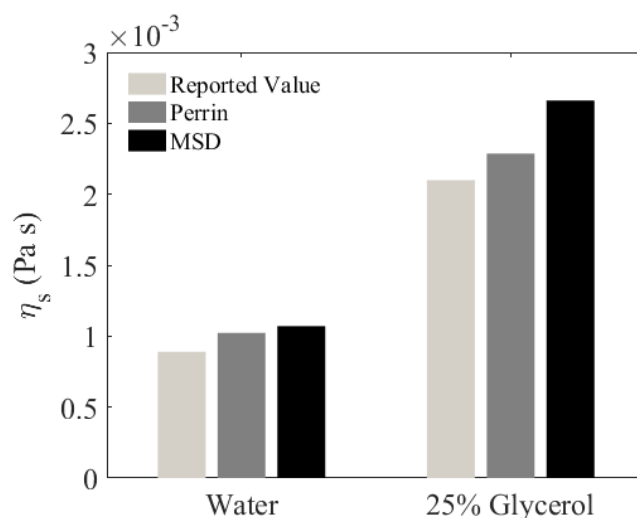


Figure 5.5. Viscosity of the solvents. Mean viscosities (η_s) of the two solvents, water and 25% (v/v) glycerol solution, were estimated using D_{eff} obtained by MSD and Perrin's methods and compared with published values.

Similarly, the estimated viscosity of 25% glycerol solution by the two methods were found to be comparable to each other and consistent with experimentally determined viscosities within the given range of temperature (Segur and Oderstar, 1951). This suggests that the motility parameters estimated by DICOT are reliable and accurate.

5.5. Discussion

In this chapter, I describe DICOT, an automated 2D particle tracker implemented in MATLAB, developed to process time-lapse images from DIC microscopy. DICOT detects the centroids of objects and links them in time based on a nearest-neighbour approach to generate (x,y) trajectories. The tool is integrated in an easy-to-use, intuitive GUI that allows the users to fine-tune the parameters of object detection and tracking for optimal results and also displays the output in the form of statistics of object motility and length.

The nearest-neighbour search is a method to temporally link particles detected in each image frame. In successive frames of the image-series, position coordinates that are closest in terms of distance and time make up a single trajectory. The method is simple, computationally less intensive and generally applicable, but works best with low density of objects whose velocity of movement is often lesser than the inter-object spacing. This prompted us to assess the sensitivity of this method to the input ‘search radius’. When we plotted the estimated viscosity (an indirect measure of the D_{eff} of suspended beads) as a function of search radius, we found that the optimal search radius is data-set specific. In the case of water, tracking search radius that resulted in viscosity comparable to the reported value (0.001 Pa s) was $\sim 1.8 \mu\text{m}$. The solvent viscosity estimated using D_{eff} values appears to vary with varying search radius (Figure 5.6). Therefore, in the case of tracking based on distance minimization, a careful choice of search radius is essential.

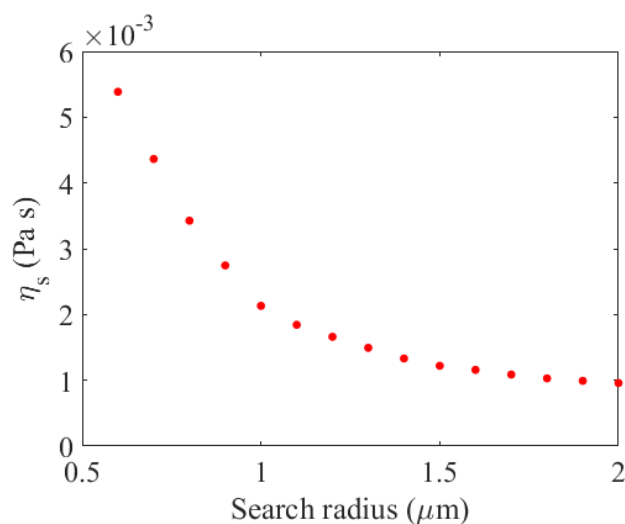


Figure 5.6. Estimated viscosity of water is plotted as a function of the ‘search radius’ parameter in DICOT.

An initial guess could be made based on the following expression:

$$\text{SR} \sim d_{\text{max}} < \mu_{\text{space}} \quad (\text{Equation 5.1})$$

Here, SR is search radius, d_{max} is the maximum instantaneous displacement of objects per frame and μ_{space} is the average distance between two objects in the image. d_{max} and μ_{space} could be roughly approximated by eye. The value of SR could be optimised if need be, such

that at that input SR there are no spurious trajectories in the output movie ‘Trackingmovie.tif’.

It is important to note that a range of values of search radius (between 1.6 and 2 μm) yielded saturating values of viscosity of water, close to the reported value (Figure 5.6). Thus, it is fair to assume that slight variation in the search radius does not compromise the accuracy of the measurement. For very high densities of objects, however, one may require to employ density corrections on the viscosity obtained by the Stokes-Einstein relation. In future, additionally introducing more involved, object-identification-based algorithms as alternatives for tracking in DICOT would substantially reduce the influence of search radius.

Gradient detection and adaptive thresholding are the two different segmentation methods employed in DICOT. Either of the two could be chosen by the user based on the data being analysed. Typically, we recommend the use of the gradient method for objects with aspect ratios greater than 1, such as rod-like *E. coli* cells. The adaptive thresholding method is useful in segmenting spherical objects. In the rare event of finding image-series with objects that are segmented well by both methods, the choice is governed by efficiency of the algorithm. For example, we take the case of our image-series with 1 μm beads, imaged at 63x magnification and segmented by both the methods (Figure 5.7A, B). Although both methods detected similar number of trajectories and resulted in comparable measures of D_{eff} (Figure 5.7C), the adaptive thresholding method was found to be faster, i.e. more efficient than gradient detection.

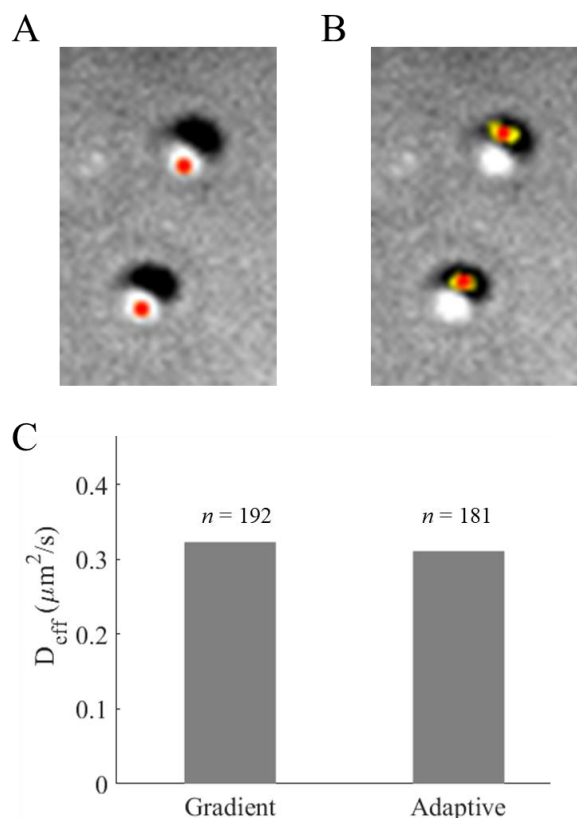


Figure 5.7. Comparison of segmentation methods used in DICOT. Bead images segmented by (A) gradient detection method and (B) adaptive thresholding method are shown. The yellow line indicates the detected skeleton of spheres, while centroids are marked as red dots. (C) Mean effective diffusion coefficients calculated by analyzing the same dataset with both methods are compared.

The displacement distributions of beads in X and Y directions centre are seen around mean 0 (Figure 5.3C, D; Figure 5.4C, D), indicating that both solvent media are isotropic. Thus the beads are equally probable to be displaced in X, Y or Z directions. This led us to think, what if a bead moves in Z, but shows no displacement in X and Y? Would the (x,y) trajectory of such a bead represent the true 2D- D_{eff} ? However as an answer to these questions, we reason that the displacement of the bead in Z would make it go out of focus and such a blurred image of the bead is not segmented by DICOT's algorithm. Additionally, our time-frame cut-off ensures that only objects that are consistently detected in each consecutive frame make up a trajectory. Both these factors allow us to indirectly ensure that the movement we detect is only indeed in the XY plane. As a result, our estimation of viscosity of the solvents based on 2D particle tracking yields values consistent with published literature.

We compared the output from DICOT with CellTracker (Piccinini et al., 2016) that tracks particles in DIC images based on template selection and distance minimization. The average

speeds measured for a single bead image-series with DICOT and CellTracker were found to be consistent with each other ($1.64 \mu\text{m/s} \pm 0.3$, $1.58 \mu\text{m/s} \pm 0.14$). To its advantage, DICOT does not require additional template selection or training prior to segmentation and tracking, as was seen with the other tool. Also, as a novel feature, DICOT implicitly outputs motility parameters such as directionality and effective diffusion measures, in addition to object displacement and speed. For objects with high aspect ratios, the gradient detection based segmentation module in combination with distance based tracking could be utilized in future to track lengths of elongated rod-shaped structures such as *E. coli* cells or cytoskeletal filaments.

5.6. Conclusion

DICOT is a comprehensive tool based in MATLAB, developed to automatically segment and track objects in DIC images, in order to quantify the dynamics of their movement and length. The tool was validated on experimental image-series of micron-sized beads diffusing in water and 25% glycerol and the values of viscosity of both solvents (0.001 Pa s and 0.0026 Pa s respectively) were found comparable to literature. Owing to its objective tracking criteria and user-oriented interface, DICOT could be applied to gain new insights in old biological problems through high throughput analysis of label-free imaging data.

Chapter 6

Cytoplasmic Viscosity Varies and Correlates with Spindle Motion Among Zygotes of Related Nematode Species

Overview

Precise positioning of the mitotic spindle is essential for the determination of the division-plane and the subsequent first asymmetric cell division in various species of nematode embryos. In addition to the well-studied interactions of the spindle with the cell cortex, viscoelastic properties of the cytoplasm are speculated to be involved in the patterns of spindle motion observed during positioning. In this chapter, we use a microrheology approach to estimate the cytoplasmic viscosity of multiple nematode zygotes. To this end, we apply DICOT (described in Chapter 5), a MATLAB-based particle tracking tool to trace endogenous yolk granules imaged within live nematode zygotes by time-lapse DIC microscopy. With this novel, non-invasive method, we estimate the viscosity of the cytoplasm of one-celled embryos belonging to 6 species of nematodes, including *C.elegans*.

6.1. Introduction

In single-celled embryos of nematode species, including the popular model organism *C. elegans*, accurate determination of the plane of cell division is critical during the first asymmetric cell division which is important for establishment of polarity in the tissue. Precise positioning of the mitotic spindle is essential for the determination of the division-plane. Interactions of spindle microtubules with dynein complexes in the cortex are known to affect spindle positioning and motion pattern (Kozlowski et al., 2007; Garzon-Coral et al., 2016; Grill and Hyman, 2005). In previous work, the mobility of the mitotic spindle during the process of asymmetric positioning was shown to vary between nematode species, suggesting an evolutionary difference between spindle mechanics (Valfort et al., 2018; Farhadifar et al., 2015; Riche et al., 2013). A simple hypothesis is that the viscosity of the cytoplasm could give rise to these differences. Indeed, predictions from simulations of spindle-oscillatory mechanics in *C. elegans* have suggested that order of magnitude differences in the

cytoplasmic viscosity can change the qualitative nature of spindle oscillations by mechanical damping (Kozłowski et al., 2007).

In order to understand the biophysical properties of the cytoplasm and the balance of forces acting on subcellular structures such as cytoskeletal spindles, microrheology techniques have been developed previously. While active methods include dragging of beads *in vivo* by optical and magnetic tweezers (Garzon-Coral et al., 2016), passive techniques were based on tracking of Brownian motion of fluorescent nanoparticles injected *in vivo* (Daniels et al., 2006; Chen et al., 2013). However, there are disadvantages to these methods. The invasive nature of such methods and the phototoxicity caused by prolonged exposure to high intensity beams of light and their interaction with the fluorophore may alter the behavior of cellular systems and affect their viability (Dixit and Cyr, 2003). Also, photobleaching of the probes in long-duration imaging experiments may result in poor quality of imaging. In addition, the insertion of exogenous particles in the cells may trigger active transport mechanisms within the cell. Therefore, there exists a need for non-invasive, label-free methods that allow us to quantify biophysical properties of the complex cytoplasmic fluid. Label-free DIC microscopy is especially advantageous to follow the dynamics of subcellular particles without the issues associated with labelling and phototoxicity (Kasprowicz et al., 2017).

Microrheology studies with endogenous probes have been carried out in systems such as *S. pombe* (Selhuber-Unkel et al., 2009) and amoeba (Rogers et al., 2008) to understand how viscoelastic properties of the cytoplasm vary over the cell cycle and affect processes such as locomotion. Here, we apply a novel, high-throughput microrheology approach to estimate the viscosity of the nematode zygote cytoplasm based on automated particle tracking in DIC time-lapse imaging of these cells. The probes of our choice are endogenous, refringent yolk granules composed of lipoproteins. They are ubiquitously found in zygotes of multiple nematode species (Figure 6.1A), including *C. elegans*, and their abundance in the cytoplasm serves as an added advantage.

In this chapter, we employ DICOT (described in Chapter 5), a custom-made, MATLAB-based particle tracking tool to trace yolk granules imaged within live nematode zygotes by time-lapse DIC microscopy. DICOT generates 2D trajectories of tracked particles and further calculates their effective diffusion coefficient. The viscosity of the cytoplasm is then determined by Stokes-Einstein's relation and further corrected for density of the suspended

granules. The cytoplasmic viscosity of zygotes of 6 evolutionarily related nematode species is estimated and compared among each other. We find that effective viscosities vary among these species and correlate with the observed spindle recoil velocities.

6.2. Materials and Methods

6.2.1. Nematode strains, culture and live-cell imaging

The zygotes of 6 nematode species- *Caenorhabditis elegans* (N2), *Caenorhabditis monodelphis* (SB341), *Caenorhabditis remanei* (PB219), *Pristionchus pacificus* (PS312), *Oscheius tipulae* (CEW1) and *Diploscapter coronatus* (JU359) were cultured and imaged by live-cell DIC microscopy in Delattre lab, ENS, Lyon (experiments and microscopy were performed by Thibault Brugiere and Dr. Marie Delattre) as described in (Valfort et al., 2018). Pixel size is 0.065 μm . Time-lapse images of zygotes in pro-metaphase were acquired at the interval of 0.5s. Temperature of 23⁰C +- 2 was maintained throughout the imaging.

6.2.2. Image pre-processing and analysis

DIC images of nematode zygotes were pre-processed to enhance contrast (with 0.3% saturated pixels) using Fiji (Schindelin et al., 2012). Radius of yolk granules was measured manually using Fiji (Figure 6.1B). Granule motion was analysed using Differential Interference Contrast Object Tracker (DICOT), a custom-made DIC 2D particle tracker written in MATLAB (Mathworks, USA) (described in Chapter 5). Subsections of the segments were cropped and used for DICOT analysis (such as those in Figure 6.5A) so as to avoid the effects of the boundary on granule diffusion analysis. MSD analysis was performed as explained in Chapter 2, Section 2.9.1. Solvent viscosity was estimated by Stokes-Einstein's relation (Chapter 2, Section 2.10).

Granule density was measured manually using Fiji and MATLAB for the whole embryo as well as anterior and posterior segments that correspond to 30% of major axis in each species. The absolute granule density and diameter were used to estimate granule packing fraction (ϕ_{2D}).

6.2.3. Density correction of viscosity

The effective viscosity was estimated by correcting the solvent phase viscosity for the density of granules based on the packing fraction (ϕ_{2D}) as follows:

- (i) Quemada method (Quemada, 1977):

$$\eta_{\text{eff}} = \eta_s * (1 - (\phi/\phi_{\text{max}}))^{-2} \quad (\text{Equation 6.1})$$

(ii) Krieger-Dougherty method (Krieger and Dougherty, 1959):

$$\eta_{\text{eff}} = \eta_s * (1 - (\phi/\phi_{\text{max}}))^{-2.5 \phi_{\text{max}}} \quad (\text{Equation 6.2})$$

The maximal packing fraction, ϕ_{max} is taken as 0.64 (Buscall et al., 1994).

6.3. Results

6.3.1. Size and motion of yolk granules in nematode zygotes

Yolk granules in nematode zygotes are roughly spherical in shape (Figure 6.1B). In order to see how the sizes of these granules vary across species, we measured the granule radius ($n_{\text{granules}} \sim 30$ per species) and found it to be comparable among 6 different species (Figure 6.1C).

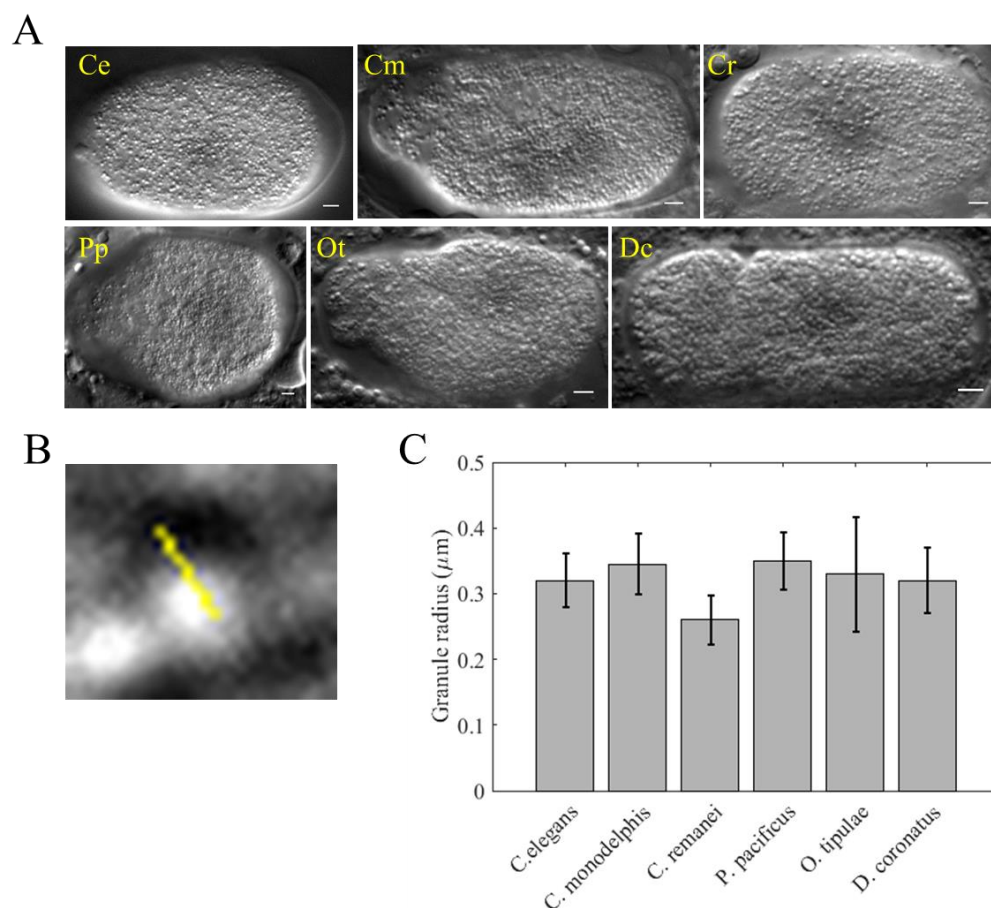


Figure 6.1. Size of yolk granules in nematode species. (A) Yolk granules are imaged by live-cell DIC microscopy in 6 nematode species, *C. elegans* (Ce), *C. monodelphis* (Cm), *C. remanei* (Cr), *P. pacificus* (Pp), *O. tipulae* (Ot) and *D. coronatus* (Dc). Scale bar 3 μm. (B) Magnified image of a

spherical granule is shown. The yellow line indicates the diameter of the granule that is marked manually. (C) Mean radius of granules among the given nematode species is compared ($n_{\text{granules}} \sim 30$ per species). Error bars indicate standard deviation.

The 2D motion of granules was tracked in label-free DIC images over time using DICOT. We find that the movement of granules in all the species varies axially along the zygote. In the central plane of the zygote, the oscillatory motion of spindles during anaphase appears to cause a ‘streaming-like’ effect in the cytoplasm. In this plane of the zygote, two regions of the cytoplasm occupied by the spindle poles are clear of granules, a feature that has previously been used to quantify spindle oscillations (Cluet et al., 2014). Granules tracked by our method in this plane show continuous directional trajectories (Figure 6.2A), suggesting that their movement is affected strongly by spindle motion. In contrast, the granules tracked in the planes away from the centre and relatively closer to the cortex show random-walk like diffusive behavior (Figure 6.2B).

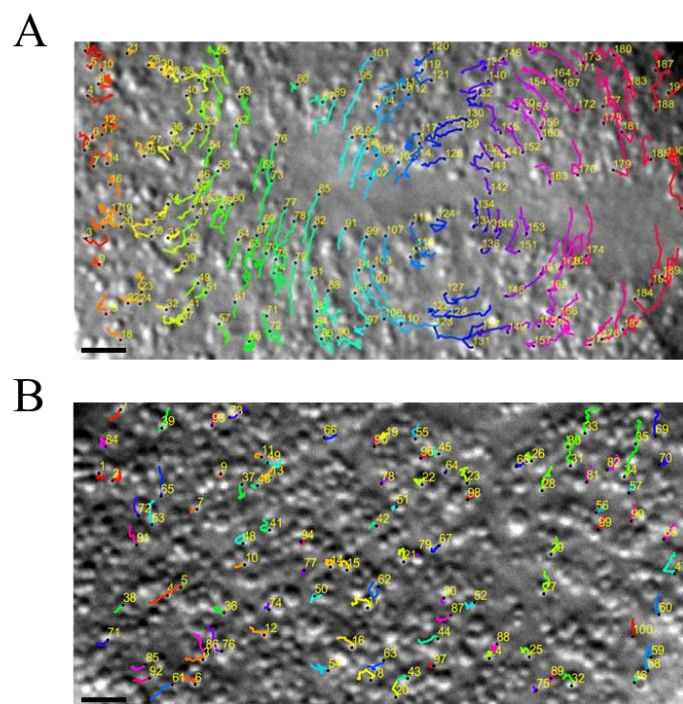


Figure 6.2. Granule motion pattern varies axially in the embryo. Movement of yolk granules was tracked using DICOT in a *C. elegans* embryo in the (A) central and (B) upper planes for 10 s. Coloured lines indicate trajectories. Scale bar 3 μm.

These observations suggest that yolk granules are mostly passive in nature and may be chosen as endogenous probes for a label-free particle tracking microrheology approach to determine the viscosity of the cytoplasm in which they are suspended. In addition, their ubiquitous presence in nematode species and their abundance in the cytoplasm serve as

advantages to arrive at a statistically sound inference. The data was averaged for at least 100 granules per embryo for 10 or more embryos per species.

Granule motion trajectories (x,y) obtained from 2D tracking (Figure 6.3 *left panel*) were further processed using DICOT to calculate the mean square displacement. Individual MSD profiles of hundreds of granules were averaged and fit to the anomalous diffusion model (Figure 6.3 *right panel*) to obtain the effective diffusion coefficient and anomaly parameter values. We find that the effective diffusion coefficient obtained by fitting an average MSD profile is comparable to the one obtained by fitting individual profiles and then averaging the diffusion coefficient values and therefore chose the former.

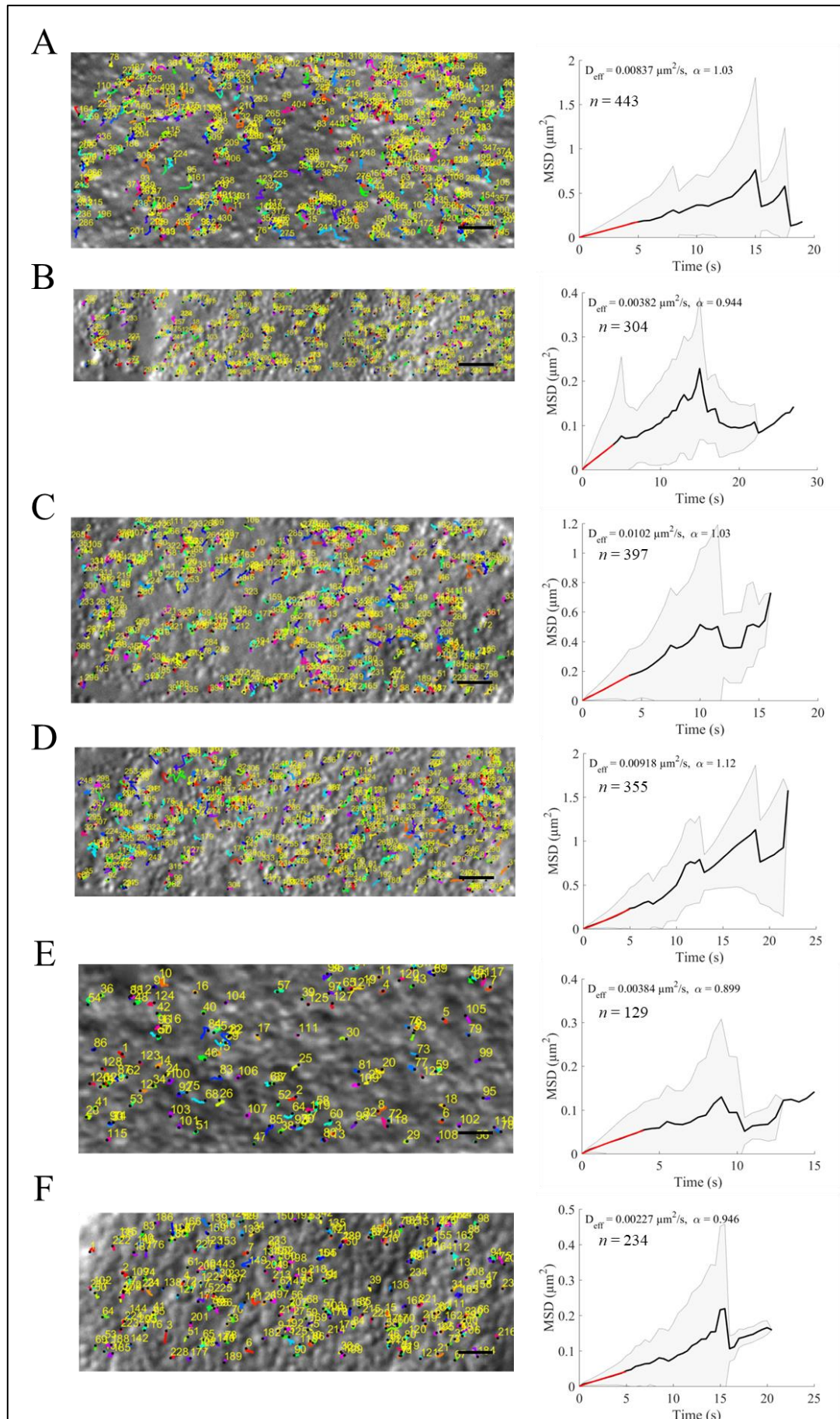


Figure 6.3. MSD analysis of yolk granules. *Left panel-* Trajectories from 2D tracking are shown as coloured lines overlaid on DIC images of yolk granules in one zygote each of species- (A) *C. elegans*, (B) *C. monodelphis*, (C) *C. remanei*, (D) *P. pacificus*, (E) *O. tipulae* and (F) *D. coronatus*. Coloured lines indicate different granules. Scale bar 3 μm . *Right panel-* Average MSD profiles (black solid lines) were fit (red) to the anomalous diffusion model (equation 2.3) to obtain effective diffusion coefficients. Shaded gray region indicates standard deviation.

It is important to note here that our fits to average MSD profiles are limited to short timescales ($\sim 1/4^{\text{th}}$ of the timescale of the entire average profile) as the granules begin to deviate from purely diffusive behaviour above ~ 4 s as indicated by their average MSD profiles (Figure 6.3 *right panel*). The movies used as input were ~ 50 s each and the trajectories we obtain from DICOT lie in the time scales of 5-20s.

Interestingly, a previous study (Daniels et al., 2006) reports super diffusivity of particles above timescales of ~ 1 s and a lack of sub-diffusivity. However, we find anomaly (α) values from 0.667 to 1.47 (averages obtained from different zygotes) (Figure 6.7A), indicating a heterogeneity in granule mobility going from sub-diffusive ($\alpha < 1$) to super-diffusive ($\alpha > 1$). This contradiction in observations could perhaps be explained by the choice of particle size in Daniels et al., which is 100nm (diameter), i.e. ~ 6 times lesser than yolk granules. A recent model of cytoplasmic mobility suggests that particles lower in size than the pore size of the cytoplasm may not undergo restricted diffusion, as opposed to larger particles (Etoc et al., 2018). While we have imaged *C. elegans* zygotes only in the pro-metaphase, similar studies in *S. pombe* report that the sub-diffusivity of endogenous probes is not affected in various stages of cell division (Selhuber-Unkel et al., 2009). The heterogeneity in the anomaly parameter of diffusion of granules also appears to be independent of their position within the cell (Figure 6.7B).

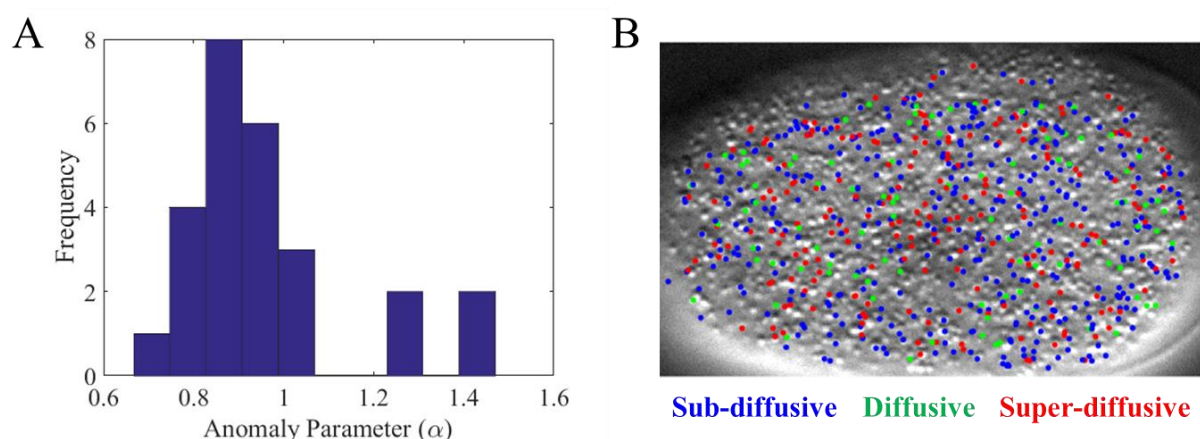


Figure 6.4. Heterogeneity of granule mobility within *C. elegans* zygotes. (A) Distribution of average anomaly parameter (α) values obtained from different zygotes. (B) A mixture of sub-diffusive (blue dots, $\alpha < 0.9$), diffusive (green dots, $\alpha = 0.9$ to 1.1) and super-diffusive (red dots, $\alpha > 1.1$) granules was observed to be distributed in the cytoplasm of a *C. elegans* zygote.

6.3.2. Estimation of solvent phase viscosity of the cytoplasm

The effective diffusion coefficient was calculated by the MSD based method for granules distributed throughout the whole embryo and separately for those in anterior and posterior segments. The A-P segments correspond to regions at the two poles that span $\sim 30\%$ of the length of the major axis of the cell. Subsections of these segments were considered for analysis (Figure 6.5A) so as to avoid the effects of the boundary on granule diffusion analysis. D_{eff} was then used to calculate the ‘solvent-phase’ viscosity (η_s) of the cytoplasm using the Stokes-Einstein’s relation (Equation 6.1).

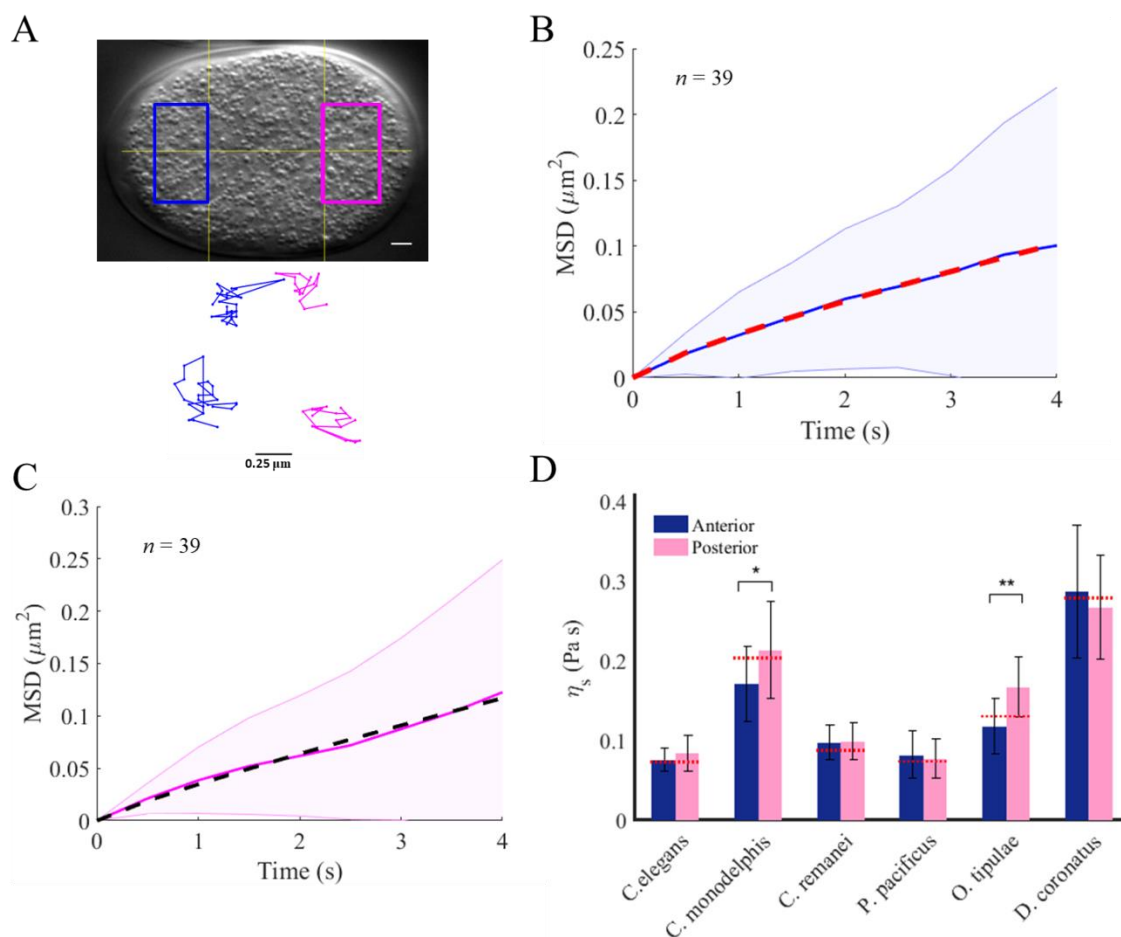


Figure 6.5. Cytoplasmic viscosity of zygotes based on granule movement. (A) Trajectories of granules tracked from anterior (blue) and posterior (magenta) segments of a *C. elegans* embryo. Scale bar $3 \mu\text{m}$. Average MSD profiles of granules for (B) anterior and (C) posterior segments are shown in

blue and magenta respectively. The shaded areas indicate standard deviation. The average MSD curve (solid line) is fit (dashed line) to the anomalous diffusion equation to obtain the effective diffusion coefficient (D_{eff}). (D) Mean (\pm SD) solvent viscosities of anterior and posterior regions of embryos are estimated across 6 species (number of zygotes per species- Ce : 19, Cm : 18, Cr : 12, Pp : 11, Ot : 14, Dc : 10). The viscosities of whole embryos are represented by red dotted lines. *, $P < 0.05$ and **, $P < 0.01$.

The obtained anterior and posterior viscosities were compared among species (Figure 6.4D, summarized in Table 6.1) and found to be maximal in zygotes of *D. coronatus* and *C. monodelphis* species. Our results are in agreement with a previous report that shows that the viscosity along the A-P axis in *C. elegans* embryos does not differ prior to the first cell division (Daniels et al., 2006). However, based on Student's t-test assuming unequal variances, we find that the solvent viscosities along the A-P axis of *C. monodelphis* and *O. tipulae* vary significantly. It is interesting to note that in *O. tipulae* embryos, the oscillatory pattern of the spindle during anaphase prior to the first cell division is different from that in *C. elegans* (Valfort et al., 2018).

Table 6.1. Summary of solvent viscosities (Pa s) of nematode zygotes.

Species	Whole embryo		Anterior		Posterior	
	Mean	SD	Mean	SD	Mean	SD
<i>C. elegans</i>	0.073668	0.013046	0.075225108	0.015042	0.083526213	0.022709
<i>C. monodelphis</i>	0.203763	0.039396	0.171076629	0.047144	0.212847399	0.060487
<i>C. remanei</i>	0.087853	0.013185	0.097320047	0.021931	0.098888292	0.023283
<i>P. pacificus</i>	0.073749	0.032619	0.08182003	0.03012	0.076832674	0.025154
<i>O. tipulae</i>	0.130317	0.026974	0.117459021	0.035033	0.166762493	0.037731
<i>D. coronatus</i>	0.2792	0.069039	0.28664612	0.083762	0.266274558	0.065356

The whole-embryo viscosity obtained for *C. elegans* by our method appears to be ~ 0.08 Pa s, more than an order of magnitude lower than the values reported previously that were determined *in vivo* by magnetic tweezer experiments (Garzon-Coral et al., 2016; De Simone et al., 2018) and special assays that involved the injection and tracking of fluorescent nanoparticles within the embryo (Daniels et al., 2006). Motivated by the need to investigate the probable cause of this difference, we went on to check the effect of density (crowding) of granules on the obtained viscosity.

6.3.3. Viscosity corrected for density of granules

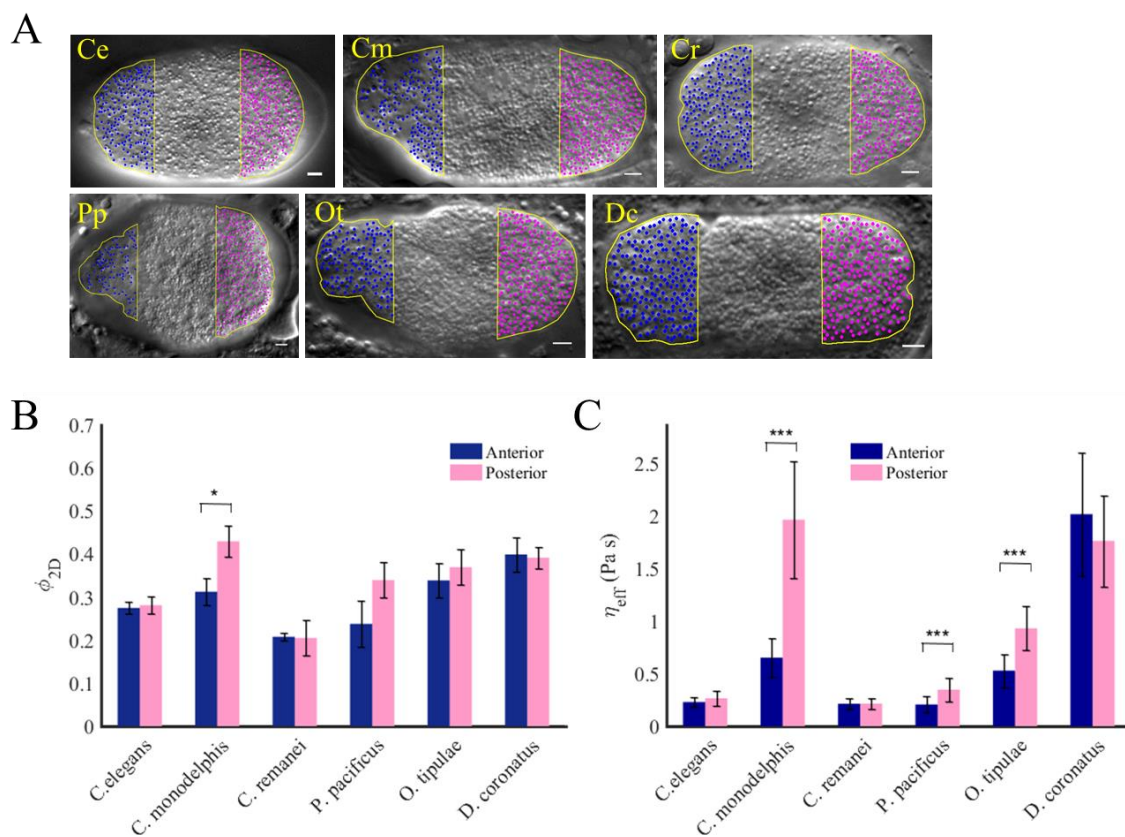


Figure 6.6. Viscosity corrected for granule crowding. (A) Density of granules in the image plane was measured manually for anterior (blue) and posterior (magenta) regions of nematode species. Scale bar 3 μm . (B) Mean granule packing fraction (ϕ_{2D}) varies across species. (C) Mean effective viscosity of the cytoplasm, inclusive of ϕ_{2D} , is estimated for the 6 species using the Quemada equation. Error bars indicate standard deviation. *, $P < 0.05$ and ***, $P < 0.001$.

The solvent phase viscosity (η_s) was corrected for the apparent density of granules in the zygote. The granule packing fraction (ϕ_{2D}) was estimated for anterior and posterior segments (Figure 6.6A, B) as well as for the whole embryo (Figure 6.7A).

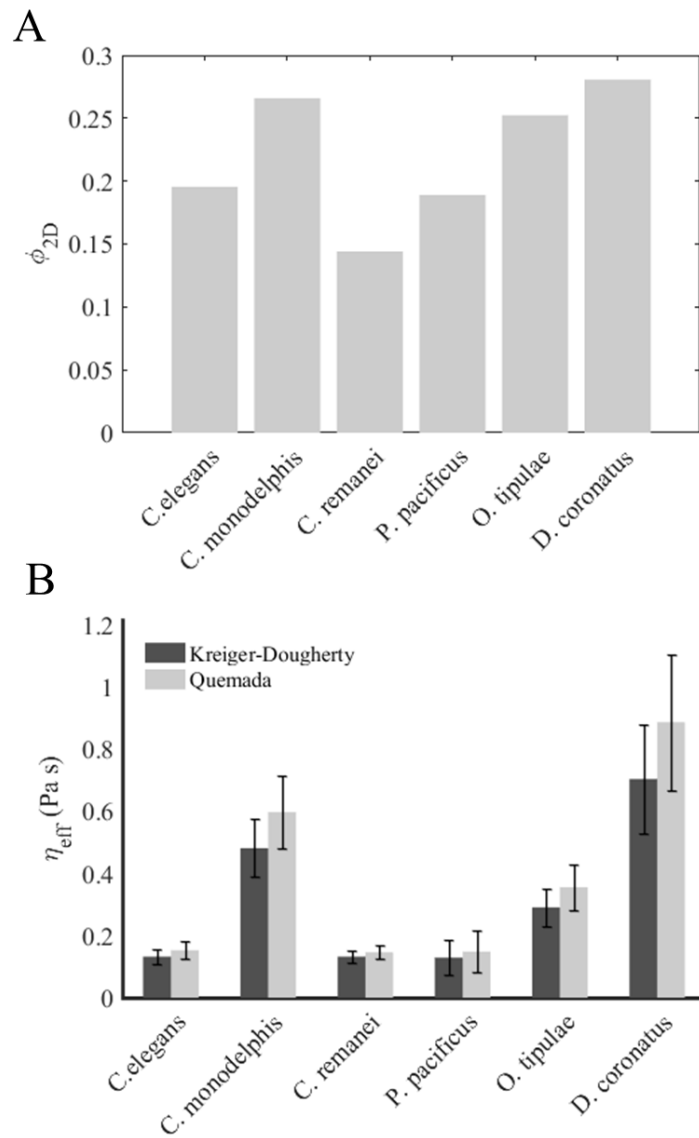


Figure 6.7. Viscosity of the whole cell. (A) Granule packing fraction values are measured manually and compared across nematode species. (B) Effective viscosity inclusive of packing fraction is calculated by Kreiger-Dougherty and Quemada equations. Error bars indicate standard deviation.

The obtained ϕ_{2D} was used to calculate the effective viscosity (η_{eff}) inclusive of granule crowding by the Quemada and Krieger-Dougherty methods (Equations 6.1 and 6.2) (Figure 6.6C, 6.7B).

Table 6.2. Viscosities (Pa s) inclusive of granule packing fraction (η_{eff} - Quemada) are compared across species and summarized below.

Species	Whole embryo		Anterior		Posterior	
	Mean	SD	Mean	SD	Mean	SD
<i>C. elegans</i>	0.152795	0.027051	0.230985186	0.046187185	0.265695959	0.072237886
<i>C. monodelphis</i>	0.596411	0.115315	0.653166764	0.179996389	1.967997446	0.55926706
<i>C. remanei</i>	0.146358	0.021974	0.213437172	0.048097649	0.214020395	0.050390826
<i>P. pacificus</i>	0.148573	0.065697	0.20704888	0.076219154	0.34876023	0.114178659
<i>O. tipulae</i>	0.355429	0.073567	0.529565432	0.157948039	0.933640652	0.211240245
<i>D. coronatus</i>	0.88591	0.219082	2.020655473	0.590463802	1.765808435	0.433411631

To further ensure that active transport has little or no role to play in the observed pattern of granule motion, RNA interference experiments were conducted in collaboration with Delattre lab, where ATP metabolism in the single-celled *C. elegans* embryos was knocked down by two methods, (i) silencing the CYC-1 gene and (ii) the ATP-2 gene.

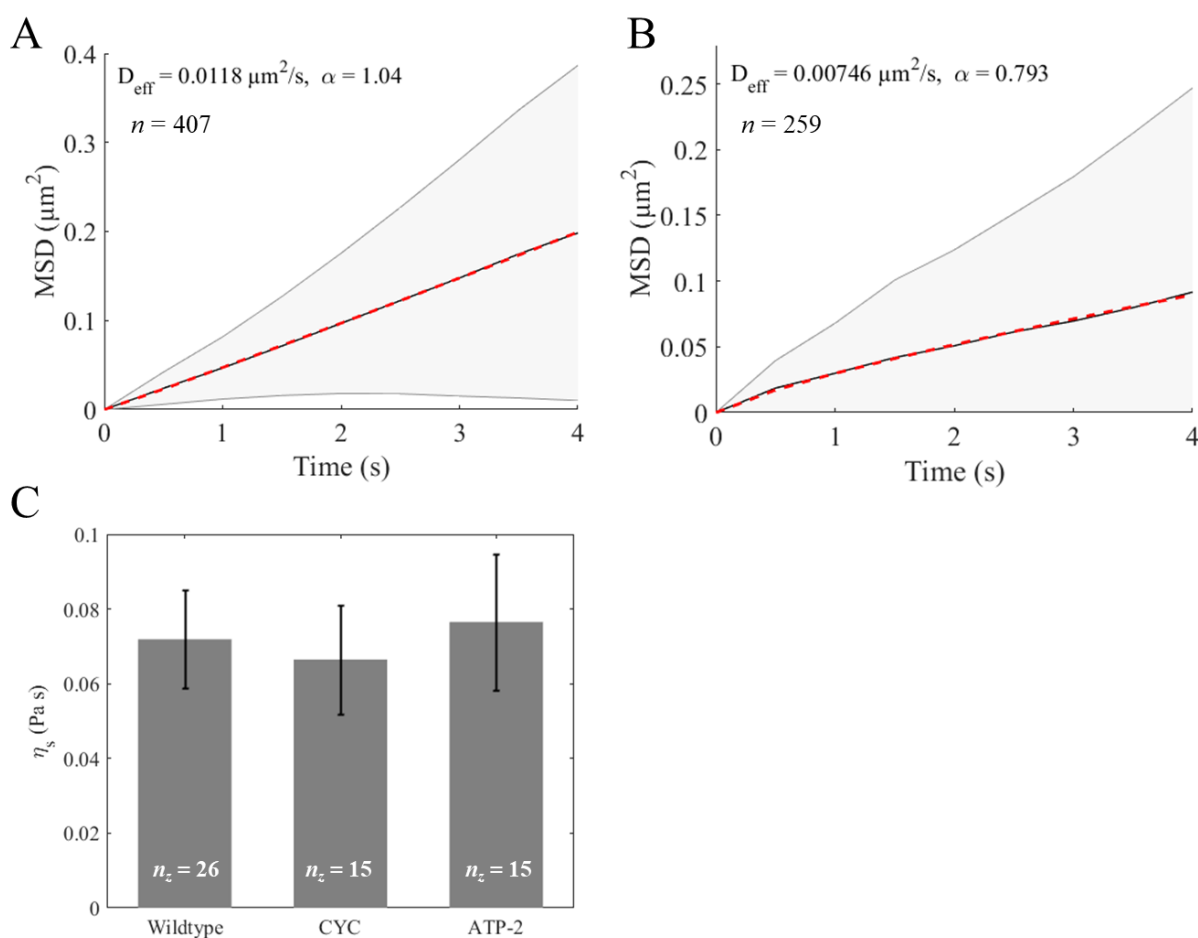


Figure 6.8. ATP inactivation does not affect granule motion. Average MSD profiles (black solid lines) were fit (red) to the anomalous diffusion model to obtain effective diffusion coefficients of (A) CYC and (B) ATP-2 knockdowns. Shaded gray region indicates standard deviation. (C) Solvent viscosities of the whole-embryo cytoplasm of wildtype *C. elegans* and RNAi-based ATP-knockdown embryos are estimated using Stokes-Einstein's equation. n_z = number of zygotes.

We find that RNAi-based silencing of CYC-1 and ATP-2 genes did not affect the effective diffusion coefficient of the granules and in turn the viscosity of the cytoplasm in the cells (Figure 6.8A, B). The viscosity of cytoplasm of wildtype zygotes was found to be comparable to the ATP knockdown variants (Figure 6.8C).

6.4. Discussion

In a pioneering attempt to determine the cytoplasmic viscosity of nematode zygotes by a non-invasive method, we used yolk granules innately present in the cells as probes. Six evolutionarily related species of nematodes were analysed, including the model organism *Caenorhabditis elegans* along with *Caenorhabditis monodelphis*, *Caenorhabditis remanei*, *Pristionchus pacificus*, *Oscheius tipulae* and *Diploscapter coronatus*. The zygotes were imaged by label-free DIC microscopy and the movement of granules was tracked in time using DICOT. Using their MSD profiles, the effective diffusion coefficient of granules was estimated. The viscosity of the cytoplasm containing these granules was then estimated by Stokes-Einstein relation that relates the effective diffusion coefficient to viscosity.

Our estimate of effective cytoplasmic viscosity of *C. elegans* zygotes is ~ 0.15 Pa s, about 150 times the viscosity of water (0.001 Pa s). This value obtained for *C. elegans*, however, is 10 folds lower than the values reported previously (Daniels et al., 2006). In addition to the fact that our measurements are obtained by a non-invasive method in unperturbed cells, there are a few possible explanations for this deviation.

- (a) The D_{eff} estimated in the report by Daniels et al. is measured from MSD profiles of ~ 1 s timescales. Our values are taken from longer curves that are fit for at least 4 s. Movement driven by active transport can show time-dependent differences, so we tested the effect of using a shorter time-interval of 1 s (comparable to Daniels et al., 2006), to examine if our estimates change. We find in our study that the D_{eff} from 1 s and 4 s fits are the same ($\sim 8 \times 10^{-3} \text{ um}^2/\text{s}$).

- (b) Daniels et al. have pooled data from multiple cell cycle stages as opposed to our estimates of viscosity that are taken only from zygotes imaged in the pro-metaphase (and away from the central plane of the zygote), where the motion of spindles is thought to affect the diffusion of granules in the least. Having a representative time-series from all stages systematically could be used to explain the discrepancy between our data and theirs.
- (c) The differences in our sampling time (500 ms) versus theirs (33 ms) may also be one of the possible reasons for the deviation in MSD measurements. However, the interval of 500 ms was found suitable when used to image 1 μm -diameter control beads suspended in water and glycerol using the same microscopy set up, as it gave viscosities of these solvents comparable with published literature.
- (d) The viscosity estimated by (Garzon-Coral et al., 2016; De Simone et al., 2018) is 0.6 Pa s, a value that also seems to vary from the viscosity reported by (Daniels et al., 2006) and appears 4 times higher than the viscosity estimated in our study.

We report that the cytoplasmic viscosities of the zygotes of the given 6 species of nematodes vary from each other. While *C. elegans*, *C. remanei* and *P. pacificus* show comparable whole-embryo viscosities, *O. tipulae*, *D. coronatus* and *C. monodelphis* show significantly higher viscosities. Recoil velocities measured post laser ablation of the spindle (courtesy, Delattre lab, ENS, Lyon) corroborate with our viscosity estimation results. While spindle recoil velocities were found to be comparable for *C. elegans*, *C. remanei* and *P. pacificus* species, the least velocities were recorded for *D. coronatus* and *C. monodelphis*.

Zygotes of less-studied nematode species, including those other than the *Caenorhabditis* species could be analysed by this method, irrespective of the degree of their amenability to genetic and physical manipulation.

6.5. Conclusion

Our non-invasive, label-free method for estimation of viscosity of the cytoplasm of nematode zygotes using yolk granules as endogenous probes paves way for understanding the variability that has emerged during the course of evolution, in the biophysical properties of cells and molecular assemblies such as the mitotic spindle.

Chapter 7

Dynamic Instability and Sliding of ParM Filaments: Implications for Plasmid Segregation

Overview

Having discussed eukaryotic spindles in Chapter 6, we now focus on the mechanics of a minimal, plasmid-segregating spindle formed by the ParMRC system in *E. coli*. In this chapter, in order to determine the effect of dynamic instability of ParM filaments on the assembly of the ParM spindle, we perform Brownian dynamics based simulations to reconstitute the assembly of half-spindles. Further, we quantify for the first time to our knowledge, the sliding of ParM filaments from *in vitro* imaging data using quantitative kymography and diffusion analysis. To this end, we employ AMTraK (described in Chapter 3), an automated kymography tool implemented in MATLAB, that generates and processes kymographs.

7.1. Introduction

The segregation of low copy R1 plasmids during cell division in *E. coli* is brought about by a transient, minimal spindle formed by the ParMRC system (Moller-Jensen et al., 2002, 2003). The *par* operon (Gerdes and Molin, 1986) encodes three spindle components- ParM (motor), ParR (repressor) and *parC* (centromere). ParM is a filamentous actin-like polymer (Ent et al., 2002) that generates force by ATP-dependent polymerization. In their free state, ParM filaments show identical kinetics of polymerization and depolymerization at both ends. *parC* is a *cis*-acting centromere-like sequence on the plasmid. ParR is an adaptor protein that binds to ParM as well as to *parC*. Dimers of ParR bind to the *parC* sequence forming a ParRC complex on the plasmid. In the ‘search and capture’ model of spindle assembly (Figure 7.1A), ParM filaments search cellular space and capture plasmid targets at the ParRC complex. Structural analysis of ParM filaments has shown that only the barbed (plus) end of a ParM filament is structurally capable of binding to a ParRC complex. The binding of plus ends with ParRC complexes results in the formation of a tripartite complex that we refer to as a ‘half-spindle’. In the ‘on-site nucleation’ model of ParMRC spindle assembly (Figure 7.1B) half-spindles are formed when a ParM filament is nucleated on the plasmid at the ParRC site

itself. At least two such half-spindles assemble in an antiparallel orientation to form a complete bipolar spindle (Figure 7.1A,B) (Gayathri et al., 2012).

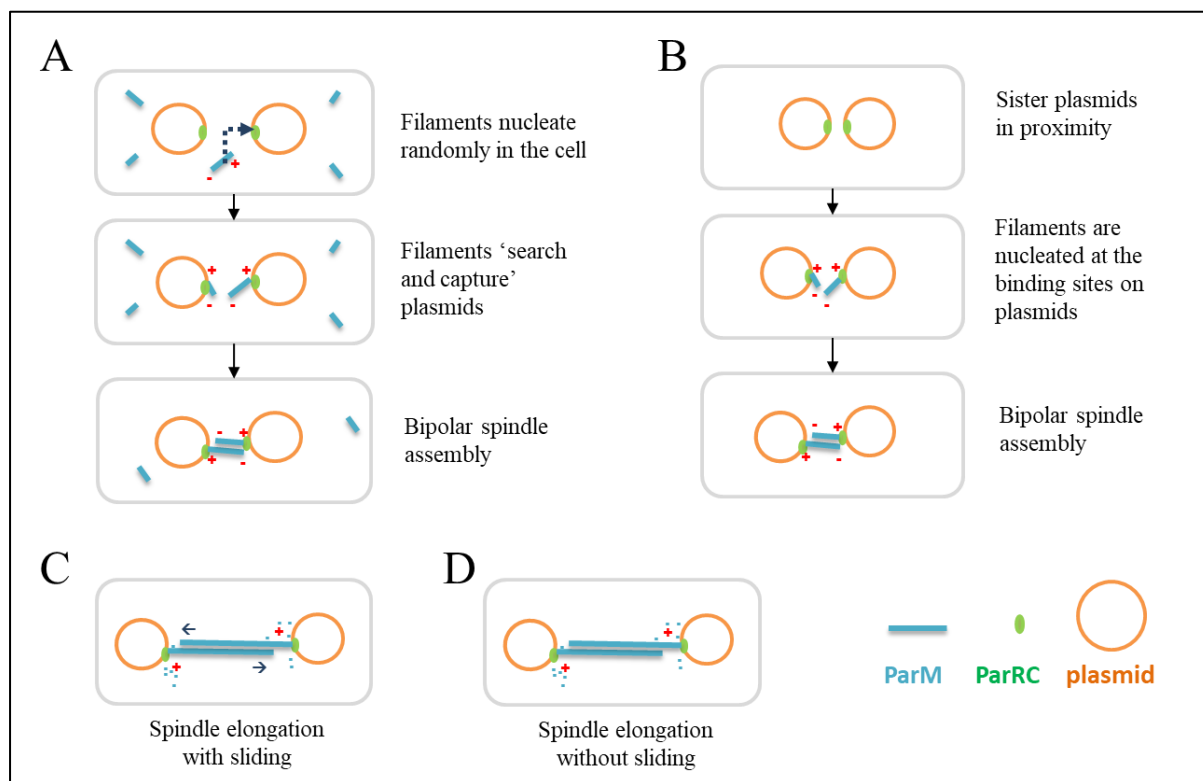


Figure 7.1. Models of ParMRC spindle assembly and action. ParM filaments are shown as blue rods, plasmids are shown as orange circles and ParRC complexes are shown green dots. Plus and minus ends of ParM filaments are marked by red + and – signs respectively. (A) *The 'search and capture' model of spindle assembly:* ParM filaments are randomly nucleated in the cell. Filaments 'search and capture' plasmids at the ParRC sites to form a half-spindle. Two half-spindles encounter each other to assemble the complete spindle. (B) *The on-site nucleation model of spindle assembly:* ParM filaments are nucleated at ParRC sites of plasmids to form half-spindles. Two half-spindles encounter each other to assemble the complete spindle. (C) Once the entire spindle is assembled, the coupled filaments elongate by insertional polymerization of ParM monomers (blue dots) at the bound ends to push the plasmids to opposite cell poles. Filaments in a pair also slide in a contractile manner, the direction of sliding is marked by arrows. (D) The assembled spindle elongates by insertional polymerization in the absence of filament sliding.

Properties of the cytomotive elements of a spindle are thought to bring about spindle formation and movement of DNA. In the following section, I shall briefly review two interesting properties of ParM filaments – dynamic instability and sliding - that are hypothesized to drive the ParMRC spindle assembly and plasmid segregation.

Dynamic instability of ParM filaments

Dynamic instability is the ability of filaments to alternate between phases of growth and rapid shrinkage. The transition of a filament from growing stage to shrinkage is termed as a ‘catastrophe’ and the transition of a shrinking filament to growth is termed as a ‘rescue’. Similar to microtubules in eukaryotes, ParM has been shown to display dynamic instability (Garner et al., 2004). However, while ParM filaments are observed to undergo catastrophic events, no rescues have been observed in them. Given that the reported velocity of shrinkage is much greater than the velocity of growth (Garner et al., 2004; Gayathri et al., 2012) (Figure 7.4A), the onset of catastrophe in a filament results in its complete destruction.

The discovery of catastrophic events in ParM filaments led to the question, how does dynamic instability contribute to ParMRC spindle assembly and segregation? *In vitro* reconstitution experiments have shown that the dynamic instability of ParM enables easy turnover of filaments, and provides excess monomer to drive the elongation of the spindle (Garner et al., 2007). Further, it is hypothesized that the dynamic instability of ParM filaments may aid the ‘search and capture’ of plasmid DNA in prokaryotes (Garner et al., 2007), similar to eukaryotic cells, where the dynamic instability of microtubules is shown to allow the efficient search of cellular space and capture of chromosomes prior to segregation (Holy and Leibler, 1994) (see Chapter 1).

In an *E. coli* cell, two distinct kinds of ‘search and capture’ events involving ParM filaments may be necessary for the complete spindle to assemble (Figure 7.1A). The first type involves the capture of a plasmid by a single filament at the ParRC complex to form a half-spindle. At least two such half-spindles are required for the formation of the entire bipolar spindle. The second type of ‘search and capture’ event takes when the two half-spindles associate by their ParM filaments to form a complete spindle. The precise role of dynamic instability in both the kinds of ‘search and capture’ events still remains a puzzle. In this study, we simulate the first type of ‘search and capture’ process with the aim to determine whether dynamic instability increases the efficiency of capture of a plasmid by a filament, in a cell as small as *E. coli*. We use plasmid capture time as a measure of the efficiency of capture and compare the efficiency of dynamic filaments and fixed-length filaments in capturing plasmid targets.

Sliding and bundling of ParM filaments in vitro

In recent work, ParM filaments were reported to bundle and undergo sliding *in vitro* (Gayathri et al., 2012) (Figure 7.2) in the presence of a very low concentration of a crowding

agent. Sliding in a pair of filaments of comparable length is observed to be contractile in nature, proceeding in a thermodynamically favourable direction that maximizes the overlap between them. Interestingly, unlike eukaryotic actin and microtubule filaments, ParM filaments do not require the presence of additional proteins or molecular motors in order to initiate or continue sliding. As sliding could occur in the presence of ATP as well as a non-hydrolysable analogue (AMPPNP), hydrolysis of ATP is shown to not be required for the process. It has been established that a sequence of 4 amino acid residues on the interface of the two filaments are essential for sliding (Gayathri et al., 2012). In previous work in eukaryotes, motor-assisted sliding of microtubules in eukaryotic spindles has been speculated to facilitate spindle assembly and maintain spindle length (Burbank et al., 2007; Loughlin et al., 2010; Goshima and Scholey, 2010). While the potential role of ParM filaments in spindle formation and mechanism of action is not yet known, it is hypothesized that during elongation of a bipolar spindle (Figure 7.1C,D), the free ends of the filaments may be stabilized by pairing (bundling) and hence protected from catastrophe (Gayathri et al., 2012).

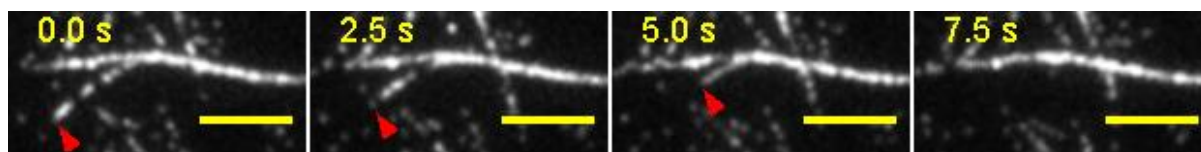


Figure 7.2. Sliding in ParM filaments. Speckle labelled Alexa-568 ParM filaments showing sliding in the presence of AMPPNP were observed by TIRF microscopy. One filament is seen to slide on another filament that appears static. Red arrowheads indicate the distal tip of the sliding filament. Time is indicated in seconds. Scale bar - 4 μm .

On the assembly of the complete spindle, insertional polymerization of ParM at the bound ends is reported to drive the process of pushing the plasmids to opposite cell poles. How dynamic instability, insertional polymerization and inter-filament interactions together bring about the process of plasmid segregation in an *E. coli* cell in a span of a few minutes still remains poorly understood. In an *E. coli* cell, the direct observation of the interactions of spindle components is hindered greatly due to the diffraction limit of light (~ 250 nm). Also, it is established that the ParMRC spindle is a minimal machinery that requires only three well-studied components to bring about plasmid segregation. Given these two facts, the use of computer simulations is most suited to investigate the collective behavior of this system and identify the potential roles of ParM dynamic instability and filament sliding in spindle

assembly and plasmid segregation. However, simulations of the sliding process are currently hindered by the lack of quantitative information on ParM filament sliding.

In this chapter, in order to determine the effect of dynamic instability on the assembly of the ParM spindle, we perform Brownian dynamics based simulations to reconstitute the assembly of half-spindles. Further, we quantify for the first time to our knowledge, the sliding of ParM filaments from *in vitro* imaging data using quantitative kymography and diffusion analysis. To this end, we employ AMTraK (Chaphalkar et al., 2016) (described in Chapter 3), an automated kymography tool implemented in MATLAB, that generates and processes kymographs.

7.2. Materials and Methods

7.2.1. Computer simulations

All the simulations were performed in 3D using Cytosim (Nedelec and Foethke, 2007), an agent-based Brownian simulator. Values of parameters used in the simulations were set either based on published experimental measures or were varied across a physiologically relevant range (Table 7.1). All the molecular events (polymerization, depolymerisation, binding, unbinding etc.) are simulated to occur with a constant probability inside an *E. coli* cell. The steric interaction between objects was set to 0 unless otherwise mentioned.

Cell system

An *E. coli* cell is modelled as an elongated spherocylinder of length 2.8 μm with hemispherical caps of radius 0.4 μm at both ends (Bakshi et al., 2012; Reshes et al., 2008) (Figure 7.3). The viscosity of the cytoplasm is taken as 9.75 cP (Mullineaux et al., 2006). The cell geometry does not undergo any change in time.

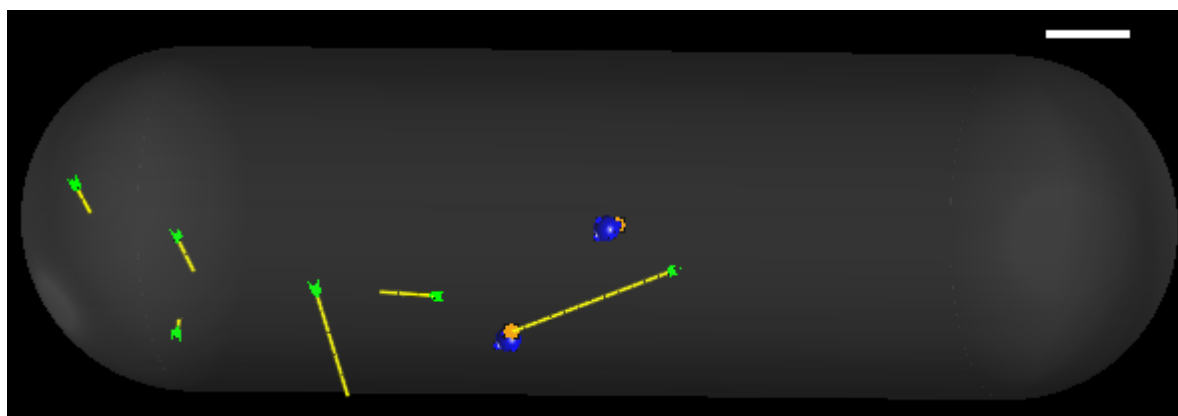


Figure 7.3. A still image from the Cytosim simulation. Dynamic ParM filaments (yellow lines) diffuse within an *E. coli* cell (grey boundary) and capture *par+* plasmids (blue spheres). Plasmids bind to filaments at the ParRC site (orange). Green chevrons depict the free minus ends of the filaments. Scale bar – 0.2 μm .

Plasmids

In our model we assume that plasmids are in their post-replication phase, so the number of plasmids in the cell remains unchanged during the simulation. Plasmids are initialized at the cell centre in the beginning of the simulation (Jensen and Gerdes, 1999). The number of plasmids in a cell varies in the range 1-2, depending on the simulation performed. Each plasmid is modelled as a sphere carrying one ParM-binding site on the surface representing a ParRC complex. The plasmid radius is chosen to be 30 nm, an approximation based on the radius of gyration (R_G) of circular DNA that can be calculated using the following equation (Araki et al., 2006):

$$\langle R_G^2 \rangle = b^2 N / 12 \quad (\text{Equation 7.1})$$

Here, b is the Kuhn length of DNA (0.34 nm), N is the number of base pairs in the *par*⁺ plasmid (R1 plasmid - 10^5 bp).

The local effective viscosity around free plasmids was modulated such that the resulting effective diffusion coefficient of plasmids matched the reported value ($5 \cdot 10^{-5} \mu\text{m}^2/\text{s}$) measured *in vivo* (Campbell and Mullins, 2007).

Filaments

ParM filaments were modelled as discrete polymers with rigidity $0.073 \text{ pN } \mu\text{m}^2$, equal to that of actin (Gittes et al., 1993). The filaments are kinetically identical and display dynamic instability (Garner et al., 2004) at both ends, unless bound to a plasmid. The dynamic instability of filaments was modelled using the standard 2-state 4-parameter model described for microtubules (Verde et al., 1992). The velocity of growth (v_g) and shrinkage (v_s) of filaments were taken from two different reports (Garner et al., 2004; Gayathri et al., 2012) (Figure 7.4A). In both cases, v_g was lower than v_s . The frequency of catastrophe (f_{cat}) was calculated using the length versus time information obtained by digitizing a graph from (Garner et al., 2004) (Figure 7.4B). The reciprocal of average time taken for catastrophe (t_{cat}) was taken as the frequency of catastrophe.

$$\langle f_{cat} \rangle = 1 / \langle t_{cat} \rangle \quad (\text{Equation 7.2})$$

We take the growing force (F_g) of ParM to be 1 pN, equal to experimentally measured values for actin (Footer et al., 2007). In our simulations, v_g depends on F_g such that:

$$v = v_g * e^{-F/F_g} \quad (\text{Equation 7.3})$$

As rescue events were not observed in experiments, we set the frequency of rescue of both ends of a filament to 0. Thus the commencement of a catastrophic event leads to complete destruction of a filament. In order to keep filament number constant in some simulations, if destroyed, filaments were allowed to re-nucleate elsewhere in the cell.

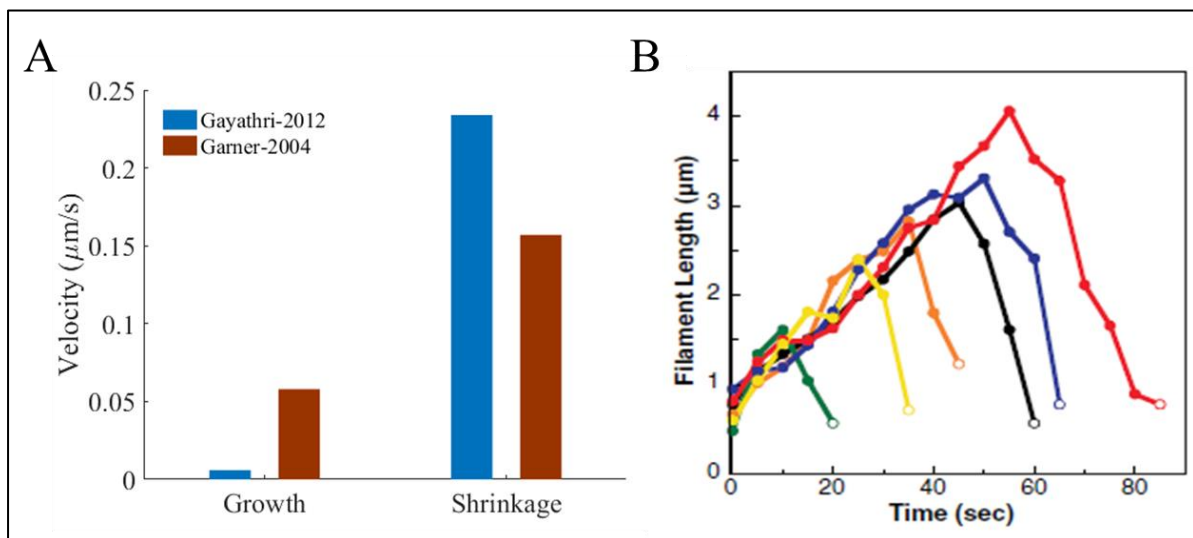


Figure 7.4. Dynamic instability parameters of ParM filaments. ParM filaments were modelled as dynamic filaments using the standard 4-parameter model. (A) Velocities of growth and shrinkage were taken from (Garner et al., 2004; Gayathri et al., 2012). (B) Frequency of catastrophe was calculated using the average time taken for a catastrophic event from this graph reproduced from (Garner et al., 2004).

According to the ‘search and capture’ model (Figure 7.1A), filaments were allowed to nucleate randomly within the cell, diffuse in cellular space and capture plasmid targets at the binding site. A filament can bind to a plasmid by only the barbed (plus) end which gets protected from catastrophe and shows increased velocity of growth post binding (Gayathri et al., 2012). Binding happens at the chosen binding rate when the plus tip of a diffusing filament lies within 10 nm of a plasmid. Only one filament can bind to a plasmid at a time. Once bound to the plus end of a filament, plasmids do not detach.

Table 7.1. Simulation parameters

Parameter	Abbreviation	Value/Attribute	Units	Reference
Simulation Space Parameters				
E. coli cap radius	r	0.4	μm	(Bakshi et al., 2012)
E. coli total length	l	2.8	μm	(Bakshi et al., 2012),(Reshes et al., 2008)
Viscosity	η	0.00975	Pa s	(Mullineaux et al., 2006)
Thermal energy (at 37°C)	$k_B T$	$4.28 * 10^{-21}$	N m	(Rob Phillips et al., 2012)
Boundary		Stiff		This study
Time of simulation	t	10	min	This study
Cytoskeletal Parameters				
Velocity of growth	v_g – bound end	0.022	$\mu\text{m s}^{-1}$	(Gayathri et al., 2012)
	v_g – unbound end	0.006	$\mu\text{m s}^{-1}$	(Gayathri et al., 2012)
		0.058		(Garner et al., 2004)
Velocity of shrinkage	v_s – bound end	0	$\mu\text{m s}^{-1}$	(Gayathri et al., 2012)
	v_s – unbound end	-0.234	$\mu\text{m s}^{-1}$	(Gayathri et al., 2012)
		0.157		(Garner et al., 2004)
Frequency of catastrophe	f_{cat} – bound end	0	s^{-1}	(Garner et al., 2004)
	f_{cat} – unbound end	0.0383	s^{-1}	(Garner et al., 2004)
Frequency of rescue	f_{res} – bound end	0	s^{-1}	(Garner et al., 2004)
	f_{res} – unbound end	0	s^{-1}	(Garner et al., 2004)
Distance between two points of a filament	d_f	0.05	-	This study
Initial length	-	0.01	μm	(Garner et al., 2004)
Polymer dynamics model	-	Two-state 4-parameter model	-	This study
Minimal length of the filament	-	0.01	μm	This study
Fate of filaments that reduce to length minimal length	-	Destroy	-	This study

Rigidity	κ	0.073	$\text{pN s } \mu\text{m}^{-2}$	Taken from values reported for actin (Gittes et al., 1993)
Growing force	F_g	1	pN	(Footer et al., 2007)
Steric interaction	-	0		This study
<i>Plasmid Parameters</i>				
Effective diffusion coefficient	D_{eff}	0.00005	$\mu\text{m}^2/\text{s}$	(Campbell and Mullins, 2007)
No. of plasmids	n_p	1 or 2	-	This study
No. of binding sites	n_{bs}	1	-	(Gayathri et al., 2012)
<i>Binding-site Parameters</i>				
Filament binding rate	-	500	/s	This study
Filament unbinding rate	-	0	/s	This study
Filament binding range	ϕ	10	nm	This study
End of filament bound	-	Plus	-	(Gayathri et al., 2012)
No of filaments per binding site	n_f	1	-	(Gayathri et al., 2012)

7.2.2. Microscopy, image pre-processing and analysis

The experimental work on ParM was performed by Gayathri Pananghat in the lab of Dr. Jan Lowe, MRC Lab, Cambridge. ParM filaments were assembled *in vitro* with a mixture of Alexa-568 labelled and unlabelled monomers, in the presence of ATP or AMPPNP and 1% methyl cellulose, were imaged by TIRF microscopy as described in (Gayathri et al., 2012). The image time-series were pre-processed by enhancing contrast, smoothing using a 3 x 3 mean filter and adjustment of brightness and contrast in ImageJ (Schneider et al., 2012).

Angle of contact measurement

Angles of contact formed by filaments prior to sliding were measured by image analysis using a custom MATLAB code. Filament ends and the point of contact were manually selected on the image. The smallest angle made at the point of contact was measured.

Quantitative kymography for sliding and diffusion analysis

Analysis of filament sliding and diffusion was performed by quantitative kymography using a MATLAB based tool named AMTraK (Chaphalkar et al., 2016). Spatiotemporal coordinates of filaments obtained from kymography were used to estimate the 1D diffusion coefficient

and anomaly parameter as described in Chapter 2. The cumulative displacement of the sliding filament was obtained by summing the instantaneous displacement in time. Instantaneous displacement in the direction of translocation of the filament was considered positive, while that against the direction of translocation of the filament was considered negative. The cumulative displacement was fit to the logistic function:

$$d_t = (k * d_0) / [d_0 + [(k - d_0) * e^{-rt}] \quad (\text{Equation 7.4})$$

Where k is the maximal displacement, r is the sliding rate, d_0 is the initial displacement and d_t is the displacement at time t . Phases in the displacement curve were identified comparing the slope of the curve (m) to the sliding rate (r). Based on transitions in the slope, three phases were identified analogous to a growth curve: lag (approach: $m < r$), log (sliding $m \sim r$) and stationary (paired $m < r$).

Persistence length measurement

Persistence lengths of individual and bundled ParM filaments were estimated from electron microscopy and fluorescence microscopy images respectively using FiberApp (Usov and Mezzenga, 2015) by manually tracing contours of filaments. The contour data was analysed using two alternate methods to estimate the persistence length (λ) in 2D, (a) the angle correlation method and (b) mean squared end-to-end distance (MSED) method. Angle correlation is measured as cosine of θ , the angle between tangents of any pair of segments along a contour of length l .

$$\langle \cos \theta \rangle = e^{-l/2\lambda} \quad (\text{Equation 7.5})$$

MSED is expressed by the equation:

$$\langle R^2 \rangle = 4\lambda [l - 2\lambda (1 - e^{-l/2\lambda})] \quad (\text{Equation 7.6})$$

Here, R is the direct end-to-end distance between any pair of segments along a contour of length l .

7.2.3. Data analysis

All data analysis and plotting was performed using MATLAB 2014b and 2016a (MathWorks Inc., USA). Fitting of custom functions was performed using either the Levenberg-Marquardt

non-linear least square routine or the trust-region method, implemented in the Curve-Fitting toolbox (ver. 3.5) of MATLAB.

7.3. Results

This section is divided into two parts-

- (1) Simulation of ParM spindle assembly and
- (2) Quantitative image analysis of ParM filament sliding.

7.3.1. Simulation of ParM spindle assembly

We reconstitute components of the ParMRC spindle machinery within an *E. coli* cell *in silico* in a coarse-grained model where filaments and plasmids are represented by rods and spheres respectively. While the filaments diffuse with an effective diffusion coefficient (given by their length) implicitly calculated by Cytosim, plasmids can be assigned an effective diffusion coefficient by modulating their local viscous drag. The parameters used for simulations are summarized in Table 7.1. Details of the system components modelled in the simulation are given in Section 7.2.1.

In an attempt to simplify our simulations, we consider that plasmids have replicated beforehand and also that the boundary of the cell does not grow within the simulation time span. We analyse the collective behaviour of the spindle components for 10 minutes, a period two fold greater than the reported time of plasmid segregation (Campbell and Mullins, 2007) and approximately half the time of the cell cycle for a fast growing *E. coli* cell.

Plasmids do not translocate to the poles by diffusion alone

It is known that high copy number plasmids of low molecular weight are partitioned randomly by diffusion into two daughter cells (Reyes-Lamothe et al., 2014; Ghosh et al., 2006; Ebersbach and Gerdes, 2005). However, high molecular weight, low copy number plasmids in *E. coli* cells are observed to require additional segregation mechanisms including the recruitment of a dedicated segregation machinery (Nordstrom and Austin, 1989; Ghosh et al., 2006; Ebersbach and Gerdes, 2005) to ensure that each daughter cell inherits at least a single copy of the plasmid. When reconstituting *par+* plasmids in simulation, the first question we asked was, is plain diffusion sufficient for segregation of R1, a 100 kb sized plasmid? We modelled R1 as spheres of 30 nm radius and effective diffusion coefficient of $5 \cdot 10^{-5} \mu\text{m}^2/\text{s}$ (Campbell and Mullins, 2007). In the beginning of the simulation, they were

initiated at the cell centre and were allowed to diffuse within the cell without steric hindrance for 10 min. We find that plasmids moving at such low diffusion coefficients do not translocate from the centre to the poles by themselves (Figure 7.5). The *in vivo* D_{eff} was measured using a mini plasmid of 30 kb in size carrying the *par+* operon (Campbell and Mullins, 2007). If plasmids $1/3^{\text{rd}}$ the size of R1 do not get segregated to the poles by diffusion alone, we suspect there is little chance that 100 kb R1 plasmids will be able to do so. This result indirectly supports the experimental results that such plasmids require dedicated mechanisms for segregation in addition to diffusion.

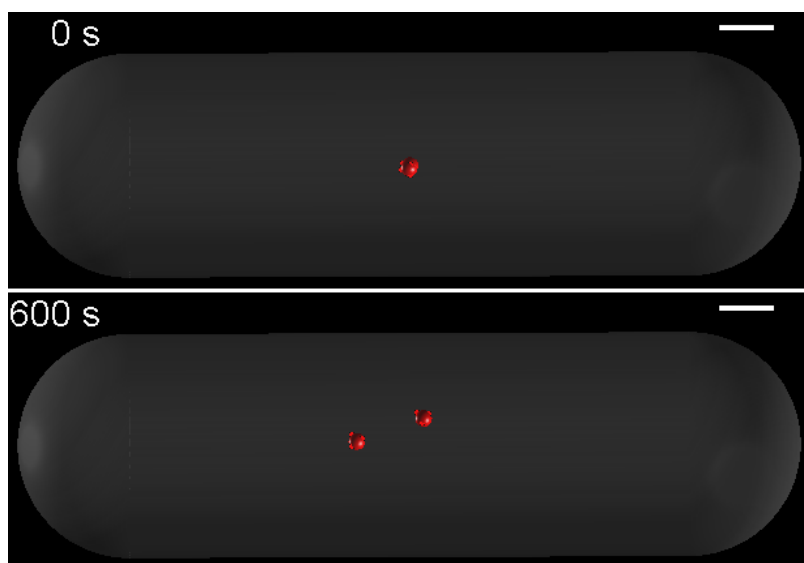


Figure 7.5. Plasmids do not translocate to poles by diffusion alone. par^+ plasmids (red spheres) were initialized in the centre of cell (upper panel) and allowed to diffuse with the given D_{eff} for 10 min. Plasmids appear to be unable to reach the poles by plain diffusion (lower panel).

Dynamic instability of ParM does not affect plasmid capture time in E. coli cells

The dynamic instability of filaments was modelled using the standard 2-state-4-parameter model described for microtubules (Verde et al., 1992). The velocity of growth (v_g) and shrinkage (v_s) of filaments were taken from two different reports (Garner et al., 2004; Gayathri et al., 2012). The image-based measures in both the reports differ possibly due to the fact that in the decade that separates the two observations, microscopy has improved greatly in terms of technology and resolution.

As a first step, the average lifetimes of simulated filaments were estimated. Using parameter values from (Garner et al., 2004), the average lifetime was calculated to be 24 s. Using values reported in (Gayathri et al., 2012), the average lifetime turned out to be 14.3 s.

Thus, the average lifetime of simulated filaments matched the lifetime of filaments measured *in vitro* (~20 s, (Garner et al., 2007)) (Figure 7.6A). We then measured the maximal length a dynamic ParM filament can achieve, i.e. the length prior to catastrophe. The average maximal lengths obtained by using values from (Gayathri et al., 2012) and (Garner et al., 2004) were 1.25 μm and 8 μm respectively (Figure 7.6B). As the maximal length determined using parameters from (Gayathri et al., 2012) was comparable to the average length of a spindle observed within an *E. coli* cell, we chose to use the former that set of v_g and v_s values in all the further simulations.

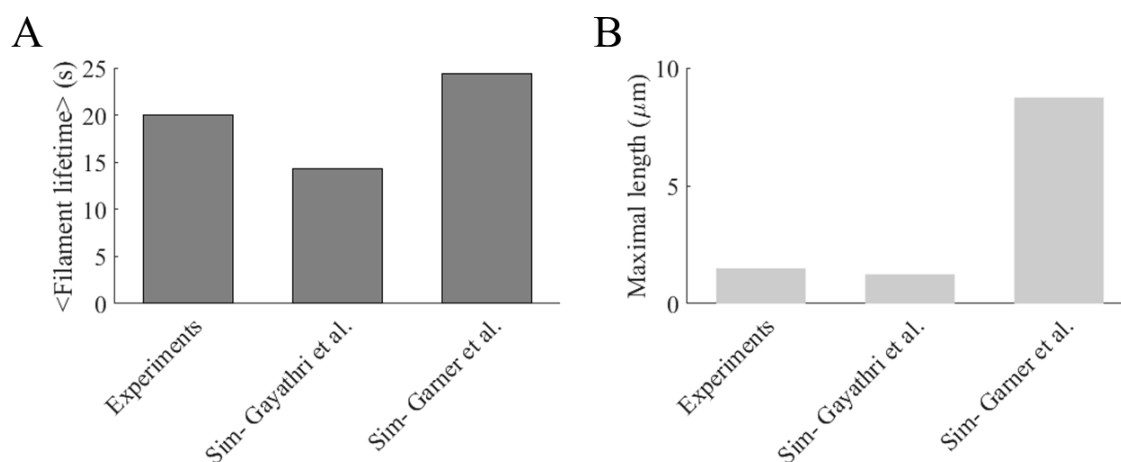


Figure 7.6. Lifetimes and maximal lengths of dynamic ParM filaments. Using v_g and v_s values from (Gayathri et al., 2012; Garner et al., 2004), the (A) average lifetimes and (B) maximal length (prior to catastrophe) of simulated filaments ($n = 1000$) were estimated and compared to reported experimental observations.

We now investigate the effect of dynamic instability on capture of plasmids by filaments. Dynamic filaments (of initial length 10 nm) and fixed-length filaments (of lengths 10 nm, 100 nm and 500 nm) were simulated. The ratio of number of filaments to number of plasmids (FP ratio) was varied. We measured the efficiency of capture in terms of two parameters. One is the average time taken for a plasmid to get captured for the first time. Second is the fraction of successful capture events. We report that in *E. coli* cells, dynamic instability does not alter the time required for a ParM filament to capture a plasmid target (Figure 7.7A). The capture time also did not appear to depend on the number of filaments available per plasmid for binding. The fraction of successful capture events, however, appeared to be proportional to the number of filaments available for binding, but did not seem to be affected by dynamic instability of the filaments (Figure 7.7B).

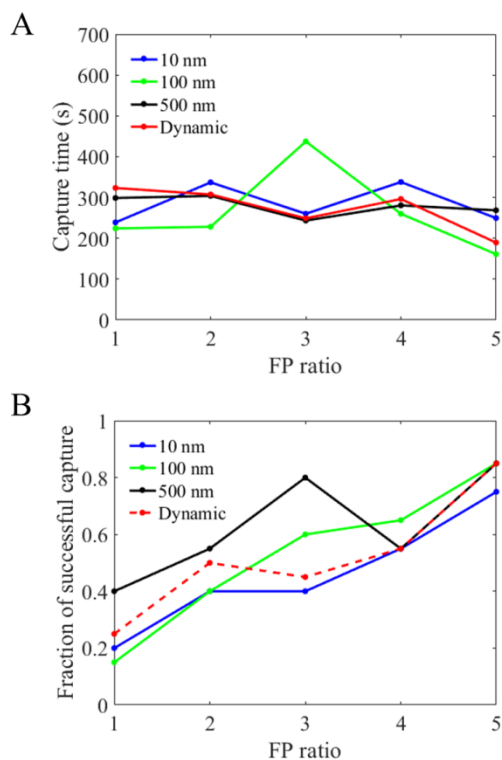


Figure 7.7. Effect of dynamic instability on plasmid capture in simulation. (A) Plasmid capture time and (B) the fraction of successful capture events are measured across an increasing ratio of number of filaments to number of plasmids (FP ratio). The filaments are either dynamic or fixed-length filaments of different lengths. 20 runs of the simulation were performed for each kind of filament.

Filaments bound to plasmids show slightly increased lifetimes

It is observed that once a plasmid is captured by a ParM filament, the bound end is stabilized by ParRC complexes (Schumacher et al., 2007; Moller-Jensen et al., 2007), thereby preventing it from catastrophe and increasing the rate of polymerization of the filament at that end (plus end) (Gayathri et al., 2012). Let us assume that a filament polymerizing at 22 nm/s at the plus end displaces a bound plasmid at the same speed. Theoretically, it would take ~34 s for the filament to push the plasmid from the centre to the poles i.e. over a distance of $1/4^{\text{th}}$ cell length ($\sim 0.75 \mu\text{m}$). If a single filament bound to a plasmid target is capable of transporting the plasmid over the required distance within a short time, is the pairing of two antiparallel half-spindles essential? Since one end of a filament in a half-spindle is free and prone to catastrophe, we speculate that the potential answer to this question may lie in the time for which a dynamic filament bound to a plasmid survives in the absence of rescue events.

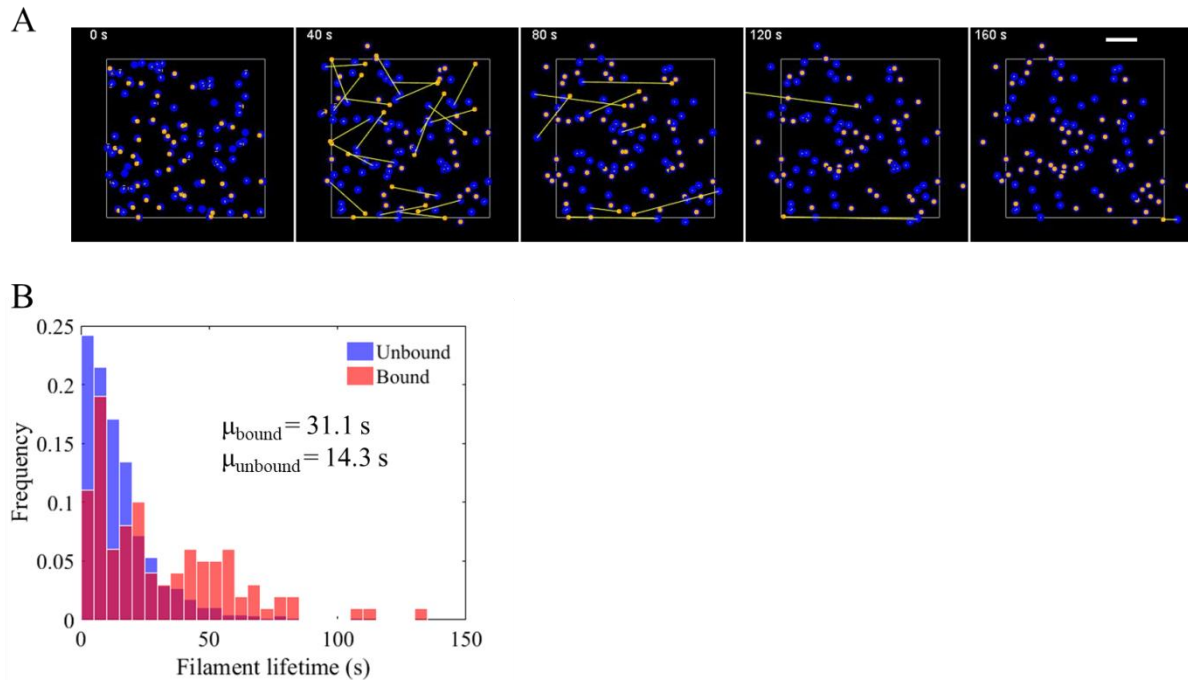


Figure 7.8. Binding increases lifetime of dynamic filaments. (A) Montage of a simulation of dynamic filaments (yellow) bound to ParRC complexes (orange dots) on plasmids (blue circles, $n = 100$). Scale bar - $0.2 \mu\text{m}$. (B) The average lifetimes of bound and unbound filaments are compared.

We calculated the lifetime of filaments when bound to plasmids. We find that in simulation, the filaments bound to plasmids show increased lifetimes i. e. 31.1 s (Figure 7.8A,B). However, this lifetime is still not sufficient for the filament to complete the segregation by itself as the process is estimated to take $\sim 3\text{-}4$ minutes *in vivo* (Campbell and Mullins, 2007).

The finding that bound filaments have shorter lifetimes than $3\text{-}4$ minutes inspite of stabilization by plasmids at one end suggests that other mechanisms may be employed *in vivo* to stabilize the free end of a filament, so that it can last till the entire segregation is completed. One such mechanism could be the pairing (bundling) of free ends of filaments belonging to two antiparallel half-spindles. Since bundling and sliding interactions in ParM filaments have only been reported qualitatively so far, we attempt to quantify the parameters associated with these interactions.

7.3.2. Quantitative image analysis of ParM filament sliding

In an *E. coli* cell, the direct observation of sliding interactions in ParM filaments is hampered greatly due to the diffraction limit of light. Therefore, the use of computer simulations is most suited to identify the potential role of ParM filament sliding in prokaryotic spindle assembly and segregation. However, simulations of this process are currently hindered by the lack of quantitative information on ParM filament sliding. We quantify for the first time to our knowledge, the parameters of sliding of ParM filaments from *in vitro* microscopy data using image analysis. The quantified parameters include:

- (a) The angle of contact made by filaments prior to sliding, when they approach each other in the field of view.
- (b) The diffusive behavior of short ParM filaments that slide onto long filaments.
- (c) The phases in which sliding occurs *in vitro*.
- (d) The persistence length of individual ParM filaments and bundles.

Towards quantitative image analysis, we employ multiple programs. A customized MATLAB code was used to determine the angle of contact of ParM filaments interactively. The diffusion and sliding processes were analyzed using AMTraK (Chaphalkar et al., 2016) (described in Chapter 3), an automated kymography tool implemented in MATLAB, that generates and processes kymographs. The persistence lengths of individual filaments and bundles were estimated using an open source tool named FiberApp (Usov and Mezzenga, 2015). The methodology of these analyses is described in detail in Section 7.2.2.

Sliding is favoured by acute angles of contact

Filaments were speckle labelled with Alexa568 and allowed to diffuse on the surface of the coverslip. When a diffusing filament approaches another filament either at the tip or along the length, we observe that there are two outcomes. Sliding may or may not happen successfully between these filaments (Figure 7.9A, B). In case of a successful sliding encounter, we find typically that one filament stays stationary (template filament) and the other filament slides progressively on the template filament. We quantify the smallest angle made by the pair of filaments at the point of contact (Figure 7.9C, D) and find that sliding is favoured by lower angles of contact.

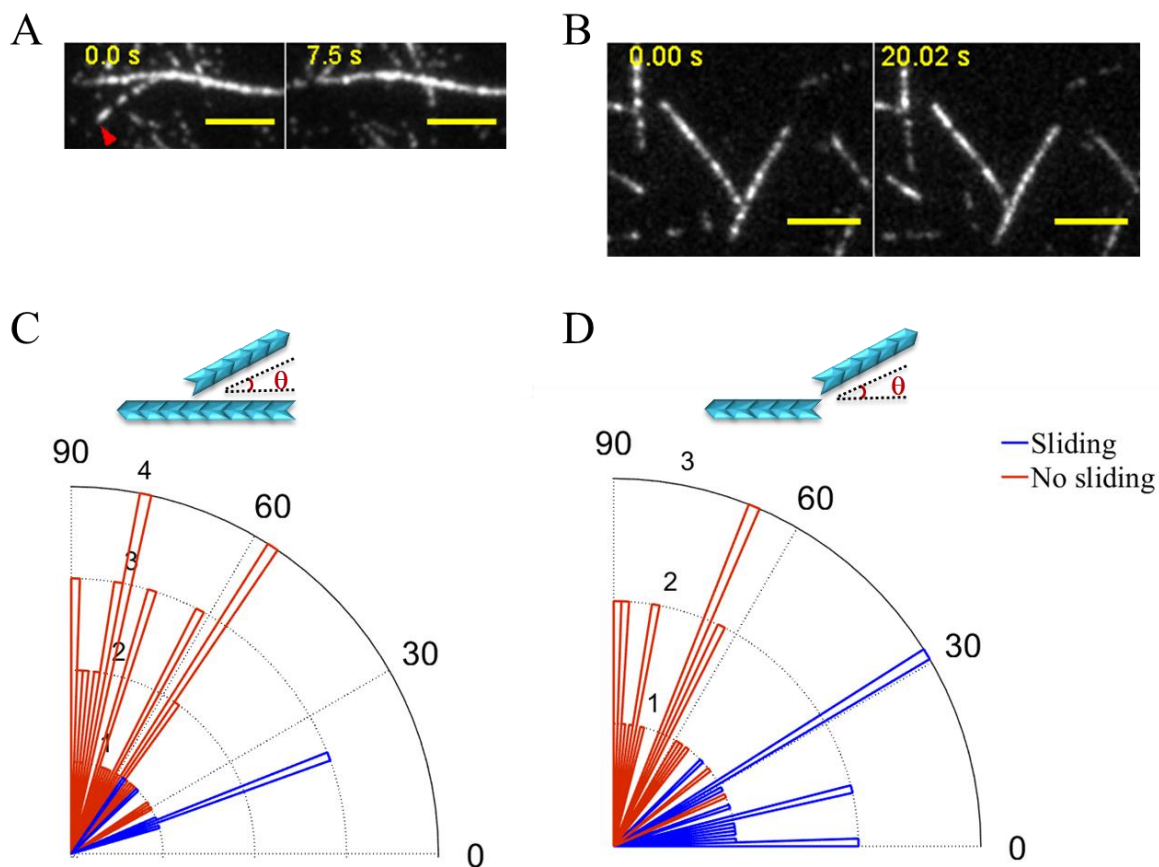


Figure 7.9. Preferred angle of contact during sliding. The first and last images from time-lapse microscopy show (A) successful sliding events and (B) unsuccessful sliding events. Time is indicated in seconds. Scale bar is 4 μm . The schematics in (C) and (D) show encounters between filaments that may either happen at the tip or elsewhere along the length of the template filament. The distribution of angles of contact (θ) for filaments are plotted as angular histograms when they meet at the (C) tip ($n = 34$) or (D) elsewhere along the length ($n = 48$). Angles for successful sliding are shown in blue while unsuccessful sliding events are shown in red.

Angles below 60° were found to be favourable for sliding events. Perpendicular encounters between filaments usually resulted in unsuccessful sliding (Figure 7.9B). On rare occasions, we saw unsuccessful sliding despite lower angles of contact. The analysis predicts that along with the angle, the orientation of the filaments may also be important for filaments to slide on each other. While we do not have polarity information in the experimental data analysed here, it has been established previously using sliding mutants that antiparallel orientation is crucial for filament sliding (Gayathri et al., 2012).

Sub-diffusive sliding of short filaments

We next quantify the sliding behaviour of short filaments on long filaments in the presence of ATP and AMPPNP (separately) to see if length of the sliding filament plays a role in the pattern of sliding observed. Short filaments (mean length - 0.5 μm) labelled with Alexa568 and long template filaments (mean length - 10 μm for AMPPNP and 2 μm for ATP) were labelled with Alexa488 (Figure 7.10A). Automated multi-channel kymography was performed using AMTraK to quantify the motion of short filaments sliding on long templates. We traced lines of interest on long template filaments and applied the same LOIs on the channel containing short filaments so as to analyse only those filaments that are present on long filaments. We find from kymographs (Figure 7.10B) that while the long filaments do not show much movement and remain stagnant over time, the short filaments perform 1D random walk-like sliding on them.

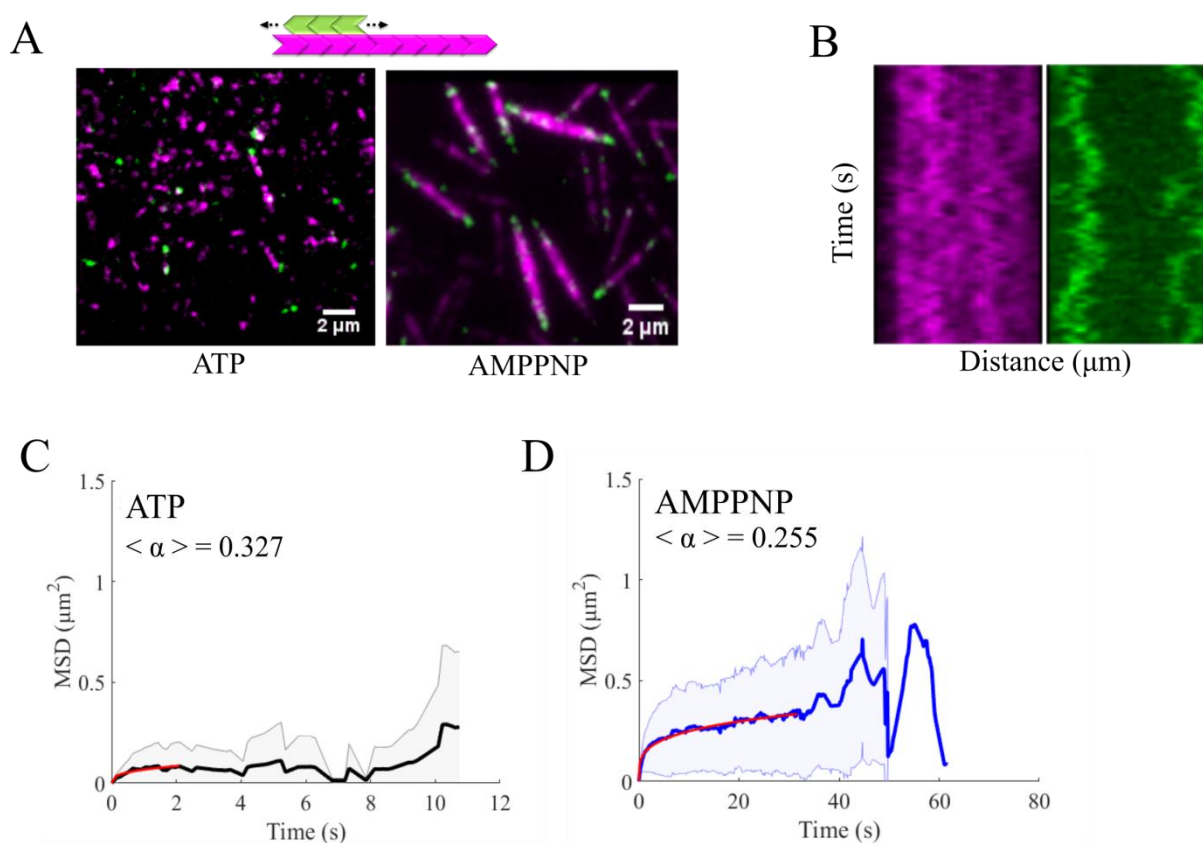


Figure 7.10. Restricted diffusion of short ParM filaments sliding on long filaments. (A) Schematic of the bidirectional sliding of short ParM filaments (green) on long static filaments (magenta). Representative images from time-series of short filaments labelled with Alexa488 (green) sliding on long filaments labelled with Alexa568 (magenta) in the presence of ATP (*left*) and AMPPNP (*right*). Scale bar is 2 μm . (B) Kymographs of static long filaments (*left*) onto which short

filaments slide (*right*). The mean square displacement (blue lines) of short filaments indicate restricted diffusion in the presence of (C) ATP ($n = 9$) and (D) AMPPNP ($n = 123$). The fit to the average MSD curve ($1/4^{\text{th}}$ portion) is marked in red.

Based on trajectories obtained by AMTraK, we calculated the mean squared displacement of these small filaments and fit the average curve to the anomalous diffusion equation (Figure 7.10C,D). We find the filaments to undergo restricted, sub-diffusive motion, further confirmed by the anomaly parameter (α) which was found to be below 1 in the presence of both, ATP and AMPPNP.

Kymography reveals three phases of filament sliding

In contrast with short filaments, long filaments that slide on template filaments of similar length showed persistent, rapid sliding in the direction that maximized the overlap between them.

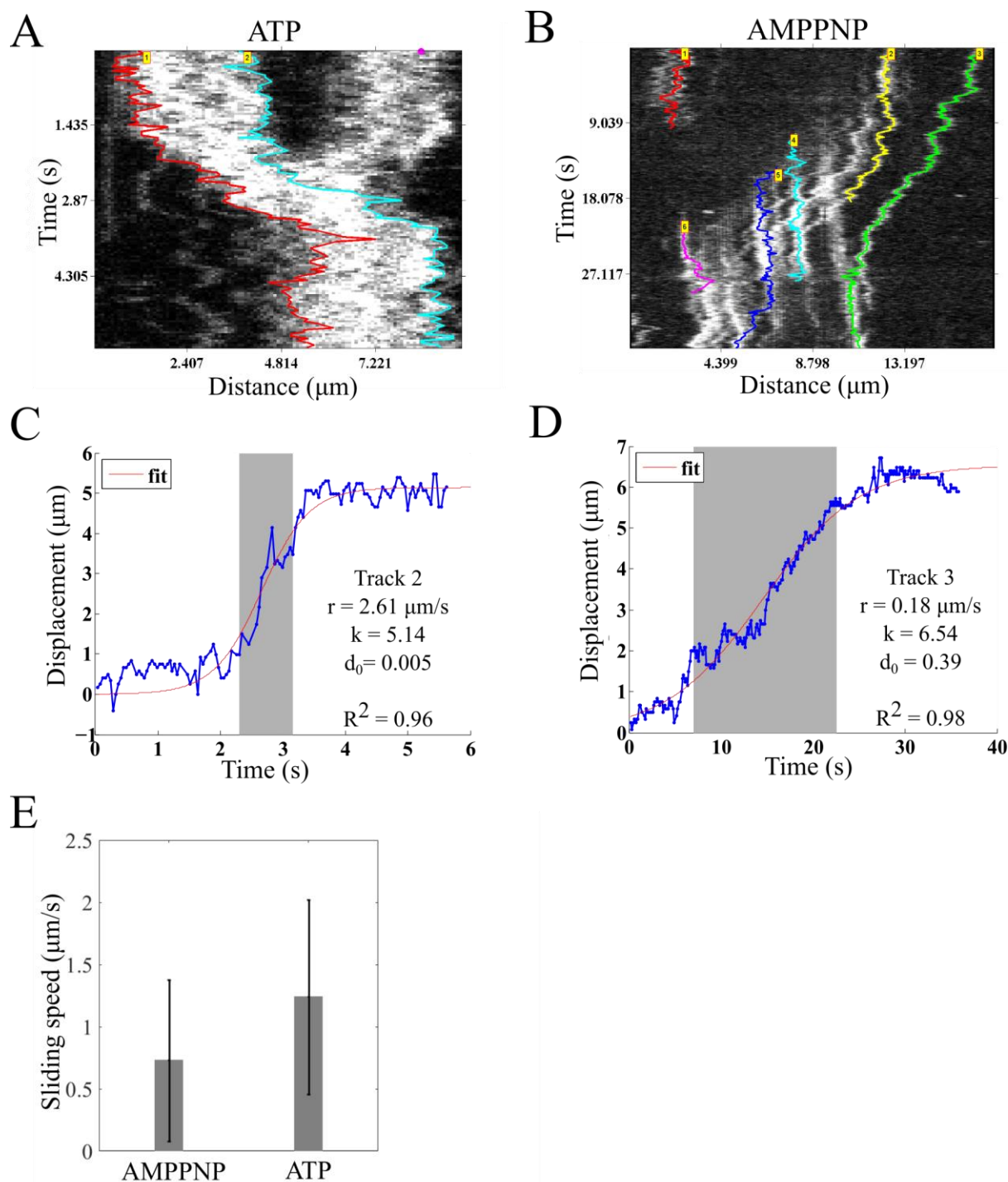


Figure 7.11. Phases in ParM sliding. Kymographs of filaments sliding in the presence of (A) ATP and (B) AMPPNP are generated and tracked using AMTraK. Coloured lines represent tracks. The tracks chosen for analysis in these particular kymographs were of speckles of tips, shown in blue in (A) and shown in green in (B).

(C) & (D) The cumulative displacement (see Section 7.2.2) profiles of chosen speckle-tracks are calculated and fit to Equation 7.4. The three phases -approach, sliding and pairing- are identified as described in Section 7.2.2. The ‘sliding’ phase is marked with a grey box. The fit parameters of sliding rate (r), maximal displacement (k) and initial displacement (d_0) are listed. (E) The average sliding speeds of ParM in the presence of ATP and AMPPNP ($n = 11$ each) are compared. Error bars indicate standard deviation.

Automated kymography was performed on pairs of filaments undergoing sliding in the presence of ATP or AMPPNP. A typical kymograph from AMTraK (Figure 7.11A,B) shows three phases of filament sliding- approach, sliding and pairing. Initially, two filaments of comparable lengths appear to be located at a distance from each other. Gradual diffusion of the filaments leads to the filaments approaching each other and encountering either at the tip (in this case) or along the length. Post contact, while one filament appears to remain stagnant, the other filament rapidly slides on it, increasing the overlap between filaments at each step. Sliding of filaments continues till the overlap between them is maximized and in 90% of the cases observed, the two filaments remained static as a pair.

The tracks obtained from processed kymographs were used to analyse the displacement and speed of sliding filaments. The cumulative displacement of each filament was plotted over time and appears to show a sigmoidal profile. The curve was fit to a logistic model (Equation 7.4) to determine the rate of sliding and segregate the three phases i.e. approach (lag), sliding (log) and pairing (stationary) based on slope (see Section 7.2.2) (Figure 7.11C,D). We find that the average sliding speeds in the presence of ATP ($1.24 \pm 0.78 \mu\text{m/s}$) and AMPPNP ($0.73 \pm 0.65 \mu\text{m/s}$) are comparable (Figure 7.11C). Surprisingly, we find the speed of sliding is ~ 50 times the velocity of polymerization of a ParM filament ($0.022 \mu\text{m/s}$). For comparison with kymography, ParM filament speckles were tracked in 2D using an ImageJ plugin- SpeckleTrackerJ (Smith et al., 2011). Sliding speeds calculated by both methods were found to be comparable.

Bundles show greater persistence length as compared to single filaments

Initial models of the ParM spindle assembly (Garner et al., 2004) suggested that a single ParM filament binds at both ends to ParRC complexes and the insertional polymerization of the filament at both ends results in segregation of the plasmids to cell poles. However, structural studies have now shown that only one end of a filament is capable of binding to a ParRC complex. The formation of a complete bipolar ParMRC spindle in the latter case would hence require at least two ParM filaments to come together and interact (Gayathri et al., 2012). Given that ParM filaments show sliding and bundling *in vitro*, one may speculate that the possible forms of inter-filament interactions in a complete spindle may involve the bundling of filaments. Intuitively, we hypothesize that the segregation of plasmids brought about by a bundle of filaments may be more advantageous than that by a

single filament. Motivated by the need to illustrate the possible advantage a bundle may have during segregation, we quantify the rigidity of single ParM filaments as well as bundles, in the form of persistence length.

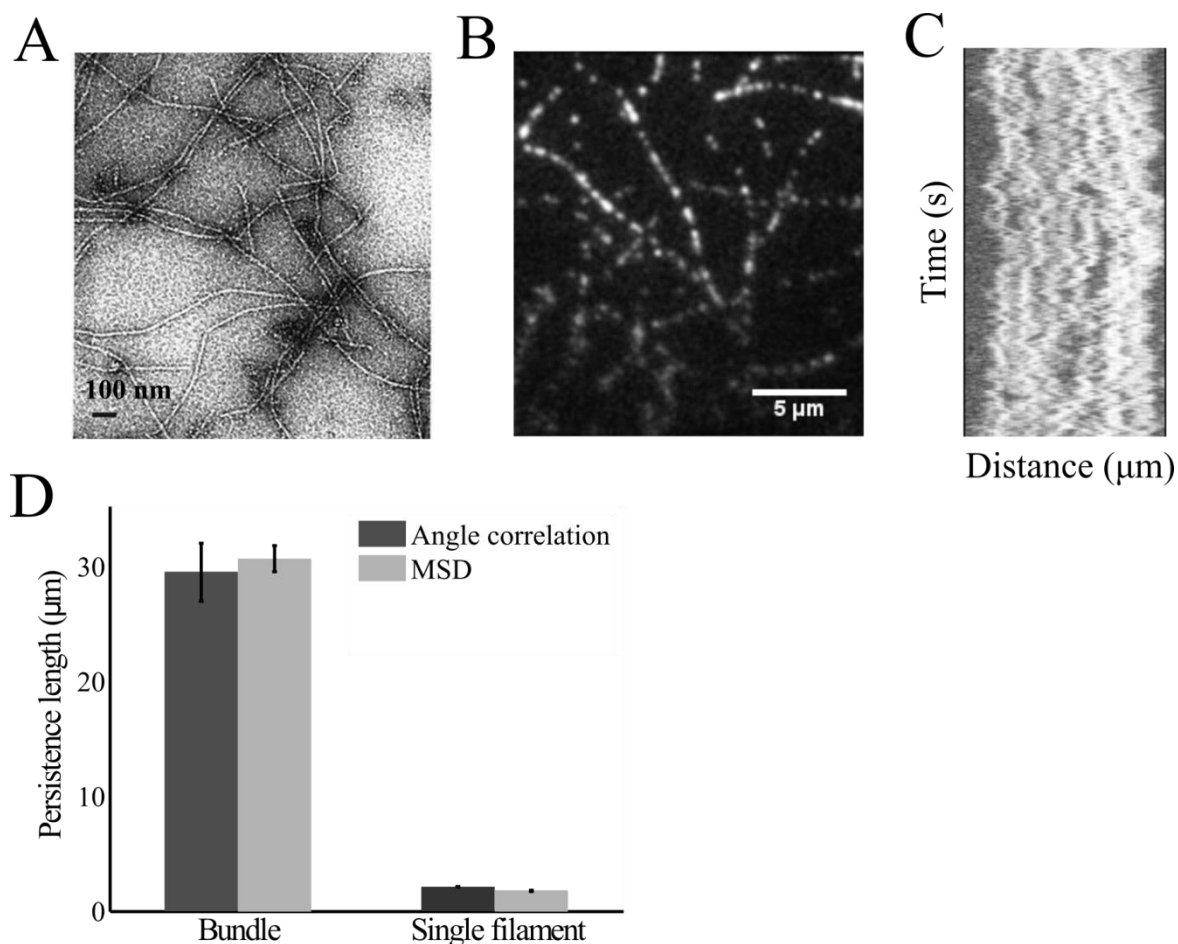


Figure 7.12. Persistence length of ParM filaments. (A) Electron micrograph taken from (Ent et al., 2002) was used to determine persistence length of single ParM filaments. Scale bar – 100 nm. (B) TIRF micrograph of bundles of ParM filaments taken from (Gayathri et al., 2012) was used to estimate the persistence length of bundles. Scale bar – 5 μm. (C) Kymograph of an image-series containing (B) shows speckles moving randomly in a disconcerted manner, confirming the presence of filament bundles. (D) Persistence lengths of individual filaments and bundled filaments were estimated and compared.

To this end, we employed FiberApp (Usov and Mezzenga, 2015), a tool that estimates the persistence length of elongated structures by image analysis. Images of single filaments (number of filaments = 25) were taken in the form of an electron micrograph from a published report (Ent et al., 2002) (Figure 7.12A). The TIRF micrographs of speckle labelled filaments obtained from (Gayathri et al., 2012) were chosen to estimate the persistence length of filament bundles (number of bundles = 40) (Figure 7.12B). We confirmed that the

filaments were indeed bundled in these image-series by performing kymography using AMTraK. Kymographs made along bright elongated filament-like structures in these images show disconcerted motion of speckles over time, confirming the presence of multiple filaments that have bundled (Figure 7.12C).

We calculate persistence length using two methods, the mean squared end-to-end distance (MSED) method and the angle correlation method (see Section). With both methods, we find that the persistence length of bundles ($\sim 30 \mu\text{m}$) is ~ 15 folds greater than that of single filaments ($\sim 2 \mu\text{m}$) (Figure 7.12D). An order of magnitude difference in the two measures strongly suggests that bundles have greater rigidity than single filaments. Bundles may therefore be capable of exerting forces across greater distances and appear to have an advantage during segregation.

7.4. Discussion

Probing the interiors of small cells such as *E. coli* ($\sim 2.8 \mu\text{m} \times 0.8 \mu\text{m}$) by light microscopy is greatly hindered due to the diffraction limit of light. Therefore, to understand the spatiotemporal organization and function of subcellular structures such as mitotic spindles within these cells, high resolution microscopy experiments need to be augmented by robust computational image analysis and theoretical modeling. In this study, we focus on the bacterial type II segregation machinery made by ParMRC molecules. Brownian dynamics based simulations are used to reconstitute the partial assembly of this spindle within an *E. coli* cell.

For the faithful segregation of a large, low copy number plasmid such as R1 (100 kb), it is crucial that replicated copies of the plasmid move from the centre of the cell to opposite poles, each travelling a distance at least $1/4^{\text{th}}$ of the cell length in the span of a few minutes. We perform simple simulations to show that plasmids with a diffusion coefficient similar to that of R1 do not translocate from the centre to the poles by plain diffusion (Figure 7.5). This result indirectly supports the fact that a dedicated spindle machinery which can translocate sister R1 plasmids to opposite poles, is required to be employed by the cell to ensure that each daughter cell receives at least one copy of the plasmid.

We further investigate the role of dynamic instability of ParM filaments in the ‘search and capture’ of plasmid targets. Our findings indicate that in an *E. coli* cell, diffusion of ParM filaments may be sufficient to bring about ‘search and capture’ of plasmids (Figure 7.7A).

Theoretical studies in eukaryotic cells have shown that dynamic instability of microtubules greatly improves the efficiency of ‘search and capture’ of chromosomes (Holy and Leibler, 1994). However, we do not observe any difference in the plasmid capture time by dynamic ParM filaments and fixed-length filaments in an *E. coli* cell (Figure 7.7A). We suspect that the contrast in ‘search and capture’ processes in eukaryotic and *E. coli* cells in terms of the role of dynamic instability could potentially be explained by the difference in the cell sizes. A systematic study of the effect of cell size or volume on plasmid capture time could be performed in future to address this hypothesis. Also, our work differs from the theoretical studies performed in eukaryotic cells in terms of number of dimensions. While Holy and Leibler (Holy and Leibler, 1994) performed calculations in 2D, our results emerge from simulations carried out in 3D, possibly explaining the contrast in results.

Further, we tested the effect of the number of filaments available per plasmid for binding on the plasmid capture time and found that capture time remains unaltered even when the ratio of filaments to plasmids increases upto 5 (Figure 7.7A). The fraction of successful capture events, however, appeared to be proportional to the number of filaments available for binding, but did not seem to be affected by dynamic instability of the filaments (Figure 7.7B).

In *E. coli*, although we show that dynamic instability of ParM filaments may not be essential to bring about the capture of plasmid targets, we speculate that dynamic filaments may play a role in the efficient capture of one half-spindle by another. In future, simulations could be performed to address this question and test if half-spindle capture time is substantially reduced when the filaments associated with the half-spindle display dynamic instability.

Our finding that filaments in a half-spindle have lifetimes shorter than the time required for segregation (Figure 7.8) suggests that other mechanisms are required to stabilize and protect the free end of a bound filament from catastrophe, thereby forming a stable bipolar spindle that can continue to elongate till the completion of segregation. A stabilized structure would persist for longer time in the cell and consequently elongate more. As an added advantage, such an elongated bipolar spindle may have increased chances of aligning with the major axis of the cell. This may thereby ensure that the two plasmids reach opposite ends of the cell and reduce the chances of the formation of a plasmid-less daughter cell. It has been hypothesized that pairing of filaments allows the stabilization of free ends. In future, it would be interesting to test this using simulations.

In addition to dynamic instability, we explored the quantitative nature of sliding interactions in ParM filaments observed *in vitro* in the presence of ATP or AMPPNP. Automated kymography using AMTraK revealed three phases – approach, sliding and pairing. Notably, filaments that approached each other at angles of contact below 60° ended up in a successful sliding event and perpendicular interactions appeared to not favour sliding. The speed of movement was estimated from the rapid sliding phase was $\sim 1 \mu\text{m/s}$, about 50 folds higher than the velocity of growth of ParM filaments reported previously. As this sliding is contractile and tends to maximise the overlap between two filaments, it is safe to assume that if sliding were to occur in the filaments of two half-spindles *in vivo*, it would oppose the direction of insertional polymerization. This may in turn offer resistance to the segregation process and affect the rate at which plasmids are being pushed apart, thus making it difficult for segregation to be completed in the reported timescale of a few minutes (Campbell and Mullins, 2007). As sliding between filaments is extremely difficult to visualize *in vivo*, this conundrum could be addressed by developing simulations of complete spindle assembly and segregation, inclusive of the sliding behaviour between filaments, based on the quantitation performed in the current work. Preliminary simulations performed with this objective hinted at the possibility of the following scenario. Sliding between two half-spindles allows minus ends of filaments (that are stabilized by pairing), to reach upto plasmids. These plasmid obstacles are now used as footholds against which the minus end of each filament continues to push, temporarily assisting the segregation. This may be accompanied by insertional polymerization at the plus end of the other filament in the pair, causing an overhang in the two filaments which is overcome by sliding yet again. However, more simulations need to be performed to deliberate on this possibility of events.

7.5. Conclusion

In this study, we found Brownian dynamics based simulations to be ideal to investigate the role of dynamic instability in ‘search and capture’ of plasmids by ParM filaments in an *E. coli* cell. Our results indicate that neither the dynamic instability of filaments, nor the number of filaments available per plasmid alter the time taken by a ParM filament to capture a plasmid.

Our novel quantitation of the *in vitro* sliding parameters of ParM filaments shows that filaments favour lower angles of contact ($<60^\circ$) for successful sliding. The persistence length of ParM bundles and individual filaments is shown to differ by an order of magnitude,

indicating the advantage of plasmid segregation by filament bundles. Automated kymography using AMTraK shows that short filaments slide on long filaments in the form of a 1D random walk, in a sub-diffusive manner. Kymography also revealed that sliding in filaments of comparable lengths proceeds in a contractile manner in three phases- approach, sliding and pairing. Interestingly, the speed of sliding was found to be ~50 times the rate of polymerization of the filament. Simulations incorporating the quantitation of filament sliding performed in this work could help identify the potential role of ParM sliding during plasmid segregation by this minimal machinery in *E. coli*.

Chapter 8

Conclusion and Outlook

In the present work, I have aimed to improve our quantitative understanding of subcellular dynamics by a combination of computational tool development, analysis of microscopy image data and computer simulations. The work is divided into two parts. The first part focuses on the development of tools for automated quantitative image analysis of microscopy data. The second part describes how these tools have been applied to study certain aspects of mechanics of cytoskeletal spindles in eukaryotic and prokaryotic cell systems through quantitative image analysis and Brownian-dynamics based simulations.

The chapters 3, 4, and 5 of the thesis describe AMTraK, FluoreT and DICOT respectively, the three automated tools I have developed for image analysis to quantify time-lapse microscopy data in labelled and label-free images. The wide utility of these tools is demonstrated by analysing diverse image-series emerging from *in vitro* microtubule gliding assays with kinesin, coalescence dynamics of microtubule-asters, clathrin assembly kinetics on lipid tethers to *in vivo* axonal vesicle transport, DNA segregation in *E. coli* and embryonic cell division in *C. elegans*. The tools are rigorously validated with simulated noisy data, tested on experimental image time-series and benchmarked by comparing their results with manual measurements, published literature and outputs of other software. The three image analysis tools described in my work are integrated into intuitive, user-friendly graphical interfaces with minimal tuneable parameters and require minimal level of computational expertise for operation. The codes are written in MATLAB, a coding environment commonly resorted to by biologists worldwide. This adds to the extensibility of these tools, allowing the scientific community to build on them in order to enhance existing features of particle segmentation and tracking. The tools are found to be precise as repeated measurements on the same data using the same set of parameters yield identical output. Owing to their objective detection criteria and open source code, we believe AMTraK, FluoreT and DICOT can be used to extract more and reproducible statistics from microscopy images.

Automated multi-peak tracking kymography (AMTraK, described in Chapter 3) was developed as an automated tool for the quantification of kymographs. Our approach detects peak and edge information and utilizes a distance minimization method for generating tracks. AMTraK displayed sub-pixel accuracy of particle-position detection when it was validated

using simulated images of beads undergoing random walk in the presence of background noise. The general applicability of the tool is illustrated by quantifying microtubule transport dynamics, clathrin polymerization kinetics, DNA segregation and axonal vesicle transport.

Fluorescence Tracker (FluoreT, described in Chapter 4), is a single particle tracking software developed for high throughput quantitation of particle motion and length in 2D. FluoreT is shown to display sub-pixel accuracy of particle-position detection even at SNR as low as 4 and reproduces identical values of parameters of motion when tested on simulated data. The speed of kinesin motors associated with microtubules in an *in vitro* assay is estimated using the tool (0.29 $\mu\text{m/s}$) and is comparable to measures from other software. We also found that while FIESTA underestimated the number of filaments in view, FluoreT could correctly estimate the value. In future, FluoreT could be improved significantly in terms of segmentation accuracy by applying Gaussian fitting algorithms as well as by providing alternative segmentation algorithms to enable the user to make a suitable choice for a given dataset. As centroid-based tracking is sensitive to fluctuations in particle shape, particles with high aspect ratios such as filaments could additionally be processed to obtain tip information. This information would be useful especially in tracking the length dynamics of filaments such as microtubules (without taxol stabilization) that grow and shrink over time and show different polymerization and depolymerisation kinetics at both ends. FluoreT could be additionally integrated with more efficient tracking algorithms such as cross-correlation and sum-absolute-difference (Cheezum et al., 2001) as alternatives to the current distance based approach. In order to resolve spatial overlaps and crossovers in filaments, ‘branch pruning’ (Athale and Chaudhari, 2011) that relies on running angles of skeleton pixels, or ‘multi-assignment’ algorithms designed for high density data (Kirubarajan et al., 2001) could be implemented. This would help to improve the accuracy of the tool in conditions of low SNR and high particle density.

Differential Interference Contrast Object Tracker (DICOT, described in Chapter 5), is a comprehensive particle tracker developed to automatically segment and track objects in DIC images, in order to quantify their movement and length. The tool is validated on experimental image-series of micron-sized beads diffusing in multiple solvents. The diffusive behaviour of beads was quantified and the effective diffusion coefficient was used to calculate the viscosity of the solvents - (i) water and (ii) 25% glycerol solution- by Stokes-Einstein’s relation. We find the estimated mean viscosities of water and 25% glycerol to be

0.001 Pa s and 0.0026 Pa s respectively, consistent with published reports. In future, as an additional feature in DICOT, the gradient detection based segmentation module in combination with distance based tracking could be utilized to analyse the length dynamics of elongated rod-shaped structures such as *E. coli* cells or cytoskeletal filaments.

Having validated DICOT, we applied it to estimate the viscosity of cytoplasm of zygotes of 6 related species of nematodes (described in Chapter 6). Our estimate of effective cytoplasmic viscosity of *C. elegans* zygotes is ~ 0.15 Pa s, about 150 times the viscosity of water (0.001 Pa s). This value obtained for *C. elegans*, however, is 4-10 folds lower than the values reported previously (Daniels et al., 2006; De Simone et al., 2018). Further, we find the viscosities vary in these related species and appear to correlate with the pattern of spindle motion and recoil velocities during positioning. Our non-invasive, label-free method for estimation of viscosity of the cytoplasm of nematode zygotes using yolk granules as endogenous probes paves way for understanding the variability that has emerged during the course of evolution, in the biophysical properties of cells and molecular assemblies such as the mitotic spindle. Zygotes of less-studied nematode species, including those other than the *Caenorhabditis* species could be analysed by this method, irrespective of the degree of their amenability to genetic and physical manipulation.

We studied the effect of dynamic instability of ParM filaments in the assembly of the minimal plasmid-segregating spindle in *E. coli* by Brownian dynamics based simulations (described in Chapter 7). We show that plasmids as large as R1 do not translocate from the centre to the poles by plain diffusion. We report that in *E. coli* cells, dynamic instability does not alter the time required for a ParM filament to capture a plasmid target (Figure 7.7A) suggesting that diffusion may be sufficient to bring about plasmid capture by ParM filaments in these cells. Our finding differs from previous studies in eukaryotic cells that show that dynamic instability of microtubules greatly improves the efficiency of search and capture of chromosomes. While dynamic instability of ParM filaments may not be essential to bring about the capture of plasmid targets, we speculate that dynamic filaments may play a role in the efficient capture of one half-spindle by another. In future, simulations could be performed to address this question and test if half-spindle capture time is substantially reduced when the filaments associated with the half-spindle are dynamically unstable. The novel quantification of ParM sliding dynamics performed in this study when combined with simulations that reconstitute the complete assembly and action of the ParMRC spindle could improve our

understanding of this minimal DNA-segregating machinery and help identify the potential role of inter-filament interactions in the process.

In conclusion, my work highlights the utility of novel tool development and its application to the dynamics of subcellular processes both *in vitro* and *in vivo*. Quantitative studies on a high throughput scale using such tools could be utilized to gain new insights in old biological problems through the analysis of labelled and label-free imaging data.

Bibliography

- Allan, V.J., and R.D. Vale. 1991. Control of Microtubule-based Membrane Transport and Tubule Formation In Vitro. *J. Cell Biol.* 113:347–359.
- Araki, S., T. Nakai, K. Hizume, K. Takeyasu, and K. Yoshikawa. 2006. Hydrodynamic radius of circular DNA is larger than that of linear DNA. *Chem. Phys. Lett.* 418:255–259. doi:10.1016/j.cplett.2005.10.115.
- Athale, C. a, A. Dinarina, F. Nedelec, and E. Karsenti. 2014. Collective behavior of minus-ended motors in mitotic microtubule asters gliding toward DNA. *Phys. Biol.* 11:016008. doi:10.1088/1478-3975/11/1/016008.
- Athale, C.A., and H. Chaudhari. 2011a. Population length variability and nucleoid numbers in Escherichia coli. *Bioinformatics.* 27:2944–8. doi:10.1093/bioinformatics/btr501.
- Athale, C.A., and H. Chaudhari. 2011b. Population Length Variability and Nucleoid Numbers in E. coli. *Bioinformatics.* 27:2944–2948. doi:10.1093/bioinformatics/btr501.
- Athale, C.A., A. Dinarina, M. Mora-Coral, C. Pugieux, F. Nedelec, and E. Karsenti. 2008. Regulation of microtubule dynamics by reaction cascades around chromosomes. *Science (80-)*. 322:1243–1247.
- Avinoam, O., M. Schorb, C.J. Beese, J.A. Briggs, and M. Kaksonen. 2015. Endocytosis. Endocytic sites mature by continuous bending and remodeling of the clathrin coat. *Science (80-)*. 348:1369–1372.
- Aylett, C.H.S., Q. Wang, K.A. Michie, L.A. Amos, and J. Löwe. 2010. Filament structure of bacterial tubulin homologue TubZ. *PNAS.* 107:19766–19771. doi:10.1073/pnas.1010176107.
- Bakshi, S., A. Siryaporn, M. Goulian, and J.C. Weisshaar. 2012. Superresolution imaging of ribosomes and RNA polymerase in live Escherichia coli cells. *Mol. Microbiol.* 85:21–38. doi:10.1111/j.1365-2958.2012.08081.x.
- Becker, E., N.C. Herrera, F.Q. Gunderson, A.I. Derman, A.L. Dance, J. Sims, R. a Larsen, and J. Pogliano. 2006. DNA segregation by the bacterial actin Alfa during Bacillus subtilis growth and development. *EMBO J.* 25:5919–31. doi:10.1038/sj.emboj.7601443.
- Bicek, A.D., E. Tuzel, A. Demtchouk, M. Uppalapati, W.O. Hancock, D.M. Kroll, and D.J. Odde. 2009. Anterograde microtubule transport drives microtubule bending in LLC-PK1 epithelial cells. *Mol. Biol. Cell.* 20:2943–2953.
- Bradley, D., and G. Roth. 2007. Adaptive Thresholding Using the Integral Image. *J. Graph. Tools.* 12:13–21.
- Bridgman, P.C. 1999. {M}yosin {V}a movements in normal and dilute-lethal axons provide support for a dual filament motor complex. *J. Cell Biol.* 146:1045–1060.
- Brookes, Mike (Department of Electrical & Electronic Engineering, Imperial College, Exhibition Road, London, U. 2005. Voicebox.
- Burbank, K.S., T.J. Mitchison, and D.S. Fisher. 2007. Slide-and-Cluster models for spindle

- assembly. *Curr. Biol.* 17:1373–1383. doi:10.1016/j.cub.2007.07.058.
- Buscall, R., P. D'Haene, and J. Mewis. 1994. Maximum Density for Flow of Dispersions of Near Monodisperse Spherical Particles. *Langmuir.* 10:1439–1441. doi:10.1021/la00017a020.
- Cabeen, M.T., and C. Jacobs-wagner. 2010. The Bacterial Cytoskeleton. *Annu. Rev. Genet.* 44:365–392. doi:10.1146/annurev-genet-102108-134845.
- Campbell, C.S., and R.D. Mullins. 2007. In vivo visualization of type II plasmid segregation: Bacterial actin filaments pushing plasmids. *J. Cell Biol.* 179:1059–1066. doi:10.1083/jcb.200708206.
- Canny, J. 1986. A Computational Approach to Edge Detection. *Pattern Anal. Mach. Intell. IEEE Trans.* PAMI-8:679–698.
- Carpenter, A.E., T.R. Jones, M.R. Lamprecht, C. Clarke, I.H. Kang, O. Friman, D.A. Guertin, J.H. Chang, R.A. Lindquist, J. Moffat, P. Golland, and D.M. Sabatini. 2006. CellProfiler : image analysis software for identifying and quantifying cell phenotypes. doi:10.1186/gb-2006-7-10-r100.
- Chaphalkar, A.R., K. Jain, M.S. Gangan, and C.A. Athale. 2016. Automated Multi-Peak Tracking Kymography (AMTraK): A Tool to Quantify Subcellular Dynamics with Sub-Pixel Accuracy. *PLoS One.* 11:e0167620. doi:10.1371/journal.pone.0167620.
- Cheezum, M.K., W.F. Walker, and W.H. Guilford. 2001. Quantitative comparison of algorithms for tracking single fluorescent particles. *Biophys. J.* 81:2378–88. doi:10.1016/S0006-3495(01)75884-5.
- Chen, Y.-Q., C.-Y. Kuo, M.-T. Wei, K. Wu, P.-T. Su, C.-S. Huang, and A. Chiou. 2013. Intracellular viscoelasticity of HeLa cells during cell division studied by video particle-tracking microrheology. *J. Biomed. Opt.* 19:011008. doi:10.1117/1.JBO.19.1.011008.
- Chenouard, N., J. Buisson, I. Bloch, P. Bastin, T. Paristech, and C.U.M.R. Ltc. 2010. Curvelet analysis of kymograph for tracking bi-directional particles in fluorescence microscopy images. *Proc. 2010 IEEE 17th Int. Conf. Image Process.* 3657–3660.
- Chenouard, N., I. Smal, F. de Chaumont, M. Maška, I.F. Sbalzarini, Y. Gong, J. Cardinale, C. Carthel, S. Coraluppi, M. Winter, A.R. Cohen, W.J. Godinez, K. Rohr, Y. Kalaidzidis, L. Liang, J. Duncan, H. Shen, Y. Xu, K.E.G. Magnusson, J. Jaldén, H.M. Blau, P. Paul-Gilloteaux, P. Roudot, C. Kervrann, F. Waharte, J.-Y. Tinevez, S.L. Shorte, J. Willemse, K. Celler, G.P. van Wezel, H.-W. Dan, Y.-S. Tsai, C. Ortiz de Solórzano, J.-C. Olivo-Marin, and E. Meijering. 2014. Objective comparison of particle tracking methods. *Nat. Methods.* 11:281–9. doi:10.1038/nmeth.2808.
- Chetta, J., and S.B. Shah. 2011. A novel algorithm to generate kymographs from dynamic axons for the quantitative analysis of axonal transport. *J. Neurosci. Methods.* 199:230–40. doi:10.1016/j.jneumeth.2011.05.013.
- Chiba, K., Y. Shimada, M. Kinjo, T. Suzuki, and S. Uchida. 2014. Simple and direct assembly of kymographs from movies using KYMOMAKER. *Traffic.* 15:1–11. doi:10.1111/tra.12127.
- Cluet, D., P. Ste, S. Riche, M. Spichty, and M. Delattre. 2014. Automated High-Throughput

- Quantification of Mitotic Spindle Positioning from DIC Movies of *Caenorhabditis* Embryos. *PLoS One*. 9. doi:10.1371/journal.pone.0093718.
- Cytoskeleton. 2005. Kinesin Motility Assay Biochem Kit BK027. Denver, CO, USA.
- Daniels, B.R., B.C. Masi, and D. Wirtz. 2006. Probing single-cell micromechanics in vivo: The microrheology of *C. elegans* developing embryos. *Biophys. J.* 90:4712–4719. doi:10.1529/biophysj.105.080606.
- Das, M., T. Drake, D.J. Wiley, P. Buchwald, D. Vavylonis, and F. Verde. 2012. Oscillatory dynamics of Cdc42 GTPase in the control of polarized growth. *Science (80-.)*. 337:239–243.
- Dixit, R., and R. Cyr. 2003. Cell damage and reactive oxygen species production induced by fluorescence microscopy: effect on mitosis and guidelines for non-invasive fluorescence microscopy. *Plant J.* 36:280–290. doi:10.1046/j.1365-313X.2003.01868.x.
- Ducret, A., E.M. Quardokus, and Y. V Brun. 2016. MicrobeJ, a high throughput tool for quantitative bacterial cell detection and analysis. *Nat. Microbiol.* 1:1–7. doi:10.1038/nmicrobiol.2016.77.
- Ebersbach, G., and K. Gerdes. 2005. Plasmid segregation mechanisms. *Annu. Rev. Genet.* 39:453–79. doi:10.1146/annurev.genet.38.072902.091252.
- Ent, F. Van Den, J. Moller-jensen, L.A. Amos, K. Gerdes, and J. Lo. 2002. F-actin-like lamaments formed by plasmid segregation protein ParM. 21:6935–6943.
- Etoc, F., E. Balloul, C. Vicario, D. Normanno, D. Liße, A. Sittner, J. Piehler, M. Dahan, and M. Coppey. 2018. Non-specific interactions govern cytosolic diffusion of nanosized objects in mammalian cells. *Nat. Mater.* 17:740–746. doi:10.1038/s41563-018-0120-7.
- Farhadifar, R., C.F. Baer, M. Delattre, D.J. Needleman, M. Delattre, E.C. Andersen, and T. Mu. 2015. Scaling , Selection , and Evolutionary Dynamics of the Mitotic Spindle Scaling , Selection , and Evolutionary Dynamics of the Mitotic Spindle. *Curr. Biol.* 25:732–740. doi:10.1016/j.cub.2014.12.060.
- Fink, G., and J. Löwe. 2015. Reconstitution of a prokaryotic minus end-tracking system using TubRC centromeric complexes and tubulin-like protein TubZ filaments. *PNAS.* 112:1845–1850. doi:10.1073/pnas.1423746112.
- Fisher, J.K., A. Bourniquel, G. Witz, B. Weiner, M. Prentiss, and N. Kleckner. 2013. Four-dimensional imaging of *E. coli* nucleoid organization and dynamics in living cells. *Cell.* 153:882–95. doi:10.1016/j.cell.2013.04.006.
- Footer, M., J. Kersemakers, J. Theriot, and M. Dogterom. 2007. Direct measurement of force generation by actin filament polymerization using an optical trap. *Proc. Natl. Acad. Sci.* 104:2181–2186. doi:10.1073/pnas.0607052104.
- Foster, P.J., S. Fürthauer, M.J. Shelley, and D.J. Needleman. 2015. Active contraction of microtubule networks Active Contraction of Microtubule Networks. *Elife.* 4:e10837:1–21. doi:10.7554/eLife.10837.
- Gadde, S., and R. Heald. 2004. Mechanisms and Molecules of the Mitotic Spindle. *Curr. Biol.* 14:797–805. doi:10.1016/j.cub.2004.09.021.

- Gallo, I. 2008. No Title. <https://imagej.nih.gov/ij/plugins/poisson-noise.html>.
- Garner, E.C., C.S. Campbell, and R.D. Mullins. 2004. Dynamic instability in a DNA-segregating prokaryotic actin homolog. *Science*. 306:1021–5. doi:10.1126/science.1101313.
- Garner, E.C., C.S. Campbell, D.B. Weibel, and R.D. Mullins. 2007. Reconstitution of DNA segregation driven by assembly of a prokaryotic actin homolog. *Science*. 315:1270–4. doi:10.1126/science.1138527.
- Garzon-Coral, C., H.A. Fantana, and J. Howard. 2016. A force-generating machinery maintains the spindle at the cell center during mitosis. *Science (80-.)*. 352:1124–1127. doi:10.1126/science.aad9745.
- Gayathri, P., T. Fujii, J. Møller-Jensen, F. van den Ent, K. Namba, and J. Löwe. 2012. A bipolar spindle of antiparallel ParM filaments drives bacterial plasmid segregation. *Science*. 338:1334–7. doi:10.1126/science.1229091.
- Gerdes, K., M. Howard, and F. Szardenings. 2010. Pushing and pulling in prokaryotic DNA segregation. *Cell*. 141:927–42. doi:10.1016/j.cell.2010.05.033.
- Gerdes, K., and S. Molin. 1986. Partitioning Structural and Functional of Plasmid R1 Analysis of the parA Locus. *J. Mol. Biol.* 190:269–279.
- Ghosh, S.K., S. Hajra, A. Paek, and M. Jayaram. 2006. Mechanisms for Chromosome and Plasmid Segregation. *Annu. Rev. Biochem.* 75:211–241. doi:10.1146/annurev.biochem.75.101304.124037.
- Gibbons, F., J.F. Chauwin, M. Despósito, and J. V José. 2001. A dynamical model of kinesin-microtubule motility assays. *Biophys. J.* 80:2515–26. doi:10.1016/S0006-3495(01)76223-6.
- Gittes, F., B. Mickey, J. Nettleton, and J. Howard. 1993. Flexural rigidity of microtubules and actin filaments measured from thermal fluctuations in shape. *J. Cell Biol.* 120:923–934. doi:10.1083/jcb.120.4.923.
- Gonzalez, R.C., and R.E. Woods. 2008. Digital Image Processing. Third Edit. Pearson Education Inc.
- Goshima, G., and J.M. Scholey. 2010. Control of mitotic spindle length. *Annu. Rev. Cell Dev. Biol.* 26:21–57. doi:10.1146/annurev-cellbio-100109-104006.
- Grill, S.W., and A.A. Hyman. 2005. Spindle positioning by cortical pulling forces. *Dev. Cell*. 8:461–465. doi:10.1016/j.devcel.2005.03.014.
- Grover, R., J. Fischer, F.W. Schwarz, W.J. Walter, P. Schwille, and S. Diez. 2016. Transport efficiency of membrane-anchored kinesin-1 motors depends on motor density and diffusivity. *PNAS*. 113:E7185-E7193-. doi:10.1073/pnas.1611398113.
- Guberman, J.M., A. Fay, J. Dworkin, N.S. Wingreen, and Z. Gitai. 2008. PSICIC: noise and asymmetry in bacterial division revealed by computational image analysis at sub-pixel resolution. *PLoS Comput. Biol.* 4:e1000233. doi:10.1371/journal.pcbi.1000233.
- Hallman, S. 2007. Make_Kymograph plugin.

- Hendricks, A.G., E. Perlson, J.L. Ross, H.W. Schroeder, M. Tokito, and E.L. Holzbaur. 2010. {M}otor coordination via a tug-of-war mechanism drives bidirectional vesicle transport. *Curr. Biol.* 20:697–702.
- Hill, D.B., M.J. Plaza, K. Bonin, and G. Holzwarth. 2004. Fast vesicle transport in PC12 neurites: velocities and forces. *Eur. Biophys. J.* 33:623–32. doi:10.1007/s00249-004-0403-6.
- Holkar, S.S., S.C. Kamerkar, and T.J. Pucadyil. 2015. Spatial control of epsin-induced clathrin assembly by membrane curvature. *J. Biol. Chem.* 290:14267–14276. doi:10.1074/jbc.M115.653394.
- Holy, T.E., and S. Leibler. 1994. Dynamic instability of microtubules as an efficient way to search in space. *Proc. Natl. Acad. Sci. U. S. A.* 91:5682–5685.
- Howard, J. 2001. *Mechanics of Motor Proteins and the Cytoskeleton*. Sinauer Associates, Sunderland.
- Howard, J. 2014. Quantitative cell biology: the essential role of theory. *Mol. Biol. Cell.* 25:3438–40. doi:10.1091/mbc.E14-02-0715.
- Howard, J., A.J. Hudspeth, and R.D. Vale. 1989. Movement of microtubules by single kinesin molecules. *Nature.* 342:154–158.
- Ikuta, J., N.K. Kamisetty, H. Shintaku, H. Kotera, T. Kon, and R. Yokokawa. 2014. Tug-of-war of microtubule filaments at the boundary of a kinesin- and dynein-patterned surface. *Sci. Reports.* 4:5281. doi:10.1038/srep05281.
- Jain, K., N. Khetan, and C.A. Athale. 2019. Collective effects of yeast cytoplasmic dynein based microtubule transport. *Soft Matter.* doi:10.1039/b000000x/.
- Jaqaman, K., D. Loerke, M. Mettlen, H. Kuwata, S. Grinstein, S.L. Schmid, and G. Danuser. 2008. Robust single-particle tracking in live-cell time-lapse sequences Supplementary Figure 1 Gap closing , merging and splitting statistics for experimental data. 5. doi:10.1038/NMETH.1237.
- Jensen, R.B., and K. Gerdes. 1999. Mechanism of DNA segregation in prokaryotes : ParM partitioning protein of plasmid R1 co-localizes with its replicon during the cell cycle. 18:4076–4084.
- Kalthoff, C., J. Alves, C. Urbanke, R. Knorr, and E.J. Ungewickell. 2002. Unusual structural organization of the endocytic proteins AP180 and epsin 1. *J. Biol. Chem.* 277:8209–8216.
- Kasprovicz, R., R. Suman, and P.O. Toole. 2017. Characterising live cell behaviour : Traditional label-free and quantitative phase imaging approaches. *Int. J. Biochem. Cell Biol.* 84:89–95. doi:10.1016/j.biocel.2017.01.004.
- Khetan, N., and C.A. Athale. 2016. A Motor-Gradient and Clustering Model of the Centripetal Motility of MTOCs in Meiosis I of Mouse Oocytes. *PLoS Comput. Biol.* 12:e1005102. doi:10.1371/journal.pcbi.1005102.
- Kirschner, M., and T. Mitchison. 1986. Beyond self-assembly: chromosomes and for spindle assembly in mammalian cells. From microtubules to morphogenesis. *Cell.* 45:329–342.

- Kirubarajan, T., Y. Bar-Shalom, and K.R. Pattipati. 2001. Multiassignment for Tracking a Large Number of Overlapping Objects. *IEEE Trans. Aerosp. Electron. Syst.* 37.
- Korson, L., W. Drost-Hansen, and F.J. Millero. 1969. Viscosity of water at various temperatures. *J. Phys. Chem.* 73:34–39. doi:10.1021/j100721a006.
- Kozlowski, C., M. Srayko, and F. Nedelec. 2007. Cortical Microtubule Contacts Position the Spindle in *C. elegans* Embryos. *Cell.* 129:499–510. doi:10.1016/j.cell.2007.03.027.
- Krieger, I., and T. Dougherty. 1959. A mechanism for non-Newtonian flow in suspensions of rigid spheres. *Trans. Soc. Rheol.* 3:137–152.
- Leduc, C., F. Ruhnnow, J. Howard, and S. Diez. 2007. Detection of fractional steps in cargo movement by the collective operation of kinesin-1 motors. *Proc. Natl. Acad. Sci. U. S. A.* 104:10847–10852. doi:10.1073/pnas.0701864104.
- Li, H.W., M. McCloskey, Y. He, and E.S. Yeung. 2007. Real-time dynamics of label-free single mast cell granules revealed by differential interference contrast microscopy. *Anal. Bioanal. Chem.* 387:63–69. doi:10.1007/s00216-006-0403-8.
- Loughlin, R., R. Heald, and F. Nedelec. 2010. A computational model predicts *Xenopus* meiotic spindle organization. *J. Cell Biol.* 191:1239–1249. doi:10.1083/jcb.201006076.
- Lüdecke, A., A. Seidel, M. Braun, and S. Diez. 2018. Diffusive tail anchorage determines velocity and force produced by kinesin-14 between crosslinked microtubules. *Nat. Commun.* 9. doi:10.1038/s41467-018-04656-0.
- Maeder, C.I., A. San-Miguel, E.Y. Wu, H. Lu, and K. Shen. 2014. *In vivo* neuron-wide analysis of synaptic vesicle precursor trafficking. *Traffic.* 15:273–291.
- Mangeol, P., B. Prevo, and E.J.G. Peterman. 2016. KymographClear and KymographDirect : two tools for the automated quantitative analysis of molecular and cellular dynamics using kymographs KymographClear and KymographDirect workflow and features. *Mol. Biol. Cell.*
- Martin, D.S. 2013. Measuring microtubule persistence length using a microtubule gliding assay. *Methods Cell Biol.* 115:13–25.
- Maska, M., V. Ulman, D. Svoboda, P. Matula, P. Matula, S. Venkatesan, C. Ederra, A. Urbiola, C. Carthel, D.M.W. Balak, P. Karas, T. Bolckova, S. Coraluppi, N. Harder, K. Rohr, K.E.G. Magnusson, J. Jalde, G.M. Hagen, H.M. Blau, O. Dzyubachyk, P. Kr, D. Pastor-escuredo, D. Jimenez-carretero, M.J. Ledesma-carbayo, E. Meijering, M. Kozubek, and C. Ortiz-de-solorzano. 2014. A benchmark for comparison of cell tracking algorithms. *Bioinformatics.* 30:1609–1617. doi:10.1093/bioinformatics/btu080.
- Meyer, F. 1994. Topographic distance and watershed lines. *Signal Processing.* 38:113–125.
- Michie, K.A., J. Löwe, L. Jan, and J. Löwe. 2006. Dynamic filaments of the bacterial cytoskeleton. *Annu. Rev. Biochem.* 75:467–92. doi:10.1146/annurev.biochem.75.103004.142452.
- Mitchison, T., and M. Kirschner. 1984. Dynamic instability of microtubule growth. *Nature.* 312:237–242.

- Miura, K. 2005. Tracking Movement in Cell Biology. 267–295. doi:10.1007/b102218.
- Mogilner, A., R. Wollman, G. Civelekoglu-scholey, and J. Scholey. 2006. Modeling mitosis. *Trends Cell Biol.* 16:88–96. doi:10.1016/j.tcb.2005.12.007.
- Moller-Jensen, J., J. Borch, M. Dam, R.B. Jensen, P. Roepstorff, and K. Gerdes. 2003. Bacterial Mitosis: ParM of Plasmid R1 Moves Plasmid DNA by an Actin-like Insertional Polymerization Mechanism. *Mol. Cell.* 12:1477–1487. doi:10.1016/S1097-2765(03)00451-9.
- Moller-Jensen, J., J. Lowe, and K. Gerdes. 2002. Prokaryotic DNA segregation by an actin-like filament. *EMBO J.* 21:3119–3127.
- Moller-Jensen, J., S. Ringgaard, C.P. Mercogliano, K. Gerdes, and J. Lowe. 2007. Structural analysis of the ParR / parC plasmid partition complex. *EMBO J.* 26:4413–4422. doi:10.1038/sj.emboj.7601864.
- Mondal, S., S. Ahlawat, K. Rau, V. Venkataraman, and S.P. Koushika. 2011. Imaging in vivo Neuronal Transport in Genetic Model Organisms Using Microfluidic Devices. *Traffic.* 12:372–385. doi:10.1111/j.1600-0854.2010.01157.x.
- Mullineaux, C., A. Nenninger, and N. Ray. 2006. Diffusion of green fluorescent protein in three cell environments in Escherichia coli. *J. Bacteriol.* 188:3442–3448. doi:10.1128/JB.188.10.3442.
- Murphy, D.B. 2001. Fundamentals of light microscopy and electronic imaging.
- Nedelec, F. 2002. Computer simulations reveal motor properties generating stable antiparallel microtubule interactions. *J. Cell Biol.* 158:1005–1015. doi:10.1083/jcb.200202051.
- Nedelec, F., and D. Foethke. 2007. Collective Langevin dynamics of flexible cytoskeletal fibers. *New J. Phys.* 9:427. doi:10.1088/1367-2630/9/11/427.
- Nedelec, F.J., T. Surrey, A.C. Maggs, and S. Leibler. 1997. Self-organization of microtubules and motors. *Nature.* 389:305–308.
- Neumann, S., T.J. Pucadyil, and S.L. Schmid. 2013. Analyzing membrane remodeling and fission using supported bilayers with excess membrane reservoir. *Nat Protoc.* 8:213–222.
- Nielsen, H.J., J.R. Ottesen, B. Youngren, S.J. Austin, and F.G. Hansen. 2006. The Escherichia coli chromosome is organized with the left and right chromosome arms in separate cell halves. *Mol. Microbiol.* 62:331–338. doi:10.1111/j.1365-2958.2006.05346.x.
- Nitzsche, B., V. Bormuth, C. Brauer, J. Howard, L. Ionov, J. Kerssemakers, T. Korten, C. Leduc, F. Ruhnaw, and S. Diez. 2010. Studying kinesin motors by optical 3D-nanometry in gliding motility assays. *Methods Cell Biol.* 95:247–271.
- Nordstrom, K., and S.J. Austin. 1989. Mechanisms that contribute to the stable segregation of plasmids. *Annu. Rev. Genet.* 23:37–69.
- Nordström, K., and S. Dasgupta. 2006. Copy-number control of the Escherichia coli chromosome: a plasmidologist's view. *EMBO Rep.* 7:484–489.

doi:10.1038/sj.embor.7400681.

- Otsu, N.N. 1979. A Threshold Selection Method from Gray-Level Histograms. *IEEE Trans. Syst. Man Cybern.* 9:62–66. doi:10.1109/TSMC.1979.4310076.
- Pawley, J.B. 1995. Handbook of biological confocal microscopy. 2nd ed. J.B. Pawley, editor.
- Pereira, A.J., and H. Maiato. 2010. Improved kymography tools and its applications to mitosis. *Methods.* 51:214–9. doi:10.1016/j.ymeth.2010.01.016.
- Perona, P., and J. Malik. 1990. Scale-space and edge detection using anisotropic diffusion. *IEEE Trans. Pattern Anal. Mach. Intell.* 12:629–639. doi:10.1109/34.56205.
- Perrin, J. 1910. Brownian movement and molecular reality, translation by F. Soddy (Taylor and Francis, London).
- Piccinini, F., A. Kiss, and P. Horvath. 2016. CellTracker (not only) for dummies. *Bioinformatics.* 32:955–957.
- Pucadyil, T.J., and S.L. Schmid. 2010. Supported bilayers with excess membrane reservoir: a template for reconstituting membrane budding and fission. *Biophys. J.* 99:517–525.
- Quemada, D. 1977. Rheology of concentrated disperse systems and minimum energy dissipation principle I. Viscosity-concentration relationship. *Rheol. Acta.* 16:82–94.
- Reshes, G., S. Vanounou, I. Fishov, and M. Feingold. 2008. Cell shape dynamics in *Escherichia coli*. *Biophys. J.* 94:251–264. doi:10.1529/biophysj.107.104398.
- Reyes-lamothe, R., D.J. Sherratt, and M.C. Leake. 2010. Stoichiometry and architecture of active DNA replication machinery in *Escherichia coli* *. *Science (80-.)*. 328:498–501. doi:10.1126/science.1185757.Stoichiometry.
- Reyes-Lamothe, R., T. Tran, D. Meas, L. Lee, A.M. Li, D.J. Sherratt, and M.E. Tolmasky. 2014. High-copy bacterial plasmids diffuse in the nucleoid-free space , replicate stochastically and are randomly partitioned at cell division. *Nucleic Acids Res.* 42:1042–1051. doi:10.1093/nar/gkt918.
- Riche, S., M. Zouak, A. Arneodo, J. Pecreaux, and M. Delattre. 2013. Evolutionary comparisons reveal a positional switch for spindle pole oscillations in. *J. Cell Biol.* 201:653–662. doi:10.1083/jcb.201210110.
- Rietdorf, Jens (FMI, B., and A. (EMBL H. Seitz. 2008. Kymograph (time space plot) Plugin for ImageJ.
- Rietdorf, J., and A. Seitz. 2008. Multi Kymograph.
- Rob Phillips, J. Kondev, J. Theriot, and H. Garcia. 2012. Physical Biology of the Cell. 2nd ed. Garland Science, Taylor and Francis Group LLC: New York. 1057 pp.
- Rogers, S.S., T.A. Waigh, and J.R. Lu. 2008. Intracellular microrheology of motile amoeba proteus. *Biophys. J.* 94:3313–3322. doi:10.1529/biophysj.107.123851.
- Ruhnow, F., D. Zwicker, and S. Diez. 2011. Tracking single particles and elongated filaments with nanometer precision. *Biophys. J.* 100:2820–8. doi:10.1016/j.bpj.2011.04.023.

- Sachs, C.C., A. Grünberger, S. Helfrich, C. Probst, W. Wiechert, D. Kohlheyer, and K. Nöh. 2016. Image-Based Single Cell Profiling : High- Throughput Processing of Mother Machine Experiments. *PLoS One*. 11:e0163453. doi:10.1371/journal.pone.0163453.
- Sarah Grah, J., J. Alison Harrington, S. Boon Koh, J. Andrew Pike, A. Schreiner, M. Burger, C. Schönlieb, and S. Reichelt. 2017. Mathematical imaging methods for mitosis analysis in live-cell phase contrast microscopy. *Methods*. 115:91–99. doi:10.1016/j.ymeth.2017.02.001.
- Schindelin, J., I. Arganda-Carreras, E. Frise, V. Kaynig, M. Longair, T. Pietzsch, S. Preibisch, C. Rueden, S. Saalfeld, B. Schmid, J.Y. Tinevez, D.J. White, V. Hartenstein, K. Eliceiri, P. Tomancak, and A. Cardona. 2012. Fiji: An open-source platform for biological-image analysis. *Nat. Methods*. 9:676–682. doi:10.1038/nmeth.2019.
- Schneider, C.A.C.A., W.S.W.S. Rasband, and K.W.K.W. Eliceiri. 2012. NIH Image to ImageJ: 25 years of image analysis. *Nat. Methods*. 9:671–675. doi:10.1038/nmeth.2089.
- Schumacher, M. a. 2012. Bacterial plasmid partition machinery: a minimalist approach to survival. *Curr. Opin. Struct. Biol.* 22:72–9. doi:10.1016/j.sbi.2011.11.001.
- Schumacher, M.A., T.C. Glover, A.J. Brzoska, S.O. Jensen, T.D. Dunham, R.A. Skurray, and N. Firth. 2007. Segrosome structure revealed by a complex of ParR with centromere DNA. *Nature*. 450:1268–1272. doi:10.1038/nature06392.
- Segur, J.B., and H.E. Oderstar. 1951. Viscosity of Glycerol and Its Aqueous Solutions. *Ind. Eng. Chem.* 43:2117–2120. doi:10.1021/ie50501a040.
- Selhuber-Unkel, C., P. Yde, K. Berg-Sørensen, and L.B. Oddershede. 2009. Variety in intracellular diffusion during the cell cycle. *Phys. Biol.* 6. doi:10.1088/1478-3975/6/2/025015.
- Shashkova, S., and M.C. Leake. 2017. Single-molecule fluorescence microscopy review : shedding new light on old problems. *Biosci. Rep.* 37. doi:10.1042/BSR20170031.
- Shekhar, S., L. Zhu, L. Mazutis, A.E. Sgro, T.G. Fai, and M. Podolski. 2014. Quantitative biology: where modern biology meets physical sciences. *Mol. Biol. Cell.* 25:3482–5. doi:10.1091/mbc.E14-08-1286.
- Siebrasse, J.P., T. Kaminski, and U. Kubitscheck. 2012. Nuclear export of single native mRNA molecules observed by light sheet fluorescence microscopy. *Proc. Natl. Acad. Sci. U.S.A.* 109:9426–9431.
- De Simone, A., A. Spahr, C. Busso, and P. Gönczy. 2018. Uncovering the balance of forces driving microtubule aster migration in *C. Elegans* zygotes. *Nat. Commun.* 9. doi:10.1038/s41467-018-03118-x.
- Skarstad, K., H.B. Steen, and E. Boye. 1985. Escherichia coli DNA distributions measured by flow cytometry and compared with theoretical computer simulations. *J. Bacteriol.* 163:661–668.
- Skruzny, M., A. Desfosses, S. Prinz, S.O. Dodonova, A. Gieras, C. Uetrecht, A.J. Jakobi, M. Abella, W.J. Hagen, J. Schulz, R. Meijers, V. Rybin, J.A. Briggs, C. Sachse, and M. Kaksonen. 2015. An organized co-assembly of clathrin adaptors is essential for endocytosis. *Dev. Cell.* 33:150–162.

- Sliusarenko, O., J. Heinritz, T. Emonet, and C. Jacobs-Wagner. 2011. High-throughput, subpixel precision analysis of bacterial morphogenesis and intracellular spatio-temporal dynamics. *Mol. Microbiol.* 80:612–27. doi:10.1111/j.1365-2958.2011.07579.x.
- Smith, M.B., E. Karatekin, A. Gohlke, H. Mizuno, N. Watanabe, and D. Vavylonis. 2011. Interactive, computer-assisted tracking of speckle trajectories in fluorescence microscopy: Application to actin polymerization and membrane fusion. *Biophys. J.* 101:1794–1804. doi:10.1016/j.bpj.2011.09.007.
- Spahn, C., U. Endesfelder, and M. Heilemann. 2014. Super-resolution imaging of Escherichia coli nucleoids reveals highly structured and asymmetric segregation during fast growth. *J. Struct. Biol.* 185:243–249. doi:10.1016/j.jsb.2014.01.007.
- Stewart, R.J., J.P. Thaler, and L.S.B. Goldsteint. 1993. Direction of microtubule movement is an intrinsic property of the motor domains of kinesin heavy chain and Drosophila ncd protein. *Proc. Nat. Acad. Sci. USA.* 90:5209–5213.
- Thévenaz, P., R. U.E., and M. Unser. 1998. Thévenaz P1, Ruttimann UE, Unser M. *IEEE Trans Image Process.* 7:27–41. doi:doi: 10.1109/83.650848.
- Toomre, D., and D.J. Manstein. 2001. Lighting up the cell surface with evanescent wave microscopy. *Trends Cell Biol.* 11:298–303.
- Toyoshima, Y.Y., S.J. Kron, E.M. McNally, K.R. Niebling, C. Toyoshima, and J.A. Spudich. 1987. Myosin subfragment-1 is sufficient to move actin filaments in vitro. *Nature.* 328:536–539.
- Ulman, V., M. Maška, K.E.G. Magnusson, O. Ronneberger, C. Haubold, N. Harder, P. Matula, P. Matula, D. Svoboda, M. Radojevic, I. Smal, K. Rohr, J. Jaldén, and H.M. Blau. 2017. An Objective Comparison of Cell Tracking Algorithms. *Nat. Methods.* 14:1141–1152. doi:10.1038/nmeth.4473.An.
- Ungewickell, E., and D. Branton. 1981. Assembly units of clathrin coats. *Nature.* 289:420–422.
- Usov, I., and R. Mezzenga. 2015. FiberApp: An open-source software for tracking and analyzing polymers, filaments, biomacromolecules, and fibrous objects. *Macromolecules.* 48:1269–1280. doi:10.1021/ma502264c.
- Valfort, A.C., C. Launay, M. Sémon, and M. Delattre. 2018. Evolution of mitotic spindle behavior during the first asymmetric embryonic division of nematodes. *PLoS Biol.* 16. doi:10.1371/journal.pbio.2005099.
- Verde, F., M. Dogterom, E. Stelzer, E. Karsenti, and S. Leibler. 1992. Control of Microtubule Dynamics and Length by Cyclin A- and Cyclin B-dependant Kinases in Xenophobus Egg Extracts. *J. Cell Biol.* 118:1097–1108. doi:10.1083/jcb.118.5.1097.
- Vollmer, W. 2006. The prokaryotic cytoskeleton: a putative target for inhibitors and antibiotics? *Appl. Microbiol. Biotechnol.* 73:37–47. doi:10.1007/s00253-006-0586-0.
- Waterman-storer, C.M., A. Desai, J.C. Bulinski, and E.D. Salmon. 1998. Fluorescent speckle microscopy , a method to visualize the dynamics of protein assemblies in living cells. *Curr. Biol.* 8:1227–1230.

- Waters, J.C. 2009. Accuracy and precision in quantitative fluorescence microscopy. *J. Cell Biol.* 185:1135–48. doi:10.1083/jcb.200903097.
- Welzel, O., D. Boening, A. Stroebel, U. Reulbach, J. Klingauf, J. Kornhuber, and T.W. Groemer. 2009. Determination of axonal transport velocities via image cross- and autocorrelation. *Eur. Biophys. J.* 38:883–9. doi:10.1007/s00249-009-0458-5.
- Welzel, O., J. Knörr, A.M. Stroebel, J. Kornhuber, and T.W. Groemer. 2011. A fast and robust method for automated analysis of axonal transport. *Eur. Biophys. J.* 40:1061–9. doi:10.1007/s00249-011-0722-3.
- Wickstead, B., and K. Gull. 2011. The evolution of the cytoskeleton. *J. Cell Biol.* 194:513–25. doi:10.1083/jcb.201102065.
- Wittmann, T., A. Hyman, A. Desai, M. Planck, M. Cell, and D.- Dresden. 2001. The spindle : a dynamic assembly of microtubules and motors. *Nat. Cell Biol.* 3:28–34.
- Wollman, R., E.N. Cytrynbaum, J.T. Jones, T. Meyer, J.M. Scholey, and A. Mogilner. 2005. Efficient Chromosome Capture Requires a Bias in the ‘ Search-and-Capture ’ Process during Mitotic-Spindle Assembly. *Curr. Biol.* 15:828–832. doi:10.1016/j.cub.2005.03.019.
- Zanella, F., J.B. Lorens, and W. Link. 2010. High content screening: seeing is believing. *Trends Biotechnol.* 28:237–245. doi:10.1016/j.tibtech.2010.02.005.
- Zernike, F. 1953. How I Discovered Phase Contrast. *Science (80-.)*. 121:345–349.